Synthesis of monodisperse FePt Nanoparticles by Pulsed Laser Ablation

Von der Fakultät für Ingenieurwissenschaften der

Universität Duisburg-Essen

zur Erlangung des akademischen Grades eines

Doktor-Ingenieurs
genehmigte Dissertation

von

Marcel Rouenhoff

aus

Kleve

Referent: Prof. Dr. -Ing. Einar Kruis
Korreferent: Prof. Dr. rer. nat. Knut Deppert
Tag der mündlichen Prüfung: 31.10. 2013

dedicated to

my beloved
mother Gerda, sister Tanja
and uncle Wolfgang Rohde

Acknowledgements

This dissertation evolved from a collaboration between the institute for Technology of Nanostructures (NST) of the faculty of engineering sciences and Experimental Physics of the faculty of physics at the University of Duisburg-Essen.
A part of this thesis was financially supported in the framework of the DFG project SFB 445 “Nanoparticles from the gas phase - Formation, structure, properties ” .
The continous motivation and the trust on me by professor F.E. Kruis has very much contributed to the success of my work. The many supporting visits of european and international conferences always again guided my thoughts in ordered tracks. I want to thank professor F.E. Kruis for the continous close-knit collaboration and intensive discussions which continously improved my thesis.
I want to thank professor Roland Schmechel for fruitful discussions, opening new perspectives and supporting me in his function as head of the department of Nanostructures and Technologies.
With his expertize in magnetism Dr. Mehmet Acet was a tremendous help when magnetic measurements had to be done and obtained results had to be evaluated.
Dr. Ralf Theissmann gave me essential support in crystallography and evaluation of samples.
This work would not have been accomplished in this way if I would not be able to take merit from further numerous scientific fellows, colleagues and friends. A detailled list would go beyond the scope. Therefore, I want to thank all scientific and technical collaborators and students of NST and Experimental Physics. I also want to thank the workshops in Duisburg and Essen for manufacturing the used technical devices.

Publications

Portions of the work described in this thesis have also appeared in:

Book chapter

- S. Kala, M. Rouenhoff, R. Theissmann, F.E. Kruis Synthesis and film formation of monodisperse nanoparticles and nanoparticle pairs. NanoScience and Technology, 79, pp. 99–119, 2012.

Conference proceedings

- M. Rouenhoff, A. Nedic, F.E. Kruis, Investigation of the charge distribution in a FePt nanoaerosol formed by pulsed laser ablation. European Aerosol Conference 2007, Salzburg, Austria

- M. Rouenhoff, R. Theissmann, F.E. Kruis, Synthesis of FePt nanoparticles formed by pulsed laser ablation. European Aerosol Conference 2008, Thessaloniki, Greece

- M. Rouenhoff, F.E. Kruis, Nanoparticle film formation by means of an electrostatic precipitator. European Aerosol Conference 2009, Karlsruhe, Germany

Contents

1. Introduction

Nanoparticles have become of increasing interest in the development of technical devices due to their size-specific properties. Physical properties of nanoparticles are influenced by quantum mechanical effects as well as the large ratio between surface and volumetric atoms. In a macroscopic solid-state body with 10^{23} atoms the fraction of surface atoms is only 10^{-7}, whereas a spherical nanoparticle with 8000 atoms (which is equivalent with a particle diameter of 6 nm) having a cubic space centered structure and a lattice constant of a = 0.4 nm has already a fraction of 20 % of atoms at the surface. With decreasing particle diameter and thus increasing ratio of surface and volume atoms the catalytic activity of metallic nanoparticles increases (Rolison [1996], Whetten et al. [1985]) and enhances the sensing properties of semiconducting gas sensors (Ogawa et al. [1981a,b], Kennedy et al. [2003]). Moreover, the increased ratio of surface and volumetric atoms leads to a stronger influence of surface properties on the physical properties of the nanoparticles. The reduced bond force of the surface atoms in comparision to the volumetric atoms leads to a reduced melting temperature of nanoparticles (Buffat and Borel [1976], Xing and Rosner [1997]). Additionally, the lattice constant of nanoparticles is modified under the influence of surface tension (Woltersdorf et al. [1981], Rellinghaus et al. [2000]). The reduction of particle volume with decreasing particle size influences the electrical, optical and magnetic properties of nanoparticles. A transition from ferromagnetic to superparamagnetic behaviour with decreasing particle diameter has been found (Cullity and Graham [2008], Shi et al. [1996]). In the case of very small nanoparticles (d_p =1-3 nm) quantum mechanical effects have a dominating influence on their electrical and optical properties (Alivisatos [1996, 1997], Junno et al. [1999]).

The synthesis of hardmagnetic nanoparticles is of special interest for high-density magnetic data storage. Here, the objective is to use the orientation of magnetization of each particle as equivalent for one bit of data. For data security it is mandatory that magnetization is thermally stable and switchable independently from the environment. A fundamental requirement is that the nanodomains of a single particle show excellent ferromagnetic properties, however, a lower size limit of a magnetic domain occurs due to the occurrence of superparamagnetism below a critical size. This is due to random reorientation of the magnetic moment induced by thermal fluctuations, thereby making long-term magnetic storage impossible. This can be estimated by comparing the thermal energy $k_{\mathrm{B}}T$ with the energy barrier $k_{\mathrm{U}}V_{\mathrm{g}}$ (where k_{U} is the magnetocrystalline anisotropy constant and V_{g} the grain volume). For storage appliations, $k_{\mathrm{U}}V/k_BT$ should be larger than 60 (Alloyeau et al. [2009]). Therefore, when small particles are required to obtain a high storage density over a long time, a high value of k_{U} is required. The most promising route to high k_{U} values is the application of bimetallic alloys, such as CoPt, FePt and CoRh which have k_u values typically one order of magnitude higher than the CoCr-based alloys currently applied in hard disks (Alloyeau et al. [2009]). One of the most promising materials, FePt in the magnetically hard, face centered tetragonal (fct, also called $\mathrm{L1_0}$) crystal phase, has a k_u value of at least $6.6 \cdot 10^6$ J/m³. This value would result in particles with a diameter of 3 nm being 10 years magnetically stable (Weller et al. [2000]). Thus, successful synthesis of those FePt nanoparticles would result in a maximum storage density of around 20 Tbit/inch² (Anders et al. [2002]) and would be much larger than the recent lab standard of around 140 Gbit/inch². Although a large number of studies focused in the last ten years on nanoscale FePt particle films, still substantial problems have to be overcome. Ideally, FePt nanoparticles in the fct phase having identical size and a single crystalline domain, closely spaced but not in direct contact, their easy axes of magnetization all pointing in the same direction, are present in form of a thin film. Most of the problems are related to the fact that the as-synthesized FePt is in the face centered cubic phase (fcc) and needs annealing to temperatures above 600 °C (Barmak [2005]) in order to obtain a phase transformation into the magnetically hard fct phase. FePt nanoparticles are predominantly generated via two main synthesis routes: the wet-chemical colloid route, established by Sun et al.

[2000] or the physical route in which the sputtering technique of thin nanocrystalline films is the most prominent (e.g. Shima et al. [2004]). Sun et al. reported the wet chemical synthesis of FePt nanoparticles with typically a particle size of $d_p = 6$ nm (Sun et al. [2000]). These particles are coated by an organic shell prohibiting the agglomeration after deposition on suited substrates and enabling a self-organisation into the hexagonal narrowest packing. Due to controlled thickness of the organic shell they could vary the distance between particles in the hexagonal formation. An annealing temperature of T =873 K was necessary for the formation of $L1_0$. The onset of agglomeration and coalescence of particles at such high annealing temperatures (Dai et al. [2001], Harrell et al. [2001], Anders et al. [2002]) is problematic. Coalescence causes magnetic coupling between FePt nanoparticles due to exchange interaction (Zeng et al. [2002]) and thus enlargement of effective switching volume. Both techniques are not well suited for high temperature annealing. In the case of colloids this is evident whereas the post-annealing of thin sputtered film leads to grain growth as a result of sintering. Several approaches are being followed to minimize the grain growth as a result of thin film annealing, such as imbedding the FePt grains in carbon film (Sellmyer et al. [2006]), covering the grains with SiO_2 (Xing and Rosner [1997]) or imbedding in molten NaCl (Rong et al. [2010]). High-temperature processing steps of the thin films are however incompatible with manufacturing constraints of the magnetic films and present the main technological barrier for the practical application of high- performance magnetic alloys (Barmak [2005]).

High-temperature annealing without uncontrolled grain growth is ideally carried in the gas phase in combination with size-selection by means of a Differential Mobility Analyzer. This has been shown for PbS (Kruis et al. [1998], Nanda et al. [2002]), SnO_{2-x}(Kennedy et al. [2003]), Au (Magnusson et al. [1999], Messing et al. [2009]), Ag (Scheibel and Porstendörfer [1983]) to mention only a few. Gas-phase synthesis is more complicated by the fact that the material does not evaporate stoichiometrically such as PbS and that the stoichiometry can also not be corrected as in the case on SnO_{2-x}which was produced by in-flight oxidation of SnO.

A physical method conventionally employed to obtain stoichiometrical evaporation is

laser ablation, in which a short laser pulse in the ns-range removes the material from a solid target having the desired composition. A focused laser spot irradiates a target which is continously moved in order to obtain a larger irradiated area and to avoid hole burning. Laser ablation techniques were employed by (Kawakami et al. [1999], Makino et al. [1999], Ozawa et al. [2001], Seto et al. [2001b, 2003, 2005], Suzuki et al. [2001], Orii et al. [2003, 2004], Hirasawa et al. [2006]). Highly purified gas is introduced at various controlled flow rates, often in a low pressure regime, and is used as carrier gas leading the aerosol towards the deposition, e.g. on TEM grids or wafer substrates for ex-situ analysis. Targets consisting of semiconducting material (e.g. Si, Seto et al. [2003]), pure metals or more complex compounds ($SrBi_2TaO_9$, Seol et al. [2002a]) can be converted into nanoscaled functional material. Thus laser ablation is a very powerful tool in materials processing especially for more complex materials mainly based on its property to preserve stoichiometry.

In the frame of this work FePt nanoparticles are synthesized in the gas phase and are sintered on flight at temperatures up to T_s =1573 K in order to achieve $L1_0$ structure. Thus postannealing on substrates can be avoided. The FePt nanoparticles are synthesized by 10 ns pulsed laser ablation at atmospheric pressure and lead through the process route with highly purified nitrogen (99.99995% purity) as carrier gas. Downstream the laser ablation chamber a differential mobility analyzer was operated with sheath gas as to enable a electrical mobility based size selection of nanoparticles. Instead of using low-pressure conditions, atmospheric pressure lowers the propability of diffusional loss inside the cavities upstream the final deposition and improves $L1_0$ formation due to an increase of sintering time in the furnace. In order to achieve reproducibility TEM grids were used as substrate and placed inside a magazine. The magazine is situated in a low-pressure impactor and FePt nanoparticles are deposited while a condensation particle counter was used for controlling the number of particles. Morphological and structural properties of deposited FePt nanoparticles are investigated by STEM, EDX, HRTEM, whereas magnetic measurements were executed with a Superconducting Quantum Interference Device (SQUID). The investigation of influences of process parameter (laser wavelength, laser fluence, aerosol volume flow, sintering tem-

perature) on morphology and structure of particles is the central part of the presented work. The investigations serve for the characterisation of particle formation and sintering behaviour as to check suitability of the processing route out of the gas phase. Main aspects of the work are:

- development of a process to sufficiently synthesize monodisperse, monocrystalline, non oxidized and mainly $L1_0$ ordered FePt nanoparticles,
- the influence of process parameters on the mean particle diameter and the geometric standard deviation of the particle size distribution,
- the dependancy of crystal structure of nanoparticles on process parameters and
- the analysis of sintering characteristics in conjunction with $L1_0$ phase transformation in high-temperature annealing.

Additionally, the magnetic properties of the synthesized FePt nanoparticles are a topic of the presented work.

Initially, theoretical fundamentals of the particle synthesis, the structure of particles and their magnetic properties are presented. It will be followed by the explanation of the experimental set-up, the sample preparation and the applied analytical methods. As next, experimental results are presented and discussed. The influence of process parameters on particle morphology is discussed, as well as the structural and magnetic properties in the following.

2. Theoretical foundations

2.1. Synthesis of nanoparticles in the gas phase

The most dominant method of nanoparticle synthesis in the gas phase is the inert gas condensation. It was introduced by Burger and van Cittert [1930]. One of the first quantitative models for describing this method was published by Granqvist and Buhrman [1976]. In the inert gas condensation a material evaporates or sublimates in a background gas by means of conventional heating, sputtering or laser ablation. The diffusion of the metallic vapour from the hot source to cooler regions causes a supersaturation of the vapour. Nucleation begins if the vapour is supersaturized and it leads to the formation of a large amount of smaller particles. Those particles grow due to Brownian coagulation and coalescence. For analytical purposes, particles are deposited thermophoretically on a cooled substrate as thermophoresis is independent of the size of the particles and guarantees a representative sample of polydisperse particles. Alternatively one can use the methods of low-pressure impaction or electrostatic precipitation if particles are electrically charged. In the following chapter, a detailed description of particle formation by inert gas condensation is presented. The main focus is directed to the model of Flagan and Lunden [1995], which describes the particle growth by coagulation and coalescence.

2.1.1. Nucleation of nanoparticles in supersaturated vapour

The nucleation of nanoparticles in a particle-free supersaturated metallic vapour is homogenous. In the classical nucleation theory the thermodynamic stability of a droplet

is given as a result of the free energy in comparision with the energy of the vapour. One can apply this model for droplets as well for the nucleation of clusters in the supersaturated vapour (Edelstein and Cammarata [1997]). Free energy E of a cluster with n molecules is given by the free energy of n molecules of the macroscopic solid and an additonal term for the surface tension. It can be expressed in dependance of temperature T and supersaturation S by:

$$E(n, S, T) = 4\pi\gamma \left(\frac{3\Omega}{4\pi}\right)^{2/3} n^{2/3} - nk_{\mathrm{B}}T\ln(S) \tag{2.1.1}$$

with k_{B} the Boltzmann constant ($1.38 \cdot 10^{-23}$ J/K), Ω the atomic volume and γ the surface tension. The maximum of free energy in dependance of the particle size (directly connected to n) defines the critical nucleus size d^*. Particles being smaller than the critical size of nucleus will decay, whereas bigger ones are thermodynamically stable as their growth leads to a reduction in free energy. The critical nucleus size can be found by

$$d^* = \frac{4\gamma\Omega}{k_{\mathrm{B}}T\ln(S)} \tag{2.1.2}$$

The relation between nuclei formed per unit of volume and time, the nucleation rate J is given by

$$J \propto \frac{\Omega\sqrt{\gamma}}{k_{\mathrm{B}}T} \exp\left[-\frac{16\pi\gamma^3\Omega^2}{3\left(k_{\mathrm{B}}T\right)^3 \ln^2 S}\right] \tag{2.1.3}$$

An increase of supersaturation causes on one side a reduction of the critical nucleus size d^*(see eq. 2.1.2) but on the other side as well an increased nucleation rate J (see eq.2.1.3). For the determination of critical nucleus size and nucleation rate the surface tension is decisive next to the supersaturation. A decrease of surface tension leads to a reduction of the critical nucleus size. Quantative prediction for the critical nucleus size and the nucleation rate is often not possible as the data for supersaturation and surface tension are not well known. Additionally the fundamental question occurs how far macroscopic properties (e.g. surface tension) can be transferred to nanoparticles.

Conventionally, very large supersaturation is reached in inert gas condensation due to large temperature gradients. It will cause an explosion-like nucleation of primary particles (Flagan and Lunden [1995]). The generated particles serve as condensation nuclei for the remaining metallic vapour. Mean particle size increases by nucleation of subsequent metallic vapour if particles in the size range a_0 till $a_0 + \Delta a$ are generated. The width of size distribution Δa remains and results in an effective descent of relative width of particle size $\Delta a/a_0$. This phenomenon can be used for the synthesis of nanoparticles with narrow number size distributions (Okuyama et al. [1986]). In other cases one has to find a method to size-fractionate particles if special properties in dependence of particle size are to be evaluated.

2.1.2. Particle growth: Coagulation, coalescence and agglomeration

After nucleation particles will further grow by coagulation and coalescence. Coagulation is another synonym for collision of two particles which are then conjugated by van der Waals interaction. Coalescence is causing a conjunction between two coagulated particles often leading to compaction and spherical particles. One specifies the formation of nonspherical particles due to high particle densities in the gas phase as agglomeration.

Already in 1976 particle growth by coalescence was approximated by Granqvist and Buhrman [1976] via statistical analysis. Coalescence between one particle with volume u and a second particle, leads to a new particle with volume $v > u$. An essential assumption of the model is that the change of volume $(v - u)$ of the original particle is a random fragment of the volume v after coalescence. The assumption seems to be reasonable as it represents the reverse process of fractionation of a volume in two partial volumes. One obtains a gaussian size distribution which is often observed throughout experiments as well. The experimentally observed dependancy of the mean particle diameter from inert gas pressure could be explained on the basis of this model by Granqvist and Buhrman [1976]. An enlargement of the inert gas pressure causes a reduction of free mean path of gas molecules increasing the probability of coagulation of two particles and thus resulting in an increase of the mean particle diameter.

Flagan and Lunden [1995] published an enhanced model for particle growth by means of inert gas condensation in 1995. The most important growing mechanism is the Brownian coagulation of particles. A schematic of this model is shown in figure 2.1.1. Primary particles grow after coagulation and coalescence. In case of coagulation the collision time τ_{col}, which depends on the dominating process parameters, is needed. The coalescence time τ_{coa} is used for the coalescence which describes the compaction of coagulated particles. In the initial stage of growth at relative high temperature and small particle diameter coalescence time is smaller than the collision time, $\tau_{coa} < \tau_{col}$. Thus two particles can sinter together into a spherical particle before the next collision occurs. Coalescence time increases more than collision time with increasing particle diameter and decreasing temperature. If a critical particle size has been reached coalescence time becomes larger than collision time $\tau_{coa} > \tau_{col}$ causing an incomplete coalescence of coagulated particles while the next coagulation event already happens which leads to agglomeration.

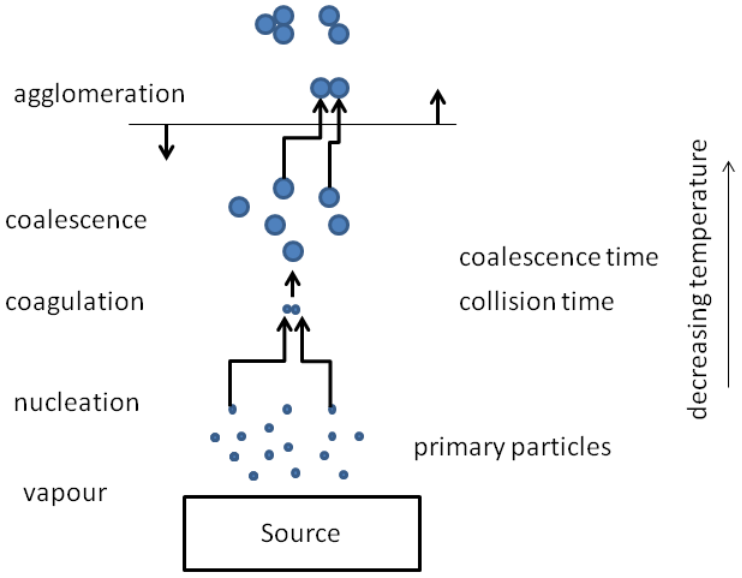

Figure 2.1.1.: Growth model for inert gas condensation.

2.2. FePt in the $L1_0$ phase

In order to achieve the $L1_0$ phase of FePt it is important to know which range of stoichiometry of $Fe_xPt_{1-x}$and sintering temperature is allowed before it is transformed into the disordered cubic space centered structure. The temperature can be as high as 1300 °C if a stoichiometry close to $Fe_{50}Pt_{50}$ is preserved after laser ablation according to the phase diagram (see Fig.2.2.1). As random shapes of FePt occur another issue will be the compaction towards spherical nanoparticles which may require such high temperatures as 1300 °C especially for particle diameter beyond the primary particle size. Short pulsed laser ablation causes an abrupt cooling down of the emitted vapour since electron temperatures up to 20000 K can be reached in the plasma plume while the surround-

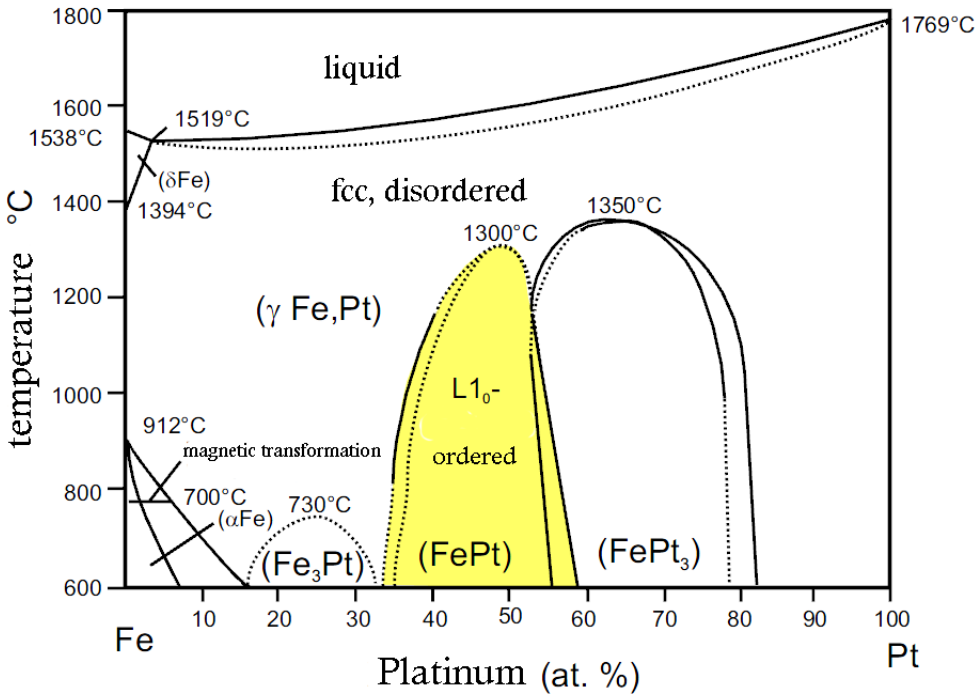

Figure 2.2.1.: Phase diagram of binary FePt alloys (Rellinghaus et al. [1995], Whang et al. [1998])

ing carrier gas is close to room temperature. It is probable that the large temperature gradient kinetically suppresses the formation of $L1_0$ phase and therefore thermal annealing becomes necessary. In most gas-phase processes for FePt a low pressure regime is applied when generating the vapour. However, laser ablation offers the possibility to operate at any kind of pressure since the laser beam is passed through a vacuum-tight and transparent window into the chamber where the target rod is placed. Atmospheric pressure allows a longer residence time of FePt inside the sintering furnace at the same mass flow rate and thus a longer on-flight annealing of the nanoparticles being necessary for the $L1_0$ order. Stappert et al. [2003] and Dmitrieva et al. [2006] tried to achieve a large fraction of ordered FePt nanoparticles. However, annealing time was limited due to low pressure (around 10 mbar) being necessary for the applied sputtering technique.

The schematic of the $L1_0$ crystal structure is presented in Fig.2.2.2. in which alternating layers of Fe and Pt atoms in $\{001\}$direction are characteristic. Different atomic radii of Fe and Pt cause a tetragonal distortion of the cubic structure in stack direction $[001]$.

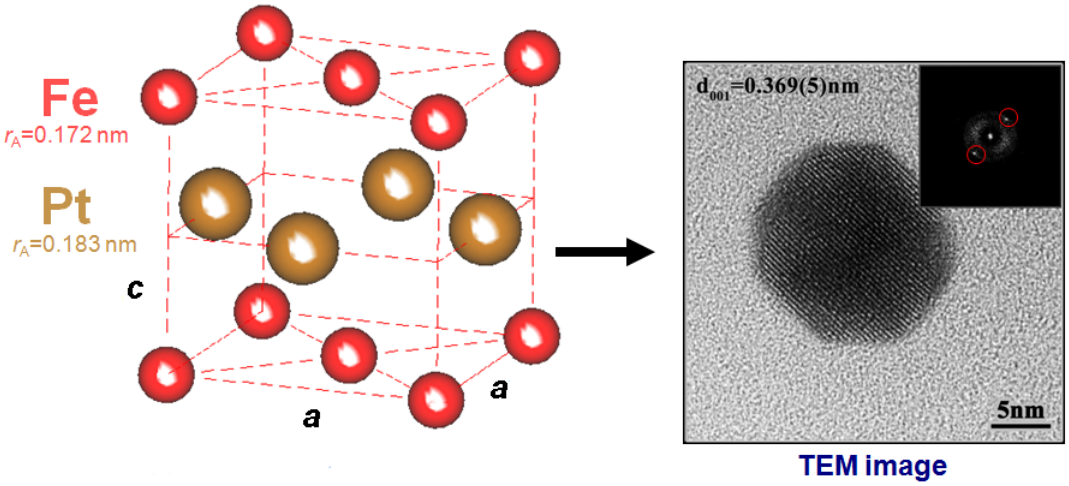

Figure 2.2.2.: Schematic showing the ordered $L1_0$ structure of FePt (left) and a TEM image showing a single monocrystalline FePt nanoparticle with a diameter of 15 nm (right). Characteristic is the alternating sequence of Fe and Pt atomic layers along the $\{001\}$direction. Tetragonal distortion ($a > c$) is effected by the different atomic radii of Fe and Pt atoms.

A c/a ratio of the lattice constants (a along $[100]$or $[010]$ axis; c along $[001]$ axis) is in the range of $0.96 \leq c/a \leq 0.98$ (Thiele et al. [1998], Visokay and Sinclair [1995]). The tetragonal distortion increases the magnetocrystalline anisotropy constant which turns from k_U of $1.1 \cdot 10^5$J/m³ in the disordered phase to $6.6 \cdot 10^6 - 10 \cdot 10^6$ J/m³ in $L1_0$ phase (Weller et al. [2000]). The ordered $L1_0$ structure can be detected with X-ray or electron diffraction by using a high-resolution electron microscope. The large difference between disordered fcc and ordered fct structure is the additional appearance of super lattice reflexes as shown in Fig. 2.2.4. Typically a lattice constant of $a = c = 0.380$ nm can be found for fcc whereas the $L1_0$ structure has lattice constants of $a = 0.385$ nm and $c = 0.371$ nm (Landolt and Börnstein [1992]).

Since the prior mentioned single-particle analysis becomes very elaborative it is more reasonable to study a HRTEM diffraction pattern of an array of FePt nanoparticles deposited on a TEM grid. The diffraction pattern shows circles of diffraction which are rotationally averaged (see Fig.2.2.3) as to keep the statistical error as low as possible. The gray scale can be transferred to different intensities (i.e. white means highest intensity whereas black means zero) such that the diffraction pattern is turned into a radial in-

tensity distribution (see Fig. 2.2.4). This distribution can be analyzed with the Rietveld refinement (Rietveld [2010]) in order to determine the fraction of $L1_0$ FePt nanoparticles. Figure 2.2.4 shows three different intensity curves indicating fully ordered fct, 60% ordered (sample prepared in this work) and the fully disordered fcc state. Red indicators show the common positions of diffraction angles of fcc and fct phase whereas the green indicators show the positions of the superlattice reflexions which only exist in the case of the fct phase. The blue curve indicates the background noise which is subtracted from the intensity profile.

The Rietveld refinement method is discussed in more detail in the following paragraph.

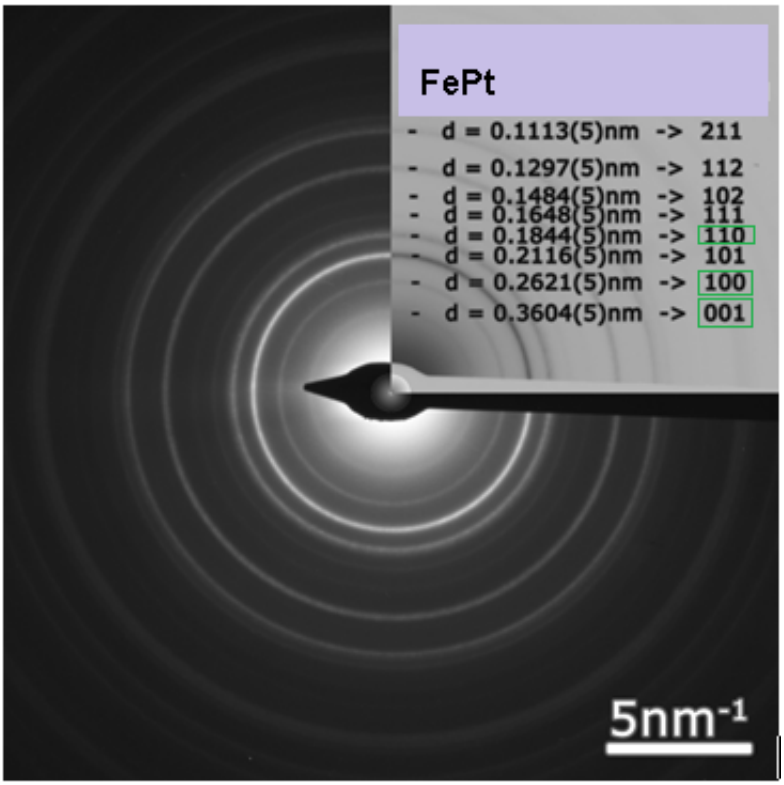

Figure 2.2.3.: Rotationally averaged HRTEM diffraction pattern of a FePt probe: The following process parameters were used: Particle diameter d_p = 15 nm; laser wave length $\lambda = 355$ nm; laser Fluence $F_L = 0.895$ J /cm²; Sintering temperature $T_\mathrm{S} = 1173$ K. Reflexes indicating ordered $L1_0$ phase are marked in green.

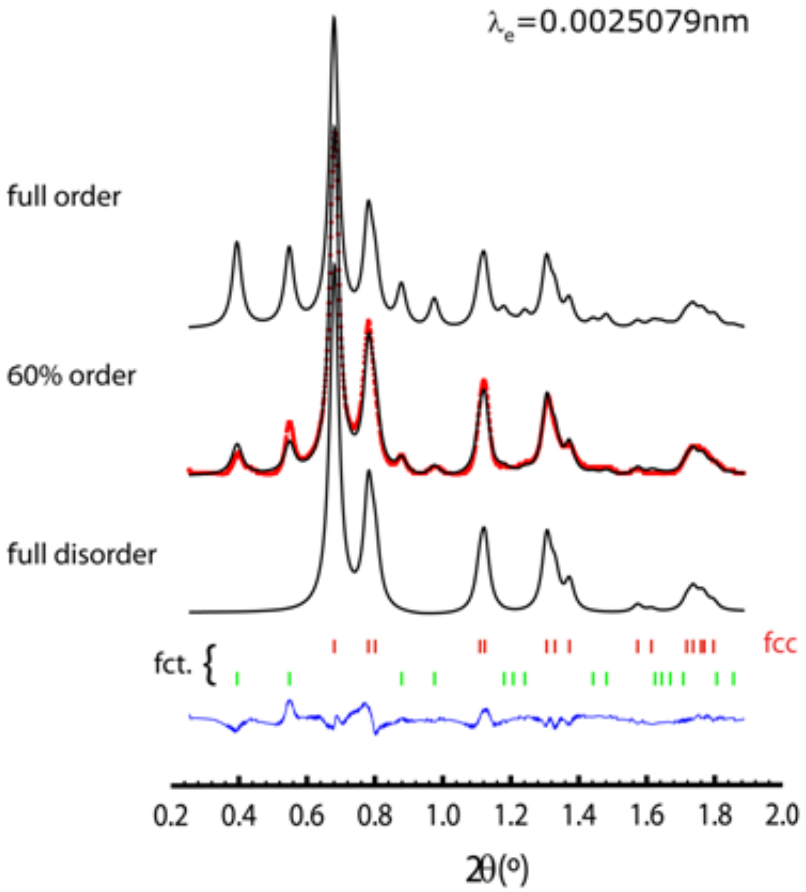

Figure 2.2.4.: Rietveld refinement (red curve) obtained from the radial intensity distribution of the diffraction pattern shown in Fig. 2.2.3 in comparison with the devolution of fully ordered and disordered state.

2.3. The Rietveld refinement

The Rietveld refinement (Rietveld [2010]) being used as standard tool for determining crystal structures in powder diffractometry uses the least-squared-method for the difference S which can be derived as follows:

$$S = \sum_i w_i |y_{\mathrm{io}} - y_{\mathrm{ic}}|^2 \tag{2.3.1}$$

with i the step of measurement, y_{io} the observed intensity at location i, y_{ic} the calculated

intensity at location i and w_{i} the weight factor. The weight factor can be derived from the standard deviation σ_i of y_{io} by

$$w_i = \frac{1}{{\sigma_i}^2} \tag{2.3.2}$$

The calculated intensity y_{ic} is given by

$$y_{\mathrm{ic}} = s \sum\nolimits_k \{ \, m_k L_k |F_k|^2 G(2\theta_i - 2\theta_k)) \, \} + \mathrm{y}_{ib} \tag{2.3.3}$$

where s is a scaling factor, k the Bragg reflex, m_k the spatial frequency, L_k the Lorentz polarisation factor, F_k the structure factor, G the profile function of the reflex k , θ_k the calculated position of the reflex k and y_{ib} the background of the intensity profile at location i. The structure factor can be derived via

$$F_k = \sum_{j=1}^{N} f_j e^{2\pi i (k\, x_j)} \tag{2.3.4}$$

There are several usually used profile functions in order to obtain the best fit with the measured diffraction pattern. The most common used are:

Gauss

$$G = \frac{\sqrt{4 \ln 2}}{\sqrt{\pi} H_k} \cdot \left(e^{-4 \ln 2 X_{ik}^2} \right) \tag{2.3.5}$$

Lorentz

$$G = \frac{\sqrt{4}}{ß \cdot H_k} \cdot \left(\frac{1}{1 + 4 \cdot X_{ik}^2} \right) \tag{2.3.6}$$

Voigt

$$G = \frac{\sqrt{4\ln 2}}{\sqrt{\pi}\cdot H_k}\cdot\left(e^{-4\ln 2 X_{ik}^2}\right) * \frac{\sqrt{4}}{\pi\cdot H_k}\cdot\left(\frac{1}{1+4\cdot X_{ik}^2}\right) \tag{2.3.7}$$

Pseudo- Voigt

$$G = \eta_{\mathrm{PV}}\left(\frac{\sqrt{4}}{\pi\cdot H_k}\cdot\left(\frac{1}{1+4\cdot X_{ik}^2}\right)\right) + (1-\eta_{\mathrm{PV}})\,\frac{\sqrt{4\ln 2}}{\sqrt{\pi}\cdot H_k}\cdot\left(e^{-4\ln 2 X_{ik}^2}\right); 0 \leq \eta_{\mathrm{PV}} \leq 1 \tag{2.3.8}$$

where η_{PV} is the Pseudo-Voigt composition parameter.

Pearson VII

$$G = \left(\frac{\Gamma(\beta)}{\Gamma\left(\beta-\frac{1}{2}\right)}\right)\left(\frac{2^{1/\beta}-1}{\pi}\right)\cdot\frac{2}{H_k}\left(1+4\left(2^{1/\beta}-1\right)X_{ik}^2\right)^{-\beta} \tag{2.3.9}$$

with $X_{ik} = \frac{\Delta\theta_{ik}}{H_k}$, H_k the full-width half -maximum at the Bragg reflex k and β the Pearson composition parameter.

H_k is increased with θ whereupon the Gaussian component $H_k^{Gau} = \sqrt{U\tan^2\theta + V\cdot\tan\theta - W}$ and the Lorentzian component becomes $H_k^{Lorentz} = X\cdot\tan\theta + \frac{Y}{\cos\theta}$. U, V, W, X and Y are free available parameters.

In case of asymmetric diffraction profiles it is possible to split it into two parts and to continue refinement for H_l , H_r or β_l, β_r. The background needs to be filtered out. It can be approximated by deriving a potential array as given by

$$y_{ib} = \sum\nolimits_n b_n\,(2\theta_i)^n \tag{2.3.10}$$

with b_n as free available parameter. One also can add supporting points or the background can be modelled manually. The quality of refinement is checked via the following values:

the weighted R- profile value

$$R_{\mathrm{wP}} = \sqrt{\frac{\sum_i w_i \left(y_{io} - y_{ic}\right)}{\sum_i w_i y_{io}^2}} \tag{2.3.11}$$

the expected R value

$$R_{\mathrm{E}} = \sqrt{\frac{N_{\mathrm{o}} - P_{\mathrm{f}}}{\sum_i w_i y_{io}^2}} \tag{2.3.12}$$

with N_o the number of observations and P_{f} the number of free parameters.

The quality of the fit can be found by

$$Q_F = \frac{\sum_i w_i \left(y_{io} - y_{ic}\right)}{N_o - P_{\mathrm{f}}} = \frac{R_{wp}}{\mathrm{R}_E} \tag{2.3.13}$$

For Rietveld refinement and determination of the $\mathrm{L1}_0$ ordered fraction the program FullProf (Rodríguez-Carvajal and Roisnel [2004]) was used together with the Winplotr interface.

2.4. Magnetic properties of nanoparticles

As explained by Cullity and Graham [2008] one can expect the presence of single-domain ferromagnetic particles if the particle diameter is below the range 50 till 100 nm. Remagnetisation of a single-domain ellipsoidal particle with uniaxial anisotropy occurs at $T = 0$ K through coharent rotation, i.e. by synchronous rotation of all magnetic moments. Remagnetisation can be achieved at $T = 0$ K if one externally applies a switching magnetic coercitivity H_{s}. However reaching $T = 0$ K is not possible. Thus instead one can determine the demagnetization of particles while temperature is continously increased and no external magnetic field is applied. The temperature dependent

relaxation time τ_{rel} for the thermal decay of magnetization can be found by (Osaci et al. [2007])

$$\tau_{\mathrm{rel}}^{-1}(T) = f_0 \exp\left[\frac{-k_U V}{k_B T}\right] \tag{2.4.1}$$

with f_0 as experimental frequency. One can obtain a criterion for thermal stability of magnetisation by setting a certain measurement time of 10 years. Then, the minimum volume of the particle V_{Pcrit} for thermally stable magnetisation is given by

$$V_{\mathrm{Pcrit}} = \frac{25 k_{\mathrm{B}} T}{k_U} \tag{2.4.2}$$

Any particle having a smaller volume than V_{Pcrit} will be thermally unstable within the relaxation time and thus superparamagnetic. Since the orientation of the magnetisation is randomly changing one observes no coercive field H_{C}. As can be seen from eq. 2.4.2 the critical particle volume only depends on the relation between thermal energy $k_{\mathrm{B}}T$ and k_{U}. The superparamagnetic limit of particle diameter d_{p} for $\mathrm{L1}_0$ ordered ($k_{\mathrm{U}} = 6.6 \cdot 10^6 - 10 \cdot 10^6$ J/m³) FePt nanoparticles is in the range from 2.8 till 3.3 mm (Weller et al. [2000]).

At a certain given particle volume one can define the blocking temperature T_B which is the upper limit of temperature for thermally stable magnetisation (ferromagnetic behaviour):

$$T_B = \frac{k_{\mathrm{U}} V}{25 k_{\mathrm{B}}} \tag{2.4.3}$$

For $T < T_{\mathrm{B}}$ and monodisperse non-interacting particles with uniaxial anisotropy the coercivity can be expressed by (Cullity and Graham [2008]):

$$H_{\mathrm{C}} = \frac{2 k_{\mathrm{U}}}{\mu_0 M_{\mathrm{S}}} \left[1 - \left(\frac{T}{T_B}\right)^{1/2}\right] \tag{2.4.4}$$

with $\mu_0 = 12.566 \cdot 10^{-7} \frac{\mathrm{Vs}}{\mathrm{Am}}$ and M_S the saturized magnetisation. The highest coercivity is given for $T = 0$ K :

$$H_\mathrm{C}(T = 0 \text{ K}) = \frac{2k_\mathrm{U}}{\mu_0 M_\mathrm{S}(T = 0\,\mathrm{K})} \tag{2.4.5}$$

3. Gas-phase synthesis

In the last 20 years many different applications of nanoparticles have emerged. Mainly the wet chemical and the gas-phase route are employed for nanoparticle synthesis. One of the most important issues is the production of functional materials offering a high grade of purity. The gas-phase synthesis can be operated without the use of solvents which may pollute the desired product or cause complications in the extraction of the desired material. Gas phase synthesis can be split into the chemical vapour synthesis (CVS) and the physical vapour synthesis (PVS). Whereas in CVS precursor gases are brought together into a reaction chamber in PVS one uses bulk material in form of powders or solids as target for evaporation through sputtering, glowing or exploding wire generator, spark or arc discharge, hot wall evaporation and laser ablation. In the following the PVS methods shall be introduced shortly in order to point out their main characteristics.

3.1. The sputtering techniques

Sputtering can be used for removal of material from the surface of solids and for physical vapour deposition (PVD). In the latter a substrate is situated close to the sputtered target causing a thin layer of condensed atoms. Crucial is the presence of a chamber pressure which prohibits the collision of target atoms with gas molecules on the way to the substrate. The mean free path of gas has got to be at least the distance between target and substrate.

In the most cases a DC ion source is used. Magnetron sputtering is a variant where additionally a magnet is placed below the target enabling the deposition of electrically conducting material. A special advantage which also can be achieved via laser ablation is the preservation of stoichiometry. Mostly metallic films of high purity can be deposited as they are required for electrical circuits on wafer. Often argon is added into the vacuum chamber.

The most important sputtering techniques are DC-, HF-, ion beam, magnetron and reactive sputtering. More detailed information is available from Wasa and Hayakawa [1992] or Wolf [1995]. In the following one can find a brief summary of the mentioned techniques.

3.1.1. DC- sputtering

A DC voltage of some hundreds Volts is applied between target and substrate. The target is the negative and the substrate the positive electrode. By impact-ionisation of inert gas atoms a low pressure plasma is formed containing negatively and positively charged ions. The ions are accelerated towards substrate or target by the presence of the applied electrical field causing a permanent current of positive ions towards the target. By the impact of ions on the target particles are knocked out by pulse transmission. However only electrically conducting targets are suited for DC sputtering. Electrically isolated material would cause a compensation of the DC electrical field and thus stop the sputtering process. Furthermore the production rate of particles is low as only a few collisions occur, due to the reduced presence of gas atoms. DC-sputtering was most recently applied by Kim et al. [2013].

3.1.2. RF-sputtering

A high frequency AC electrical field is applied in the MHz range. The RF voltage source is switched in series with a capacitor and the plasma. The capacitor cuts off the DC component and provides an electrically neutral plasma. Due to the AC field ions and

electrons are alternately accelerated in both directions. Ions stop to follow the alternating field above around 50 kHz due to their low charge to mass ratio. Electrons are oscillating in the plasma causing an increase collision with gas atoms. The sputtering rate becomes very high offering a further decrease of pressure at equivalent sputtering rate and enables the production of very thin layers with different pattern. By superposing a negative offset voltage at the target positive ions move towards the target and sputter atoms out of the surface as in DC mode. Also isolators and semiconductors can be sputtered. In comparison with DC sputtering the substrate remains cooler and sputtering rate is around 10 times larger at the same pressure due to oscillating electrons. RF-sputtering was most recently applied by Khaskheli et al. [2013].

3.1.3. Magnetron sputtering

Whereas in the case of simple cathode sputtering only an electrical field is applied one can also generate an additional magnetic field behind the cathode. By superposition of electrical and magnetical field carriers of charge do not move any more solely due to the electrical field. They are deflected by a spiral track (cycloid) and circle above the target surface causing a higher ionisation. As the ions are not deflected by the magnetic field one can observe the highest sputter rate below the ionized region. Typical for magnetron sputtering are deeper cavities of erosion. Again the sputtering rate is increased in comparision to HF. Magnetron sputtering was most recently applied by Asanithi et al. [2012].

3.1.4. Reactive sputtering

In addition to an inert gas one ore more reactive gases are added. The gases react with the target, in the vacuum chamber or at the substrate with the sputtered atomic layers and form new materials. As well increased reactivity of sputtered target material as additional ions of the reactive gas can further increase the sputtering rate. A disadvantage is some incorporation of inert gas atoms into the target and thus an increasing contamination. Reactive sputtering was most recently applied by Che et al. [2013].

3.1.5. Ion beam sputtering (IBS)

Ion-beam sputtering (IBS) is a method in which the target is external to the ion source. A source can work without any magnetic field like in a hot filament ionization gauge. In a Kaufman source ions are generated by collisions with electrons that are confined by a magnetic field as in a magnetron. They are then accelerated by the electric field emanating from a grid toward a target. As the ions leave the source they are neutralized by electrons from a second external filament. IBS has an advantage in that the energy and flux of ions can be controlled independently. Since the flux that strikes the target is composed of neutral atoms, either insulating or conducting targets can be sputtered. IBS has found application in the manufacture of thin-film heads for disk drives. A pressure gradient between the ion source and the sample chamber is generated by placing the gas inlet at the source and shooting through a tube into the sample chamber. This saves gas and reduces contamination in UHV applications. The principal drawback of IBS is the large amount of maintenance required to keep the ion source operating. Ion beam sputtering was most recently applied by Ievlev et al. [2013].

3.2. The glowing wire generator (GWG)

The GWG was firstly introduced by Schmidt-Ott et al. [1980] as cost-effective method for highly pure aerosol generation. An electrical current is fed through a metallic wire causing a resistive heating until it starts to glow and emits vapour from the surface. With removal of material the wire becomes thinner and conductor resistance increases which limits the electrical power. In our work, a reactor chamber being originally designed for spark discharge was used (see Fig. 3.2.1) and a Ti wire in form of a coil was fixed between two electrode holders. Initially showing a relatively broad number size distribution of Ti nanoparticles it becomes quickly narrower and mean particle size decreases as can be seen from Fig. 3.2.2. The total number concentration is with respect to the power input not satisfying although a trend towards stabilization can be found. As the wire becomes thinner it also becomes more fragile, possibly followed by

a current break-down and sudden stop of particle emission. It is most likely that the stoichiometry of alloys such as FePt is not conserved in the emitted nanoparticles due to the permanent heating of the wire.

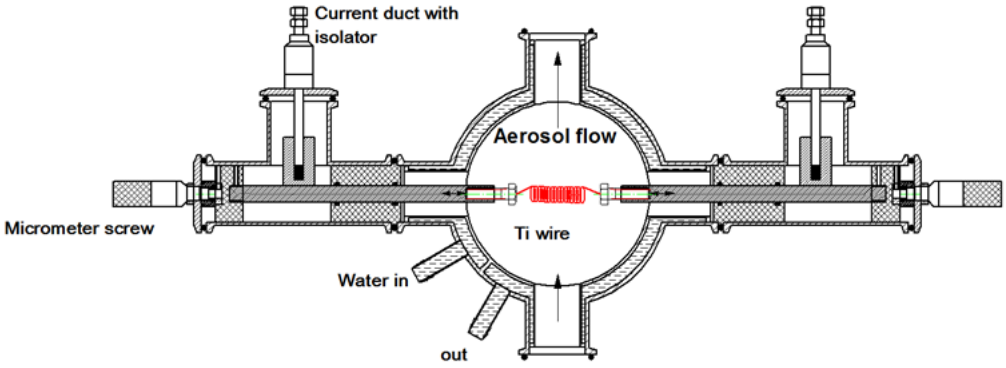

Figure 3.2.1.: The glowing wire generator with a 1 mm Ti wire. Nitrogen was used as carrier gas at atmospheric pressure.

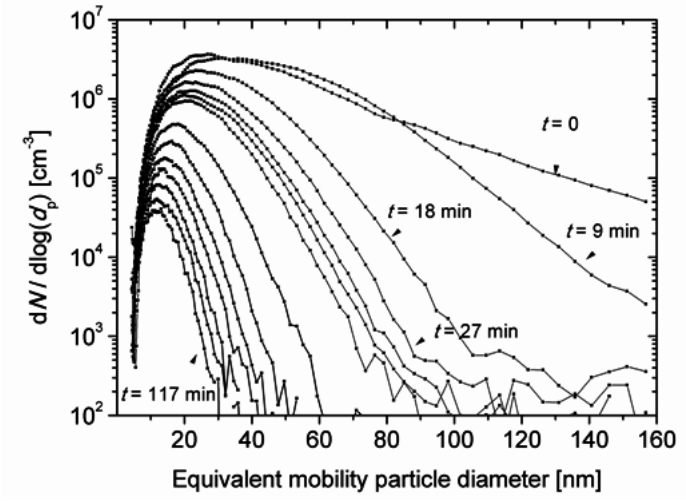

Figure 3.2.2.: Time dependent normalized number size distributions of Ti obtained from the glowing wire generator operating at U = 5 V, I = 10 A and an aerosol flow of Q_A = 100 slpm after evacuating (10^{-4} mbar) and refilling the facility with highly purified nitrogen (99,995%) to atmospheric pressure. Measurements were done with a SMPS model TSI 3080 in the high flow rate modus.

3.3. The exploding wire method

Most recently Das et al. [2012] tested the exploding wire method for generating metallic (copper) nanoparticles. They used a similar set up as presented in Fig. 3.2.1 in which a 0.26 mm thin copper wire was fixed between two electrodes. A high voltage supply is used together with a capacitor being charged until the defined break-down voltage of a sparking gap switched in series with the thin wire. The fast discharge of the capacitor via the sparking gap leads to a µs-current pulse having a peak in the kA range. The wire is instantly vaporized and inert gas condensation forms particles up to 60 nm in equivalent particle diameter. The method is cost-effective and simple. However, after explosion a new wire has to be placed inside the chamber which is time-consuming.

3.4. Spark discharge

Spark discharge is one of the most versatile and cheapest techniques for aerosol generation introduced by Schwyn et al. [1988]. The process of spark discharge is initiated by gas break-down and formation of a conducting channel, and dissociation and ionization of the gas molecules within a very short time. The plasma channel then thermally expands and a shock wave is formed. In the final stage, charge carriers recombine, the plasma cools and the shock wave is attenuated to a sound wave. The rapid discharge consists in a current associated with a high temperature. Electrode material is evaporated in the vicinity of the spark. This is followed by rapid cooling initially governed by adiabatic expansion and radiation and below the evaporation temperature dominated by thermal conduction. Because the vapour cloud is small compared to other evaporation-condensation processes, the cooling period below the boiling point is relatively fast, and a high concentration of very small particles forms (Biskos et al. [2008]).
In order to test its suitability for FePt nanoparticle synthesis a coaxial flow arrangement of a tungsten electrode having a diameter of 1.6 mm and the FePt rod was tested with spark discharge. Nitrogen was used as carrier gas with a flow rate of 10 slm. The electrode gap was set to 0.5 mm. A capacitor charging array having a total capacitance

of 26 nF was charged by means of a high voltage supply (Technix, Creteil, France, model CCR 10-P-7500) up to a break-down voltage of 460 V. Charging current was set to 40 mA . The emitted particles were deposited via low-pressure impaction (see chapter 5) on a TEM grid and analyzed with EDX. The result was a dominating emission of Fe (90%) next to Pt(9.5%) and a small amount of W(0.5%) which could be explained with a rather too long current pulse and thus still a dependancy of different vapour pressure of materials. Spark discharge offers a continuous synthesis of particles as compared to the wire explosion method. It might be possible to maintain stoichiometry if the current pulse duration is limited to the ns range.

3.5. Evaporation in a tube furnace

A tube furnace is used to evaporate material which is usually placed inside a ceramic boat being inside the tube and the center of the heated region. As material evaporates out of the ship it is carried away by a gas stream passing through the tube. Through inert gas condensation vapour nucleates and further grows to nanoparticles. Particle size and morphology can be controlled by adjusting the aerosol flow rate and thus the residence time of nanoparticles in the heated region. The choice of the heated tube limits the maximum temperature needed for evaporation. In order to avoid contamination it is important to choose a tube material that does not emit particulate matter while the desired target material is evaporated. In this work some tube materials were tested with nitrogen as carrier gas at higher temperatures without the presence of any target material. Even Inconel which is a high-temperature steel tends to emit particles at already 750 °C. The best choice is Al_2O_3 as it shows no particle emission at least till 1400 °C as measured with a CPC (TSI, St. Paul, USA, model 3775) and does not deform or destabilize as a quartz tube. However, many desired nanomaterials such as metallic compounds need much higher temperatures for evaporation and moreover the heating rods or wires of the furnace can not withstand such high temperatures for a longer period of time. Since not only the target material is heated up a lot of electrical energy is spoiled for heating the carrier gas.

3.6. Laser ablation in gaseous media

Laser ablation can be applied in liquids (e.g. Liquid Assisted Pulsed Laser Ablation (LA-PLA) as applied by Intartaglia et al. [2012], Al-Mamun et al. [2013] and Nunokawa et al. [2012]) and gases (e.g. Nanoparticle Assisted Pulsed Laser Deposition NAPLD (NAPLD as used by Kawakami et al. [2003], Palani et al. [2012], Nakamura et al. [2012]), Thermally Assisted Pulsed Laser Deposition (TAPLD) as applied by Longtin et al. [2008], Torrisi and Setola [1993]and Li et al. [2005]) depending on the further process of nanoparticle synthesis. In both cases solid materials in shape of a rod are placed inside a chamber and ablated through conversion of photonic energy into thermal energy causing an explosion-like plasma plume. The latest developments of laser techniques allows a pulsed operation of the beam down to the femto second scale. So pulsed lasers are mainly categorized through the duration of a single pulse namely in the femtosecond, picosecond , nanosecond and microsecond range. With increasing pulse duration of the laser thermal effects become more dominant as heat can enter more and more the deeper regions of the ablated material. The number of possible interactions between solid and laser increases with duration as well. Whereas at fs pulse only absorption and excitation occur one will detect additionally photonic ionization and conduction at ps pulses. Laser pulses in the ns scale evoke already a fully developed shock wave which encloses a mixture of vapour and droplets originated from sudden expansion of molten material on the surface. Thermal conductivity becomes highest at µs pulses leading to boiling of the irradiated zone of the solid. In all cases the surrounding liquid or gas becomes ionized due to formation of plasma. Laser ablation is mainly applied for the synthesis of metallic or semiconducting nanoparticles. A big issue for preserving the stoichiometry of ablated alloy or semiconducting compounds is the prevention of thermal equilibrium inside the irradiated region. Thermal equilibrium means that the elements will be evaporated differently due to the different vapour pressures. Thus in the case of FePt more iron than platinum would be evaporated causing a continuous change of stoichiometry of the nanoparticles. This leads to the consequence that a µs pulsed laser is not suited for the evaporation of alloys. The most common used ablation method is pulsed laser deposition (PLD) in which target and deposition sub-

strate are closely placed to each other inside a vacuum-tight chamber. When performed in vacuum, atoms deposit on the substrate where they can form nanoscale “islands” or thin films. In a background gas, the deposition process is mainly guided through diffusion in a low pressure regime. If further annealing is crucial for reaching certain functional nanoparticles PLD is less suited as nanoparticles tend to form bigger clusters through agglomeration. In the following table some of the most recent applications of laser ablation in gaseous media are listed. The main laser parameters are wavelength λ [nm], pulse fluence F_L [J/cm²], repetition rate f_L [Hz] and full width at half maximum (FWHM) pulse duration t_P .

For the determination of the fluence one needs to detect the laser spot or crater diameter d_L. The measurement of the laser spot size is based in the fluence profile $\phi(r)$ of the Gaussian laser pulse(Liu [1982], Bonse et al. [2001]). The pulse fluence has a radial distribution characterized by eq. 3.6.1, where $\phi_0 = 2E_P/\pi w_0^2$ is the fluence maximum, located at the centre of the pulse, E_p is the pulse energy, r is the radius from the pulse centre, and w_0 is the radius where the fluence value drops to $1/e^2$ of ϕ_0.

$$\phi(r) = \phi_0 \exp\left(\frac{-2r^2}{w_0^2}\right) \tag{3.6.1}$$

From this equation a relation between the crater diameter $d_L(= 2r)$ made by a laser pulse with the fluence can be obtained by

$$d_L = w_0\sqrt{2\ln\left(\frac{\phi_0}{\phi_{th}}\right)} \tag{3.6.2}$$

where ϕ_{th} is the ablation threshold fluence, defined as the minimum laser fluence required for starting the material ablation.

In Table 3.1, an overview of recent laser ablation experiments for synthesis of nanoparticles is presented. In most cases argon is used as inert gas in order to prevent oxidation of ablated material. In cases where semiconducting metal oxides such as SnO_2 are needed one has the possibility to add a controlled amount of oxygen. Often one can

find an evacuated laser ablation cell where a target is ablated and nanoparticles are deposited via diffusion on substrates. These are placed closely to the target in order to avoid losses due to the random orientated particle tracks. One can see the preference of choosing a Nd-YAG laser being operated at wavelength of 1064 nm, the 2nd or 3rd harmonic namely 532 or 266 nm. Laser power is simply realized by two arcing lamps, one as main pumping source and the other for amplification. The ablated material is often metallic as e.g. iron, zinc, tin or copper. The pressure regime reaches from less than 10^{-7} till 1013 mbar which means a decrease of the mean free path of gas from several meters till a few microns and different expansion rates of nanoparticles. At lower pressures less collisions will happen and result in less coagulation or coalescence. By this smaller agglomerates can be expected at lower pressures and pressure control offers a good tool for particle sizing. Another possibility is given by choosing a specific laser fluence. Obviously a higher fluence will lead to a more intense plasma plume causing more heat and finally higher evaporation rate. The fluence chosen in this work reaches from relatively low values of 0.15 J/cm² being close to ablation threshold till very large of 4000 J/cm². Often ns pulsed lasers are used for ablation since they offer a compromise between stoichiometry preservation in case of alloys and more economic synthesis next to fs pulsed ones. Particle sizes generated with ablation are in the range from 3 till 160 nm.

Table 3.1.: Overview on recent laser ablation experiments producing nanoparticles.

Laser	Target	gas	p[mbar]	F_L [$\frac{J}{cm^2}$]	λ[nm]	t_P	f_L[Hz]	d_p	Reference
Nd:glass	Carbide	Ar	$1.5 \cdot 10^{-6}$	12	527	250 fs	10	50 ± 20 nm	Bonis et al. [2012]
Nd-YAG	CdTe	Ar	$6.6 \cdot 10^{-6}$	8	355	10 ns	10	15 - 50 nm	Ghosh et al. [2012]
Nd-YAG	Fe and C	Ar	$2 \cdot 10^{-4}$ -20	30	532	8 ns	10	-	Mahmood et al. [2010]
KrF	Al_2O_3, Ge	Ar	$2 \cdot 10^{-7}$	1.2	248	20 ns	10	4 nm -5 µm	Martín-Sánchez et al. [2012]
Nd-YAG	Fe	Ar	0.5	4000	1064	1.5- 5 ms	5- 150	1-10 nm	Wang et al. [2012]
Nd:glass	Fe	Ar	$6 \cdot 10^{-6}$	1.2	527	300 fs	33	14-55 nm	Ausanio et al. [2012]
Nd:YVO_4	Zn	O_2	0.2-1.2	0.17	532	8 ps	50 k	45-58 nm	Sima et al. [2012]
KrF	SnO_2	O_2	$1.3 \cdot 10^{-2}$ - 0.66	1	248	25 ns	10	3-17 nm	Fazio et al. [2011]
Nd:glass	$Al_{70}Cu_{20}Fe_{10}$	Ar	$1 \cdot 10^{-6}$	0.2-2	527	250 fs	10	10-120 nm	Teghil et al. [2009]
Nd:glass	Si, Ni	Ar	$<10^{-7}$	0.15-0.75	780, 1055	100 fs, 1 ps	33	10-160 nm	Amoruso et al. [2006]
XeCl	SnO_2,Pd	O_2	$10^{-4} - 10$	6-10	308	30 ns	-	30-55 nm	Pereira et al. [2006]
Nd:YAG	Cu	He	26, 600, 1013	12	266	5 ns	10	1-10 nm	Koshio et al. [2004]
Nd:YAG	CuO_2	O_2	6.66	10	355	6 ns	10	9,12,15 nm	Suzuki et al. [2012]
Nd:YAG	CdS, ZnS	Ar	$6 \cdot 10^{-7}$	$\leq$1	266, 532	5 ns	10	5-150 nm	Sanz et al. [2011]

4. Size selection techniques in the gas phase

Size selection of FePt nanoparticles obtained from laser ablation allows to investigate the magnetic properties as function over particle diameter. Thus in the following the different methods of particle size selection are discussed. The method should allow subsequent treatment of the selected particles in order to improve the magnetic storage capabilities.

4.1. The Electrostatic Low-Pressure Impactor (ELPI)

The ELPI operating principle can be divided into three major parts; particle charging in a unipolar corona charger, size-classification in a cascade impactor and electrical detection with sensitive electrometers. The particles are first charged to a known charge level in the charger. After charging the particles enter a cascade low-pressure impactor with electrically insulated collection stages. The particles are collected in the different impactor stages according to their aerodynamic diameter, and the electric charge carried by particles into each impactor stage is measured in real time by sensitive electrometers. This measured current signal is directly proportional to particle number concentration and size.

The particle collection in each impactor stage is dependent on the aerodynamic size of the particles. Measured current signals are converted to particle size distribution

using particle size dependent relations describing the properties of the charger and the impactor stages. The result is particle number concentration and size distribution in real-time.

The ELPI was mainly developed as a measuring tool and further treatment of nanoparticles in the carrier gas would become difficult as they are deposited inside the impactor stages. However the impactor stages could be finally used for simultaneously selecting different particle sizes on substrates. By choosing a high number of stages one can obtain a low geometric standard deviation of each number size distribution. However, gas phase synthesis will not generate equal amounts of size selected nanoparticles. If a special layer thickness is needed for analysis or film formation one would need a mechanism to stop the deposition on each substrate after the necessary amount of particles is reached. Such a mechanism could be a sort of moveable cover above a substrate or the substrate itself would have to be shifted out of the particle beam. For determining the number of particles indirectly by an electrometer one would need a conducting substrate. More detailed information can be found from Marjamäki et al. [2000].

4.2. The Centrifugal Particle Mass Analyzer (CPMA)

The CPMA is an aerosol classifier which selects particles according to their mass: charge ratio. It produces a monodisperse aerosol based on a mass metric, compared with a DMA which uses an electrical mobility metric. The CPMA uses opposing electrical and centrifugal force field to classify aerosol particles, a concept first developed by Ehara et al. [1996]. The CPMA consists of two concentric rotating cylinders, with a variable potential difference between them. Particles which have a higher mass to charge ratio than the selected precipitate on the inner cylinder. Particles which have the selected mass to charge ratio follow a trajectory through the classifier.
Crucially and uniquely to the CPMA, the cylinders may be rotated at slightly different speeds. If the cylinders are rotated at the same speed, only particles of the correct mass which also enter along the central trajectory would emerge. The difference in rotation

speed sets up a constant centrifugal field across the classification region. A particle of the correct mass: charge ratio will therefore transit the classifier if it enters at any point along the annular radius. This reduces particle losses in the CPMA (Cambustion [2012]).

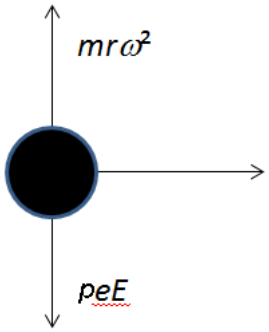

Figure 4.2.1.: The forces having effect on the particle motion inside a CPMA.

The mass to charge ratio is given by

$$\frac{m}{p} = \frac{eU_{CPMA}}{r_{\mathrm{p}}^2 \omega^2 \ln\left(\frac{r_o}{r_i}\right)} \tag{4.2.1}$$

with m as the mass of the particle, p the number of charges on a particle, e is the elementary charge ($e = 1.602 \cdot 10^{-19}$As), U_{CPMA} the potential difference between the concentric cylinders, r_{p} the radial position of the particle, ω the angular frequency of the rotating cylinder, r_o and r_i the outer and inner radius of the classification zone.

The CPMA is a fundamental standard for particle mass provided particles are singly charged. The mass setpoint depends only on the set speed and voltage, and the physical dimensions of the classifier. Unlike a DMA, the setpoint does not depend upon the gas properties (such as viscosity and mean free path) or ambient conditions (temperature and pressure), and furthermore it is not affected by particle morphology (Ehara et al. [1996]).

As selected particles are not deposited inside the CPMA further treatment such as in-flight sintering is still possible. Thus the CPMA could be an alternative method next

to the DMA. However, it is necessary that the rotational axis is better tightened as to avoid oxidation of the nanoparticles which is a critical issue for FePt.

4.3. The Differential Mobility Analyzer (DMA)

Another possibility to classify nanoparticles on flight is given by applying an electrical field causing a defined attraction of charged particles in the gas. This is accomplished using a classifier that is commonly called a Differential Mobility Analyzer (DMA). Inside the DMA a gas flow is passing through two electrodes. A small aerosol flow is introduced near one of those electrodes; a larger sheath flow is added which keeps the particles close to one electrode if no electrical field is applied. As the combined gas flows carry the particles through the channel, a voltage difference between the electrodes drives particles of appropriate polarity across the channel. In differential mobility analyzers, a small flow that exits through a downstream port in the counter electrode extracts particles that have mobilities in a narrow range. DMAs have been built with a number of different geometries. By far the most common geometry is the cylindrical DMA (cDMA) in which the classification takes place in the flow between concentric cylinders (Knutson and Whitby [1975]; Winklmayr et al. [1991]; Chen et al. [1998]; Heim et al. [2004]; Rosell-Llompart et al. [1996]). Classification is also performed using radial flow between parallel disk electrodes in the so-called radial DMA (rDMA) (Zhang et al. [1995]; Fissan et al. [1996]). Although rectangular channels appear in the early literature, edge effects reduce the resolution of such DMAs. However, easiness of miniaturization of such devices led to recent developments with this geometry (Zhang and Wexler [2006]; Kulkarni and Wang [2006]).

The electrical mobility of a charged nanoparticle is defined by

$$Z_{\mathrm{p}} = \frac{peC_{\mathrm{c}}}{3\pi\eta_g d_{\mathrm{m}}} \tag{4.3.1}$$

where C_{c} the slip correction factor is given by

$$C_C = 1 + Kn\left[1.257 + 0.4\exp\left(-\frac{1.1}{Kn}\right)\right], \tag{4.3.2}$$

with Kn the particle Knudsen number determined from

$$Kn = \frac{2\lambda_g}{d_p} = \frac{\sqrt{2}\cdot k_B \cdot T}{\pi \cdot {d_{\mathrm{mol}}}^2 \cdot P \cdot d_{\mathrm{p}}} \tag{4.3.3}$$

with λ_g the mean free path of gas, P the total pressure and d_{mol} the diameter of gas molecules.

η_g is the viscosity of the gas and d_{m} the equivalent mobility diameter of selected particles.

One can define a centroid mobility, corresponding to a particle that enters at the centroid of the incoming aerosol flow, and exits at the centroid of the outgoing classified aerosol flow.

4.3.1. The radial DMA (rDMA)

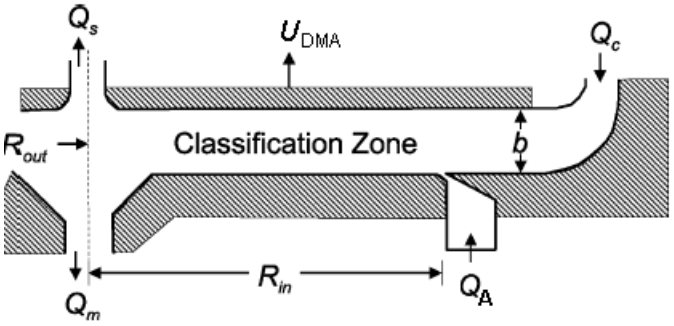

Figure 4.3.1.: Schematic of a Radial DMA.

The centroid mobility of classified nanoparticles by means of a rDMA is

$$Z^*_{\mathrm{rDMA}} = \frac{(Q_{\mathrm{c}} + Q_s)\, b}{2\pi \left(R^2_{\mathrm{in}} - R^2_{\mathrm{out}}\right) U_{\mathrm{DMA}}} \tag{4.3.4}$$

where Q_c is the entering sheath flow, Q_s is the sample flow, b is the distance between the two electrodes, R_{in} and R_{out} denote the radii of the aerosol entrance slot and the classified sample extraction port and U_{DMA} is the voltage difference between the electrodes.

4.3.2. The cylindrical DMA (cDMA)

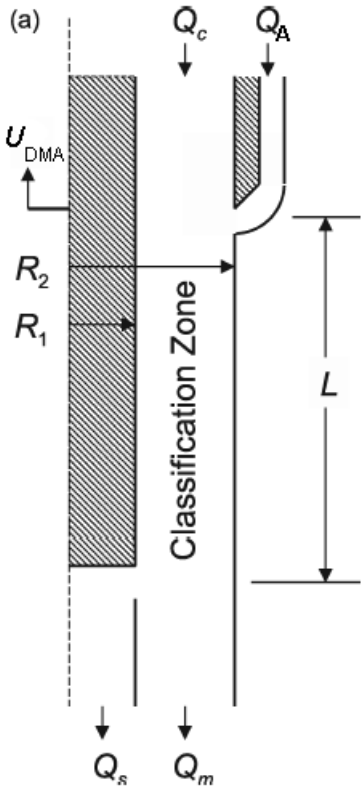

Figure 4.3.2.: Schematic of a Cylindrical DMA(Stolzenburg and McMurry [2008]).

The centroid mobility of classified nanoparticles by means of a cDMA is given by

$$Z^*_{\mathrm{cDMA}} = \frac{Q_c + Q_s}{r\pi L U_{\mathrm{DMA}}} \ln \frac{R_2}{R_1} \tag{4.3.5}$$

where R_1 denotes the radius of the central electrode, R_2 the inner radius of the outer electrode and L the length of the classification zone.

4.3.3. The parallel Plate DMA (pDMA)

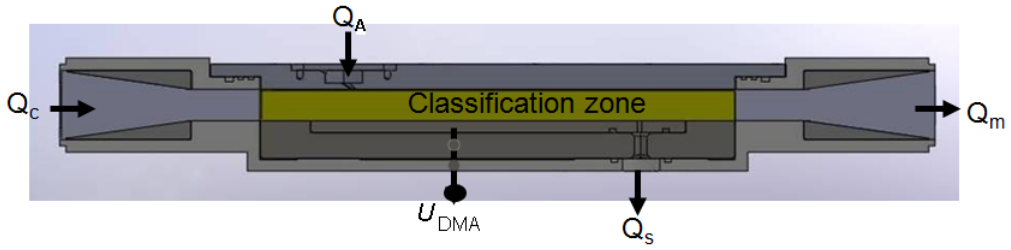

Figure 4.3.3.: Schematic of a Parallel Plate DMA (MegaDMA, RAMEM, Madrid(Spain) for aerosol flow rates up to 200 slm).

The centroid mobility of classified nanoparticles by means of the pDMA is given by

$$Z^*_{\mathrm{pDMA}} = \frac{Q_{\mathrm{c}}}{U_{\mathrm{DMA}}} \cdot \frac{b}{L w_{cz}} \tag{4.3.6}$$

where w_{cz} is the width of the classification zone. Thus the electrical mobility is not depending on the entering aerosol flow.

4.3.4. Transfer function of a DMA

The non-diffusing relative transfer function of a DMA can be derived from Knutson and Whitby [1975]:

$$\begin{aligned} \Omega_{\mathrm{nd}}(\widetilde{Z}_p, \beta_f, \delta) \quad = \quad & \frac{1}{2\beta\,(1-\delta)} \Big[\Big| \widetilde{Z}_{\mathrm{p}} - (1+\beta_f) \Big| + \Big| \widetilde{Z}_{\mathrm{p}} - (1-\beta_f) \Big| - \\ & - \Big| \widetilde{Z}_{\mathrm{p}} - (1+\beta_f\delta) \Big| - \Big| \widetilde{Z}_{\mathrm{p}} - (1-\beta_f\delta) \Big| \Big] \end{aligned} \tag{4.3.7}$$

where the dimensionless mobility is defined as

$$\widetilde{Z}_{\mathrm{p}} = \frac{Z_{\mathrm{p}}}{Z^*_{\mathrm{p}}} \tag{4.3.8}$$

along with dimensionless flow parameters

$$\beta_f = \frac{Q_{\mathrm{s}} + Q_{\mathrm{A}}}{Q_{\mathrm{m}} + Q_{\mathrm{c}}} \tag{4.3.9}$$

with Q_{m} the exiting sheath flow rate and

$$\delta = \frac{Q_{\mathrm{s}} - Q_{\mathrm{A}}}{Q_{\mathrm{s}} + Q_{\mathrm{A}}} \tag{4.3.10}$$

In Fig. 4.3.4 the non-diffusing transfer function of a DMA is shown.

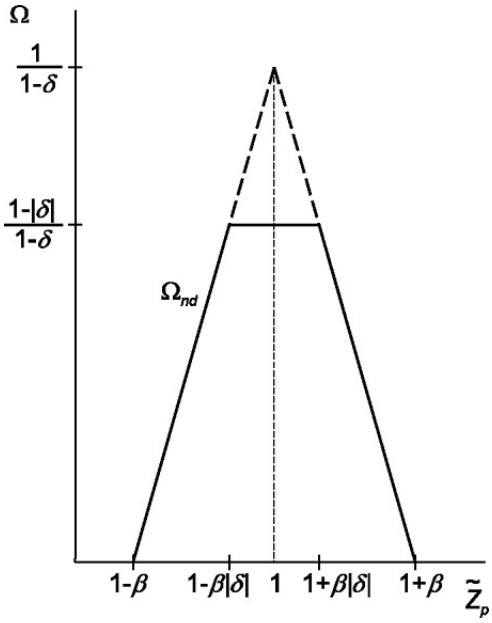

Figure 4.3.4.: Non-diffusing transfer function , Ω_{nd}, showing probability of transiting the DMA for a particle with electrical mobility , $Z_{\mathrm{p}} = \widetilde{Z_{\mathrm{p}}} \cdot Z_{\mathrm{p}}^*$ where Z_{p}^* is the centroid of the transfer function (Stolzenburg and McMurry [2008]).

where the Cunningham slip correction is given by

$$C_C = 1 + Kn\left[1.257 + 0.4\exp\left(-\frac{1.1}{Kn}\right)\right] \tag{4.3.11}$$

with Kn the particle Knudsen number determined from

$$Kn = \frac{2\lambda_g}{d_p} = \frac{\sqrt{2} \cdot k_B \cdot T}{\pi \cdot {d_{\mathrm{mol}}}^2 \cdot P \cdot d_{\mathrm{p}}} \tag{4.3.12}$$

with λ_g the mean free path of gas, P the total pressure and d_{mol} the diameter of gas molecules.

Due to the presence of Brownian motion becoming more dominant for nanoparticles below a size of 10 nm the ideal transfer function of a DMA becomes broader and thus the number size distribution of the monodispersed aerosol as well. In Fig. 4.3.5 diffusion broadening is shown exemplarily for the cDMAs model 3085 and 3081 from TSI if an equivalent mobility diameter d_{p}^{*}= 3 nm is selected (Stolzenburg and McMurry [2008]). As FePt nanoparticles with particle diameters below 10 nm shall be sampled as well one has to consider diffusion broadening if a DMA is used for size selection.

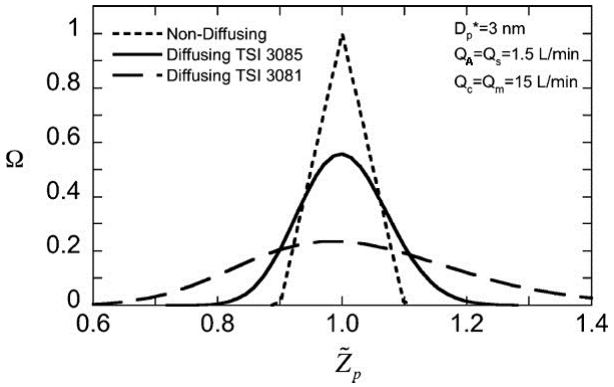

Figure 4.3.5.: Transfer functions, Ω, as a function of dimensionless particle mobility, $\widetilde{Z}_{\mathrm{p}}$, for a flow ratio of β_f=1.5/15 ($\delta = 0$) at DMA centroid diameter d_{p}^{*}= 3 nm. Diffusing transfer function, Ω_d, for TSI 3085 nano DMA and TSI long DMA(Stolzenburg and McMurry [2008]).

The diffusing transfer function, Ω_d , plotted in Fig. 4.3.5 is given in non-dimensional form as (Stolzenburg [1988]).

$$\begin{aligned}\Omega_{\mathrm{d}}(\widetilde{Z}_p,\beta_f,\delta,\sigma) \;=\; & \frac{\sigma}{\sqrt{2}\beta_f\,(1-\delta)}\left[\varepsilon\left(\frac{\widetilde{Z}_{\mathrm{p}}-(1+\beta_f)}{\sqrt{2}\sigma}\right)+\varepsilon\left(\frac{\widetilde{Z}_{\mathrm{p}}-(1-\beta_f)}{\sqrt{2}\sigma}\right)-\right.\\ & \left.-\varepsilon\left(\frac{\widetilde{Z}_{\mathrm{p}}-(1+\beta_f\delta)}{\sqrt{2}\sigma}\right)-\varepsilon\left(\frac{\widetilde{Z}_{\mathrm{p}}-(1-\beta_f\delta)}{\sqrt{2\sigma}}\right)\right]\end{aligned} \tag{4.3.13}$$

where $\varepsilon(x) = x \cdot erf(x) + e^{-x^2}/\sqrt{\pi}$ and erf(x) is the error function, σ is the geometric standard deviation.

4.3.5. Synthesis of monodisperse nanoparticles with help of a DMA

The most recent publications which involve particle size selection of nanoparticles by means of a DMA are listed in table 4.1. The DMA-based size fractionation has become the most preferred method if nanoparticles are synthesized in the gas phase. The device offers a relatively low loss of fractionated nanoparticles. Development of a new DMA for aerosol flow rates well above 30 slm are still in progress as to enable upscaling of the production rate of nanoparticles without increasing agglomeration and thus enlargement of mean particle size. By increasing flow rates one has to deal with higher Reynolds numbers. Thus transition between laminar and turbulent flow will become an issue and probably turbulence could increase the geometric standard deviation of mobility selected nanoparticles. Next to this one has to deal with the classifying aerosol outlet of the DMA as with higher flow rates gas velocity increases and the risk of particle loss due to impaction increases as well. Lowering particle loss is insofar important as the listed synthesis methods in table 4.1 deliver already a low number concentration. Some DMAs have been developed (e.g. Seto et al. [1997]) for the realisation of low pressure conditions, so that vacuum tightness was an important issue. A combination of two DMAs offers the possiblity to determine a charge distribution of a given aerosol (Tandem DMA configuration) or to synthesize heterogeneous nanoparticle pairs being realized due to electrical attraction of monodispersed nanoparticles with opposite polarity (Kala et al. [2012]).

Table 4.1.: A selection of publications which involve size-selection of nanoparticles in the gas phase.

Synthesis method	Material	carrier gas	Q_a [slm]	p [mbar]	Size selection	d_p[nm]	Reference
Hot wall evaporation	Ag	N_2	3	1013	Vienna DMA	50,90,130	Harra et al. [2012]
Spark discharge	Cu	N_2	1.5	1013	n-DMA 3085, TSI, USA	10	Byeon and Roberts [2012]
Hot wall evaporation	Ag, C_{60}	N_2	1.0	270	G3-LPDMA, Wyckoff Co.	3, 20	Tanaka and Maeda [2009]
Spark discharge	Pr	N_2	1.5	1013	n-DMA 3085, TSI, USA	5, 12	Kala et al. [2009]
Laser ablation	Ag	He	0.4-1.0	15 - 30	LP-DMA	13.7	Kawabata et al. [2007]
Laser ablation	ZnTe	Ar	0.2	13	LP-DMA	20	Orii et al. [2007]
Laser ablation	CoPt	He	0.4	10	LP-DMA	15	Seto et al. [2006]
Glow discharge	C, Fe	He	27	1500	DMA	23	Barankin et al. [2006]
Hot wall evaporation, spark discharge	C	N_2	2.0-8.0	1013	TSI 3081 DMA, Vienna DMA	19.5, 31.9, 48.1	Messing et al. [2013]
Hot wall evaporation	Ag	N_2	2.0	1013	Vienna DMA	15, 20, 34, 40, 44, 50	Karlsson et al. [2006]
Hot wall evaporation	$Fe(CO)_5$	N_2	0.01	1013	DMA	18 - 24	Karlsson et al. [2005b]
Hot wall evaporation	Au	N_2	1, 1.5	1013	DMA	2 - 30	Nakaso et al. [2002]

5. The deposition of nanoparticles from the gas phase

Apart from generation of reproducible layers of nanoparticles for obtaining a representative array of samples for investigation it is also crucial to establish a deposition method for a high-density magnetic storage device based on FePt nanoparticles of which each is representing one bit of information. The highest density can be achieved if nanoparticles are as small as possible, will not loose their orientation of magnetization and the space between nanoparticles is as small as possible too. In the following the different available devices for deposition of nanoparticles from the gas phase are discussed in order to find a promising solution both for sampling and one for adequate magnetic film formation.

With each of the following devices one tries to influence the particle motion by using controllable and redirecting external forces. For particle tracking in a model mostly a spherical nanoparticle is assumed which also should be valid for FePt nanoparticles after on-flight sintering. In the fundamental equation for particle motion one considers the force balancing. It is given by (Hinds [1982])

$$m\frac{\mathrm{d}u}{\mathrm{d}t} = -f(u_p - u_\mathrm{g}) + \sum F_i \tag{5.0.1}$$

with m as the particle mass, u_p the particle velocity, u_g the gas velocity, f the friction coefficient and F_i the prior mentioned external forces. The friction coefficient can be derived by

$$f = \frac{3\pi\eta_g d_\mathrm{p}}{C_c} \tag{5.0.2}$$

If a particle is influenced by external forces it does not immediately change its motion. To this end the relaxation time τ_r is defined as

$$\tau_r = \frac{m}{f} = \frac{\rho_p d_\mathrm{p}^2 C_C}{18\eta_g} \tag{5.0.3}$$

As methods for particle film formation the following controllable deposition mechanisms are taken into account:

- impaction due to inertia of nanoparticles (Stern et al. [1962], Fernandez de la Mora et al. [1990])
- thermophoresis (Maynard [1995])
- electrostatic force (Dixkens and Fissan [1999])

5.1. Low-pressure impaction

A large pressure drop over a orifice is used for acceleration of nanoparticles in a carrier gas passing through it. The mean gas velocity inside the orifice can be calculated by

$$u_\mathrm{o} = \frac{Q_A}{A_o} \tag{5.1.1}$$

with Q_A as aerosol flow and A_o the area of the orifice outlet. A substrate is placed into the aerosol stream causing a redirection along the substrate surface. One uses the inertia of nanoparticles for impaction. Inertia can be increased by increasing the velocity of nanoparticles. Nanoparticles with larger mass are leaving faster the gas flow in the moment of redirection. So one will find heavier particles at the center of

redirection (stagnation point). The characteristic parameter in low pressure impaction is the dimensionless Stokes number. It is defined as the ratio of the stopping distance of a particle to a characteristic dimension of the obstacle, or

$$Stk = \frac{\tau_r u_0}{d_c} \tag{5.1.2}$$

where d_c is the characteristic dimension of the obstacle (Hinds [1982]).

Conventional orifices of low-pressure impactors have inner diameter of less than 1 mm which will generate a small deposition spot. For obtaining a film of larger diameter one has to split the orifice into a multiple array of tiny nozzles. Another option would be a moveable substrate underneath the orifice while deposition is in progress. However achieving a large homogenous film is difficult. Porosity of the film is strongly influenced by the impact energy of particles.

5.2. Thermophoretic deposition

Thermophoresis is the weakest force of the discussed ones. It effects the movement of particles in an aerosol flow due to the presence of a temperature gradient. Particles tend to move from the hotter towards the colder region. Thermal energy is defined as (Hinds [1982])

$$E_{th} = \frac{3}{2} k_B T \tag{5.2.1}$$

Thermal energy is transformed into kinetic energy $\frac{1}{2}mv^2$ causing a faster movement of gas molecules in the hotter region. Although the particle movement in the aerosol flow is statistical and non-directional more collisions with gas molecules appear in the hot region causing a netto impulse towards the colder region. Thermophoresis is directly proportional to the temperature gradient ∇T. It can be expressed by (Hinds [1982]))

$$F_{\mathrm{th}} = \frac{-\pi \cdot P \cdot \lambda_g \cdot d_{\mathrm{p}}^2 \nabla T}{4T} \tag{5.2.2}$$

If F_{th} is equated with the Stokes drag force (Hinds [1982])

$$F_{\mathrm{D}} = 3\pi\eta_g d_{\mathrm{p}} v_{\mathrm{p}} \frac{1}{C_{\mathrm{c}}} \tag{5.2.3}$$

where v_{p} is the velocity of the particle relative to the gas flow one obtains the thermophoretic velocity of nanoparticles.

$$v_{\mathrm{th}} = v_{\mathrm{p}} = -\frac{P \cdot \lambda_g \cdot d_{\mathrm{p}} \cdot \nabla T \cdot C_{\mathrm{c}}}{12 \cdot T \cdot \eta_{\mathrm{g}}} \tag{5.2.4}$$

For large Kn the slip correction can be written as

$$C_c \approx 1.257 \cdot Kn \tag{5.2.5}$$

and

$$v_{\mathrm{th}} \propto \frac{P \cdot \lambda_g^2 \cdot \nabla T}{\eta_{\mathrm{g}} \cdot T} \tag{5.2.6}$$

Thus v_{th} is independent from particle size and the number size distribution of nanoparticles thermophoretically deposited on a cooled substrate will be identical with the one of the aerosol. Therefore, for representative sampling this mechanism is well suited. Relatively large and homogenous films can be realized by thermophoretic deposition. However the creation of the film is a very slow process as the typical thermal velocity is only 1-10 cm/s.

5.3. The electrostatic precipitation

Electrically charged nanoparticles can be attracted by applying an electrical field with intensity E_{ESP}. The electrostatic force can be expressed by

$$F_E = peE_{\mathrm{ESP}} \tag{5.3.1}$$

where q is the number of charges on the particle and e is the elementary charge ($e = 1.602 \cdot 10^{-19}$As). Due to the presence of drag force by the carrier gas the particle velocity reaches a constant value. The electrical mobility Z_p is defined as the velocity of a nanoparticle which will be reached in a field of unit strength (1 V/m). Z_p can be calculated from the force balance between drag and electric force:

$$F_{\mathrm{D}} = peE_{\mathrm{ESP}} \tag{5.3.2}$$

For E_{ESP}= 1 V/m one obtains the electrical mobility:

$$Z_p = \frac{peC_c}{3\pi\eta_g d_p} \tag{5.3.3}$$

The conventional ESP being introduced by Dixkens and Fissan [1999] can be seen in Fig. 5.3.1.

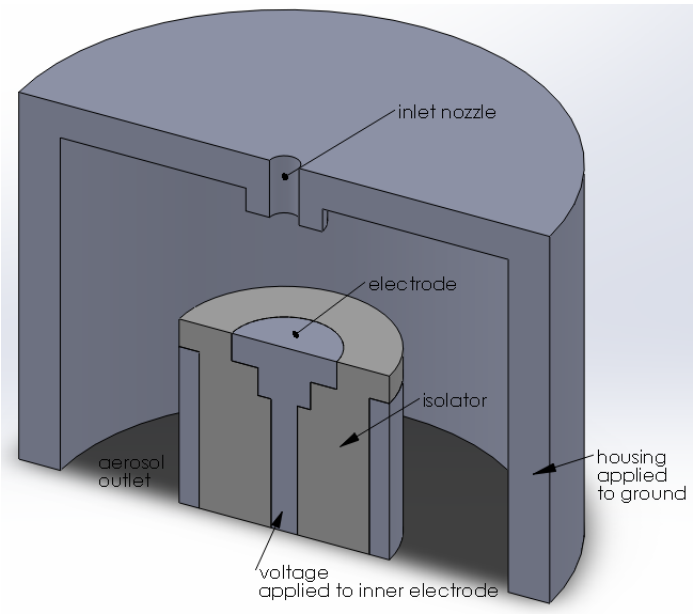

Figure 5.3.1.: Conventional ESP

Initial experiments with this version showed a non uniform deposition spot due to the presence of a recirculating gas flow in the upper region causing the formation of deposition rings on the surface of the deposited substrate. In proceeding versions the influence of recirculation was minimized by separating it with a nozzle plate above the electrode as can be seen from the improved design of the modified ESP (Fig. 5.3.2 (Kala et al. [2012]).

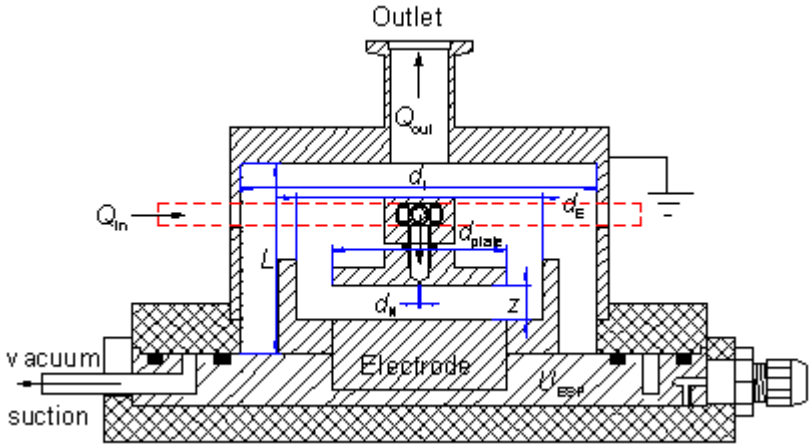

Figure 5.3.2.: Improved version of the electrostatic precipitator for nanoparticle deposition.

Thus in this work, an electrostatic precipitator was developed with the goal to produce a homogeneous deposit of nanoparticles. Its performance was investigated using size-selected nanoparticles in the size range 10-70 nm. The design shown in Fig. 5.3.2 demonstrated the best performance. It allows the distance z between the nozzle and the surface of the central electrode to be varied. Further parameters which can be varied are the nozzle diameter d_{N}, the electrode diameter d_{E}= 70 mm, the electrode voltage U_{ESP} . Differences to previous versions are: 1) instead of a tube-like aerosol inlet, a plate with an orifice is used with a diameter d_{plate} of 50 mm, leading to a more uniform electric field and a more suitable gas velocity profile without a recirculation zone, 2) the aerosol does not flow in the vicinity of the isolator, avoiding deposition of charges on the isolator which causes remnant fields and lack of reproducibility, 3) the gas outlet is placed centrally, as to obtain the most symmetric outflow profile as possible which is necessary to obtain perfectly spherical deposits and 4) attachment of the housing to the base by means of vacuum suction. The performance of the ESP was investigated experimentally with the help of monodisperse nanoparticles in the size range 10-70 nm, generated by means of evaporating PbS powder from a tube furnace at 680°C, followed by a radioactive charger (^{85}Kr), a sintering furnace operating at 400°C and a DMA (Model 3085, TSI, Shoreview, MN, USA). The introduced aerosol flow rate was 1 slm, further z = 10 mm; d_{N} = 1 mm. The electrostatic deposition efficiency is defined as the ratio between the number concentration at the outlet of the ESP with and without applying the high voltage.

Fig. 5.3.3(a) shows that the deposition efficiency increases with the applied voltage, leading to larger electrostatic forces, and decreases with increasing particles size, which is a result of the electric mobility decreasing with size. Images of the deposit were taken with a digital camera, allowing to determine the deposition diameter. Fig. 5.3.3(b) shows that the spot size is a strong function of the particle diameter, and to a lesser extent of the applied voltage. It can be seen that the variability of the spot diameter is limited when the applied voltage is used as control parameter. The spot size in case of the smallest nanoparticles is mainly controlled by the inlet diameter of the nozzle, whereas for the larger particles the spot diameter is much larger than the nozzle diam-

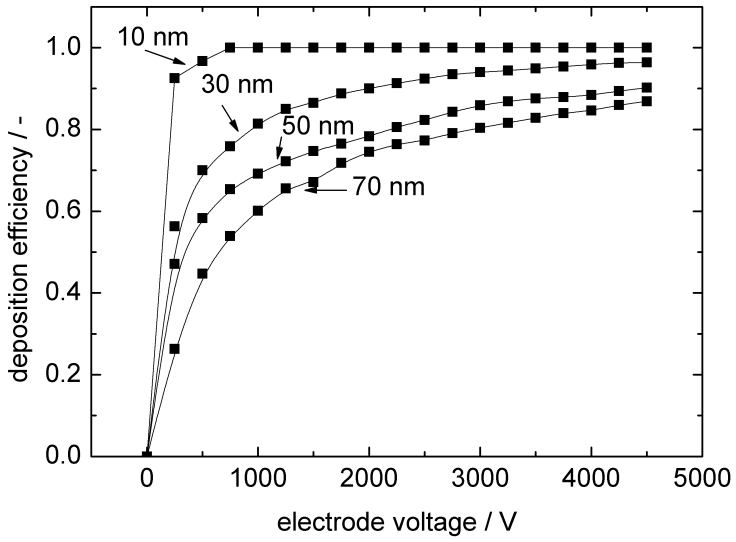

a)

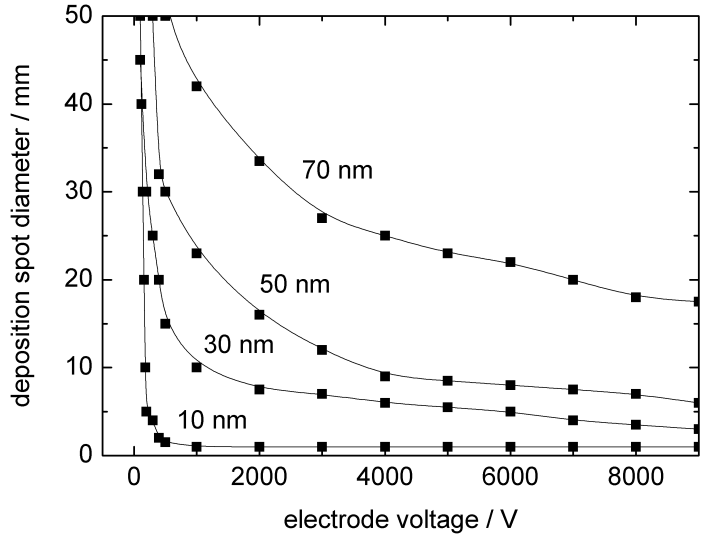

b)

Figure 5.3.3.: (a) The deposition efficiency of ESP for nanoparticles with diameters d_P of 10, 30, 50 and 70 nm. (b) The measured deposition spot diameters using PbS nanoparticles with diameters d_P of 10, 30, 50 and 70 nm as function of applied electrode voltage.

eter. Notice that the difference in deposition behaviour will lead to preferential sampling at different radial positions when depositing polydisperse aerosols.

For the determination of the layer thickness of the deposition spot, a contact profilometer was used (XP 200, Ambios, Santa Cruz, USA), which measures small surface variations due to vertical displacement of a stylus as a function of position. Vertical features ranging in height from 10 nm to 65 µm can be traced by this purely mechanical method. As the stylus can deplace particles and create particle-free tracks, the measurement was started in the center of the deposit using a very small force (30 µg), avoiding this effect. In Fig. 5.3.4 (a), the height profile of the deposition spot is shown for 30 nm diameter nanoparticles. The film thickness at the center was 200 nm at U_{ESP} = 0.1 kV. It can be seen that for the higher voltages a Gaussian deposition profile is found, while for the smaller voltages the deposition profile is constant over a large portion of the film, which is clearly the most desired case. In Fig. 5.3.4(b), the homogeneity as well as the perfect roundness can clearly be seen.

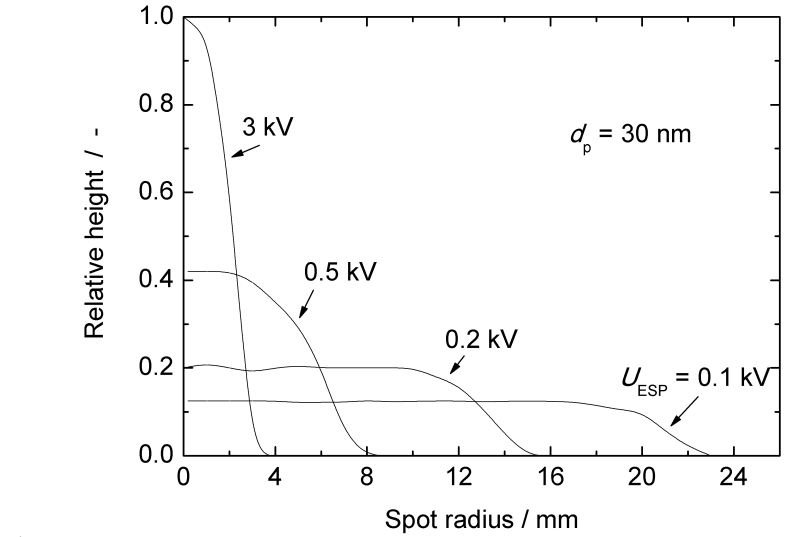

a)

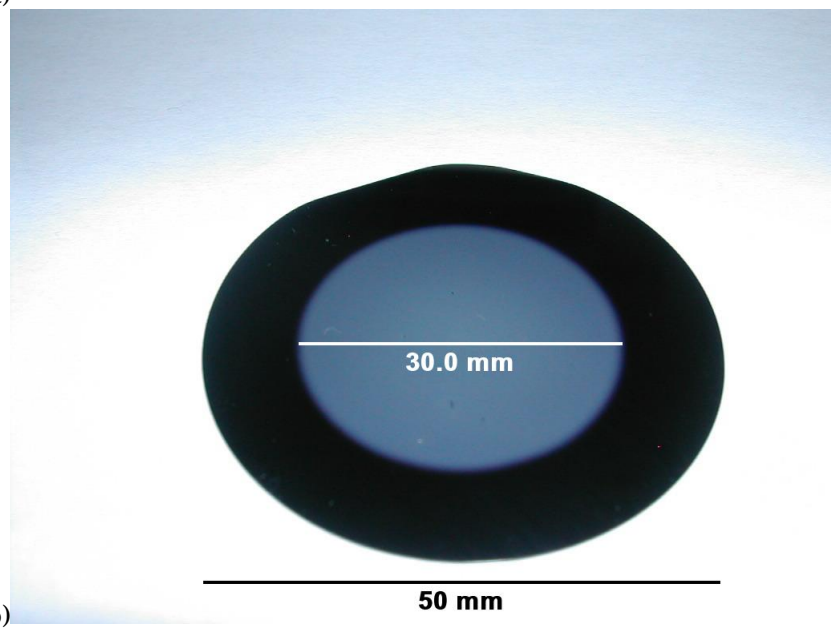

b)

Figure 5.3.4.: (a) The relative height of the deposition spot formed for PbS nanoparticles having a diameter d_P of 30 nm as a function of radial position and electrode voltage U_{ESP}. 2D scans were executed with an Ambios XP 200 contact profilometer being started at the center of the deposition spot and (b) a digital image showing a Si wafer with a diameter of 50 mm being covered by PbS nanoparticles having an equivalent particle diameter d_P of 50 nm by applying an electrode voltage of 0.5 kV.

6. Experimental set up for depositing monodisperse FePt nanoparticles

6.1. Finding the most suitable configuration

Basically, an experimental setup for producing monodisperse FePt nanoparticle in the fct crystal phase is proposed here which contains an aerosol generator(see A), a device for charging the aerosol, a DMA for size fractionation, a high-temperature furnace for on-flight annealing (in order to achieve the $L1_0$ crystal structure and compacted FePt) and a deposition system. Finding the most suitable configuration took several iterative steps and is schematically shown in Fig. 6.1.1. The first configuration (Fig. 6.1.1a) applied a radioactive charger (Am^{241}) for obtaining mainly singly charged nanoparticles after the laser ablation reactor, followed by a commercial DMA (Nano-DMA, TSI, Minneapolis, USA). The DMA sheath gas was supplied by means of a mass flow controller whereas the excess gas was controlled by means of a needle valve before a vacuum suction. A large-diameter tube furnace having a maximum temperature 1200°C and heated length 110 cm (GZF 12/1092, Carbolite, Ubstadt-Weiher, Germany) containing a stainless steel tube having 139 mm diameter and a length of 150 cm was used initially. This arrangement led to strongly oxidized agglomerates, with a very low yield on the TEM grids placed in the electrostatic precipitator. The stainless steel started to emit particles above 800°C, thereby limiting the range of annealing temperature. Furthermore, the large tube dimensions caused a slow cooling down of the aerosol after the annealing zone at the same time, thereby causing a large radial temperature gradient. The sec-

ond configuration (Fig. 6.1.1b) intended to compact the agglomerates before the DMA using another tube furnace (inner diameter 18 mm) containing a ceramic tube (Alsint, Buntenkötter, Neuss, Germany). Applying the annealing step before the size selection turned out to be not possible, as this configuration did not allow to obtain spherical particles. Placing the DMA before the annealing step has the advantage that the annealing is performed with a much lower concentrated aerosol, thereby greatly reducing coagulation during annealing. However, the Cajon tube fittings used for the ceramic tube were not always hermetically tight and had Viton O-rings in contact with the tube, limiting the furnace temperature. Therefore, in the final arrangement (Fig. 6.1.1c) the smaller annealing furnace was placed after the DMA. As the laser ablation process released particles which were already charged to sufficient extent, it appeared that no neutralizer had to be applied. This led to slightly higher concentrations of size-selected aerosol. For the extended deposition times necessary, the use of separate sheath and excess gas controls turned out to be too instable. Therefore, a closed-loop sheath gas arrangement was constructed and applied. Other modifications to the first setup were the use of a vacuum-tight DMA, vacuum-compatible tube connections (KF-style) and the replacement of the electrostatic precipitator (ESP) by a low-pressure impactor (LPI). The LPI had to be used instead of the ESP because the required annealing temperatures turned out to be so high, that the particles lost their charges in the annealing step. A LPI as deposition tool does not require the particles to be charged.

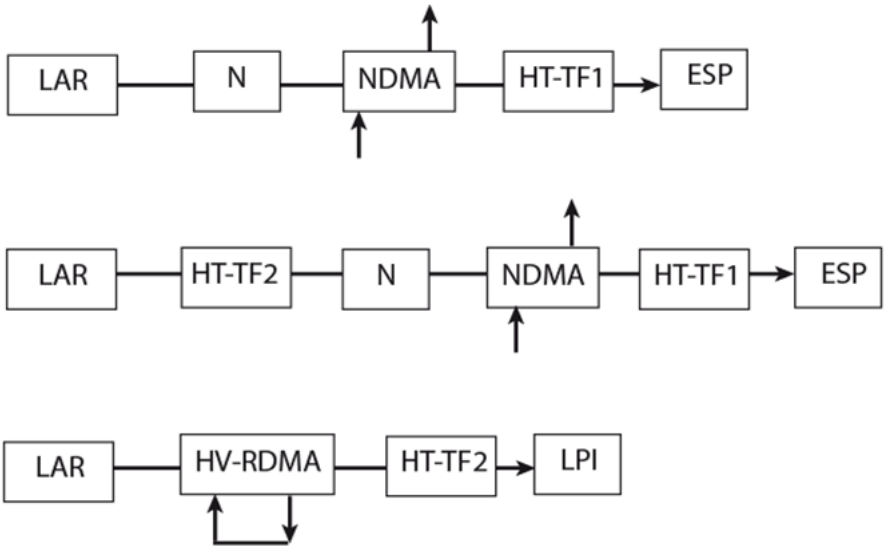

Figure 6.1.1.: The synthesis configurations tested for the synthesis of monodisperse fct-FePt nanoparticles (LAR: laser ablation reactor, N: neutralizer, NDMA: NanoDMA, HT-TF: high-temperature tube furnace, ESP: electrostatic precipitator, HV-RDMA: vacuum-tight radial DMA, LPI: low-pressure impactor)

6.2. The final experimental set up

The final experimental setup, already schematically shown in Fig. 6.1.1c, is shown in more detail in Fig. 6.2.1. The most important requirement was to obtain a vacuum-tight set-up that guaranteed the exclusion of oxygen which caused an oxidation of the iron present in the ablation plume and thereby making the synthesis of $L1_0$ FePt nanoparticles impossible. The ablation chamber, the custom-built radial DMA, the closed loop sheath gas recirculation system as well as the ceramic annealing tube are all fitted with either KF or CF vacuum flanges. The components are linked by means of DIN 16ISO-KF standard vacuum interconnection tubes. The whole setup is evacuated by means of a small turbo-pump backed by a rotary pump to $2 \cdot 10^{-5}$ mbar and refilled by means of a mass flow controller with highly purified nitrogen (99.995 %), which was produced by passing evaporated liquid N_2 through a prepurifier (Oxysorb, Air Liquide, Düsseldorf, Germany) and a getter (MonoTorr, SAES Getters S.p.A., Lainate, Italy). Nitrogen was used as carrier gas, as it is known to enhance $L1_0$ formation due to preliminary

dissociation in FePt as shown by Dmitrieva et al. [2006]. The particle number concentration after different processing steps like size fractionation or in-flight annealing can be measured by means of a condensation particle counter (Model 3775, TSI).

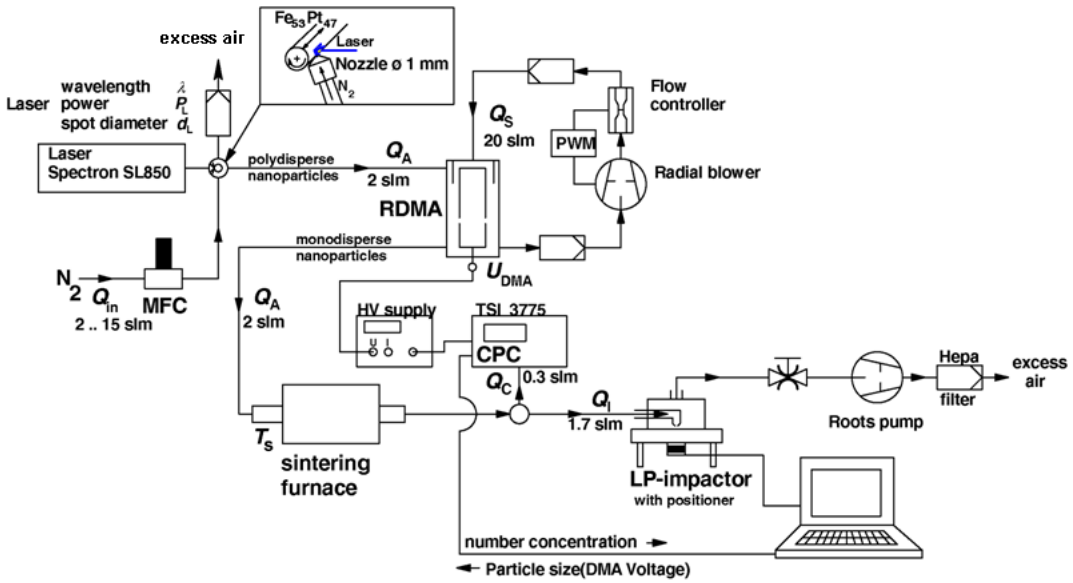

Figure 6.2.1.: The final experimental set up for the synthesis of monodisperse FePt nanoparticles

The ablation chamber consists of a commercial 6-way CF40 vacuum cross (see detailed in Appendix A), connected to the gas inlet, the polydisperse aerosol outlet, a combined linear/rotary vacuum feedthrough, a viewport for a small camera, a fused silica gauge-glass for the laser beam entrance and the laser power meter (Vector H410, Laser 2000, Weßling, Germany). A rod being rotated and shifted in longitudinal direction was selected as target in a similar way as practiced by Seol et al. [2002a], Sakiyama et al. [2004], Suzuki et al. [2009] or Klanwan et al. [2010] in order to achieve homogenous ablation. The target material is a 28 mm long $Fe_{53}Pt_{47}$ rod fixed via the feedthrough to custom-built driver supplying a rotating and translating movement that guarantees that the laser pulses hit the target rod each time at another position. This avoids heating up of the target which would lead to thermal evaporation and thereby loss of stoichiometry. In our case rotational speed and shifting speed are changed periodically in order to avoid beam overexposure of specific regions on the rod causing deeper cavities

in the target. In this way, the target rod is gradually reduced in diameter, the initial diameter being 6 mm. A pulsed Nd:YAG laser (Spectron SL 805-10, Polytec, Waldbronn, Germany) was chosen as it offered the possibility to obtain different laser wavelengths λ of 1064, 512 or 355 nm by applying different optical filtering elements thereby selecting different harmonics of the laser radiation. The maximum output energy is 1300 mJ per shot at 1064 nm (540 mJ@532 nm and 290 mJ@355 nm), the repetition rate 10 Hz and the pulse length 10 ns. The laser power P_{L} can be adjusted by changing the intensity of the main and amplifying arc lamp in the module. The laser output energy is measured with a commercial power meter calibrated at 1064 nm (Vector H410, Scientech, Boulder, CO, USA). It can be combined with a calorimeter (Astral AC2501, Scientech) in order to determine the laser power at other wavelengths in case the laser power is attenuated. The diameter d_{L} of the laser spot hitting the target can be changed in the range from 0.1 up to 1 mm in diameter by moving a collimating lens situated inside a closed container. The laser beam is for safety reasons completely contained. The fluence is defined as the pulse energy per irradiated area. For the determination of the fluence we assumed a radial irradiation spot with a diameter d_{L} at which the power density falls to $1/e^2$ and contains 86 % of the total power (Hull et al. (1985)). The laser spot diameter on the target was experimentally determined by means of thermally sensitive paper. As an example, a laser pulse with d_{L} = 1 mm having an energy of 7.14 mJ leads to a fluence of 0.90 J/cm^2. As the laser power meter was calibrated for 1064 nm, the laser energy at the other wavelengths was determined using the calorimeter, using the known maximum output energy at a given wavelength as a reference. The carrier gas is directed towards the ablated region through a nozzle with a diameter of 1 mm and placed at an angle of 20° at a distance of 2 mm (Fig. 6.2.3a). The carrier gas flow Q_{in} can be varied between 2 and 15 slm, but is in most experiments equal to 2 slm. The DMA is a custom-built, vacuum tight radial DMA (RDMA) having an inlet radius of 44 mm, an outlet radius of 10 mm and a plate distance of 10 mm. With a sheath gas flow Q_{S} of 20 slm it can fractionate particles with mobility diameter sizes up to 40 nm. A flow ratio of $Q_{\mathrm{A}}/Q_{\mathrm{S}}$ maintained at the DMA of 1 to 10 is used to guarantee the supply of monodisperse nanoparticles. A closed-loop recirculation system supplies the sheath gas with a maximum flow rate of 20 slm and makes it possible to operate the system

over weeks without readjustment. It consists of a radial blower with a rotor diameter of 170 mm (RG 160-28/14NTDH, EBM Papst, St.Georgen, Germany), a flow meter (AWM 5104VN, Honeywell, Morristown, USA), and two HEPA filters (see Fig. 6.2.2). A pulse-width modulation (PWM) was used for adjusting the revolutions of the blower. All these components are imbedded in custom-made vacuum-tight stainless-steel housings. A high voltage supply (HCN 14-12500, FUG, Rosenheim, Germany) provides the rDMA with the voltage U_{DMA} and is connected to a PC controlling the deposition. The size-classified nanoparticles are passed through a sintering furnace (STF 15/180, Carbolite, Ubstadt-Weiher, Germany) having a maximum temperature of 1673 K, although for extended operation times a 200 K lower temperature should be used. A alumina ceramic tube having a outer diameter of 25 mm, wall thickness 3.5 mm and heated length of 390 mm is used (Alsint, Buntenkötter, Neuss, Germany) allowing a sintering time of up to 2 s. Creating a vacuum-tight connection to the ceramic tubes was not possible with commercial products such as cajon adaptors. Therefore, stainless-steel adaptors were constructed which created by using an epoxy glue (Plus Endfest 300, UHU, Bühl, Germany) a vacuum-tight connection between the ceramic tubes to the KF16 flanges (Fig. 6.2.3b). A distance of 250 mm between tube furnace outlet and flange was chosen as not to expose the outlet flange to elevated temperatures to avoid excessive heating of the Viton O-rings or glue.

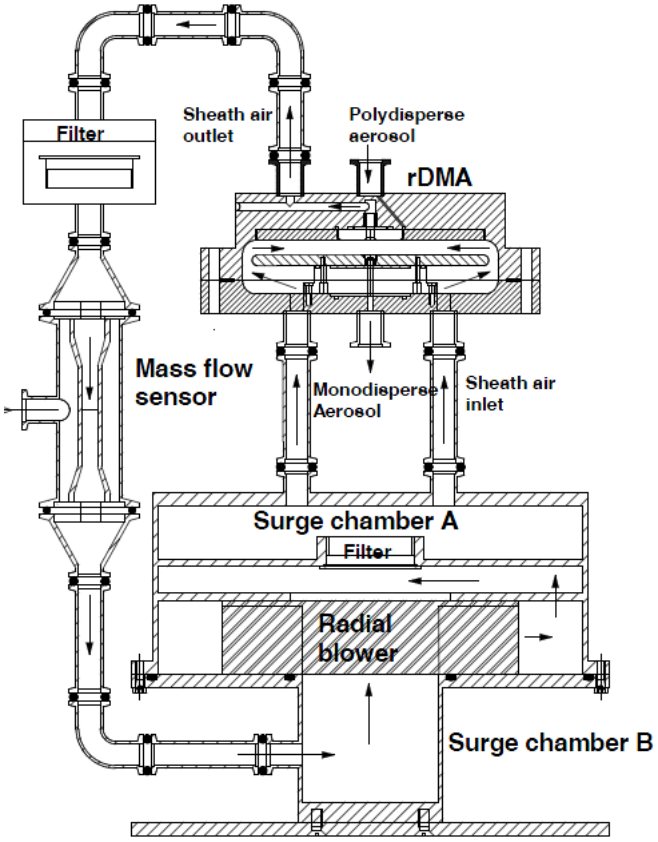

Figure 6.2.2.: The custom built rDMA with sheath gas recirculation.

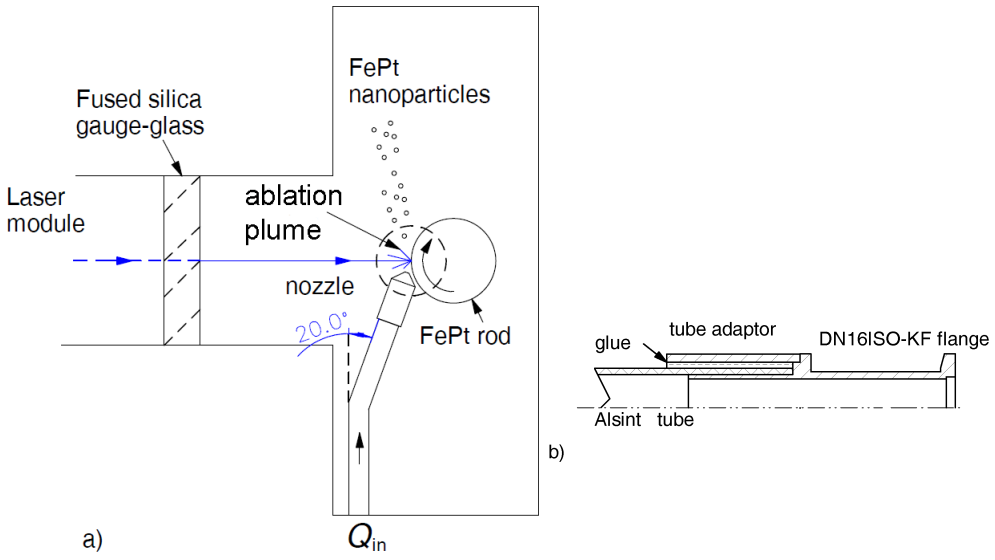

Figure 6.2.3.: a) Schematics of the target arrangement in the laser ablation cell (more detailed in A), b) custom-built vacuum-tight adaptor for ceramic tubes.

6.3. The deposition

For the analysis of the magnetic properties of size-selected nanoparticles on mass basis, the deposition system has to deal with the following requirements:

1) efficient deposition of nanoparticles with sizes below 30 nm, being partly discharged

2) deposit diameter not larger than 2 mm

3) continuous monitoring of the total number of particles deposited, allowing to determine the exact number of monolayers (ML) of particles

4) deposit different samples without exposing the setup to air in order to avoid the evacuation stage for impurity removal

5) deposit enough particle mass.

Requirement 1) is met by applying a low-pressure impactor (LPI, Fig. 6.3.1), having a critical orifice of 0.4 mm diameter, resulting in a sample flow Q_{I} of 1.7 slm. The orifice-to-plate distance is 1.5 mm. The pressure inside the LPI can be varied by using a needle valve in front of the pump. The required pressure was experimentally found to be 20 mbar as to guarantee a highly efficient deposition of the FePt nanoparticles (bulk density 15.4 g/cm^3) with the smallest equivalent mobility diameter d_{m} of 5 nm. The deposition spot diameter d_{s} was found to be 1 ± 0.1 mm for d_{m} = 5, 10 and 15 nm by visual inspection with a confocal scanning laser microscope (TCS SP2, Leica, Solms, Germany), so that requirement 2) is met. Requirement 3) is dealt with by measuring continuously the number concentration N in a 0.3 slm probe flow Q_{C} taken from the 2 slm main flow. This is done by means of a condensation particle counter (model 3775, TSI, Minneapolis, USA) from which the output signal is fed to a PC which integrates the signal so that the total number of particles in the probe flow is obtained. In order to deposit samples for different process conditions, a rotating stage was integrated in the LPI. It is controlled by a stepper-motor (SM 42051, Emis, Dortmund, Germany) placed outside the chamber allowing 400 different positions for a full turn on a spot centered at a radial distance of 10.25 mm, thereby a step distance of 0.16 mm is obtained. In one arrangement (Fig. 6.3.2a), it allows deposition on 20 different TEM grids. In another arrangement, a semicontinuous line is deposited on one of 10 pieces of tape used for magnetic characterisation (Fig. 6.3.2b).

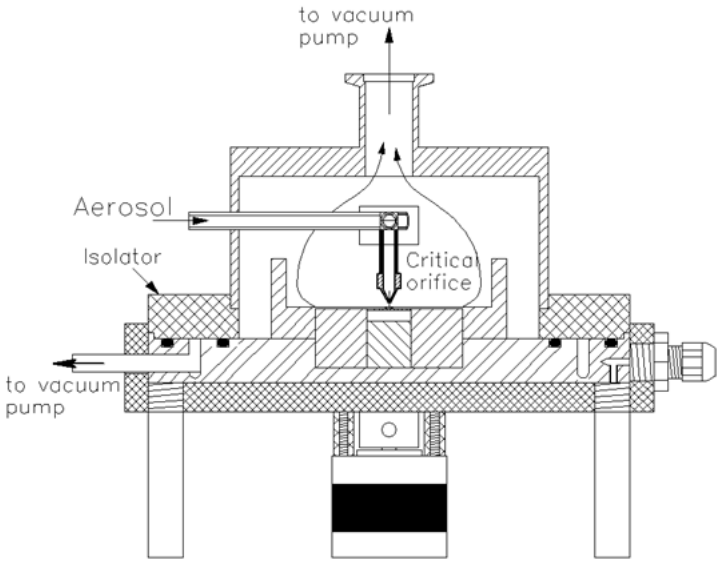

Figure 6.3.1.: The custom built low-pressure impactor with integrated rotating sample holder.

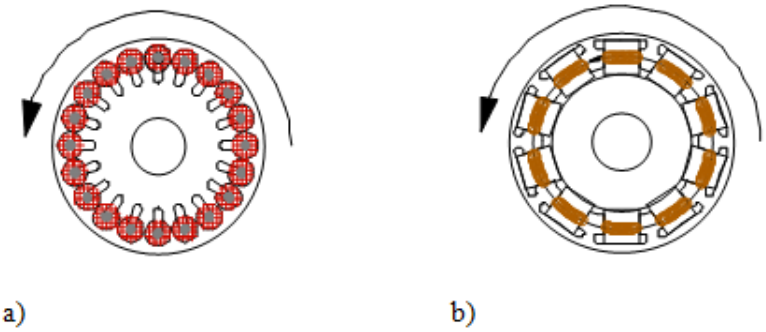

Figure 6.3.2.: Rotating sample holder for deposition onto TEM grids (a) or on a piece of adhesive tape for SQUID measurements (b).

The different characterisation methods require knowledge and control of the effective film thicknesses, conveniently expressed in the effective number of monolayers in the deposit. The following procedure is followed. By continuous monitoring of the CPC signal the number of deposited particles after a given time t is calculated as

$$n_{\mathrm{d}}(t) = Q_I \frac{\eta_{LPI}}{\eta_{CPC}} \int_0^t N dt \tag{6.3.1}$$

with η_{LPI} the deposition efficiency of the LPI (0.71, 0.83, 0.92, 0.98 for sizes of 5, 10, 15 and 20 nm, mainly caused by diffusion losses) and η_{CPC} the counting efficiency of the CPC (0.7 for d_{m} = 5 nm, 0.95 for d_m = 10 nm, and 1 above 15 nm). For obtaining a one ML deposit, the number of particles is

$$n_{1ML} = \frac{v_{1ML}}{V_p/c_v} \tag{6.3.2}$$

in which $v_{1\mathrm{ML}}$ is the volume of the 1 ML thick deposit having a deposition diameter d_s and thickness equal to the particle diameter d_p, V_p is the particle volume and c_v the packing density which is set to 0.74. Although the film will be more porous than 74%, one prefers to define the number of monolayers in terms of the maximum possible packing density. Further, the particle diameter is equal to the mobility diameter in case of singly charged spherical particles. Equation 6.3.2 can be written as:

$$n_{1ML} = \frac{3d_s^2 c_v}{2d_p^2} \tag{6.3.3}$$

The deposition procedure is thus as follows: the desired number of monolayers and the particle size is entered in the deposition software, then the DMA voltage is set and the deposition is carried out until the number of deposited particles reaches the desired number of particles for the given number of monolayers calculated via eq. 6.3.3. The control software then sets the DMA voltage to 0 to stop the deposition, and the sample holder is rotated for deposition on the next sample.

6.4. The probe preparation and characterization

Deposition has to be performed on TEM grids for analysis in a high-resolution transmission electron microscope (HRTEM, Tecnai F20, FEI, Hillsboro, USA) as well on non-magnetic adhesive tape for magnetic characterisation. Analysis of size distribution of

the HRTEM images required a TEM grid coverage of approx. 0.2 ML, more than classically advised to obtain images of noncontacting particles as the magnetic interaction between the particles decreased the probability of contacting particles. Classically, crystal structure is analyzed by means of X-ray diffraction, but this requires at least 10 mg of powder. In case of the size-fractionated particles, this would require unrealistic long deposition times. Therefore electron diffraction was performed inside the HRTEM. The analysis of crystalline structure, which was done by (SAED) in HRTEM with ensuing Rietveld refinement, required at least 1 ML to obtain a signal. This analysis allowed determining the fraction of the fct crystal phase in the deposit. The particle stoichiometry which plays a key role for the magnetic properties is determined by inertial low-pressure deposition on a 4x4 mm piece of B-doped silicon wafer followed by EDX measurements using a Bruker AXS X flash EDX detector 5030 connected to a high-resolution scanning transmission electron microscope (HR-STEM, 7500F, JEOL, Tokyo, Japan). The magnetic measurements were performed in a superconducting quantum interference device (SQUID, Quantum Design MPMS) magnetometer. A special sample preparation had to be developed in order to deal with the small amount of deposited mass in a single ML (in the µg range). Therefore, the particle deposit was done on a piece of one-side adhesive tape (TESA 51446, thickness 0.1 mm), with the particles depositing onto the adhesive side as to minimize the distance of the probe towards the Josephson junction. Prior conventionally used Si wafers (4x4 mm) were positioned inside the straw resulting in a larger distance causing a significant signal loss. After deposition, the TESA segment was then fixed on a plastic drinking straw (Fig. 6.4.1b). In this way, the deposit was well protected and could be conveniently handled and glided inside the SQUID, with the particles coming as close as possible to the Josephson contact.

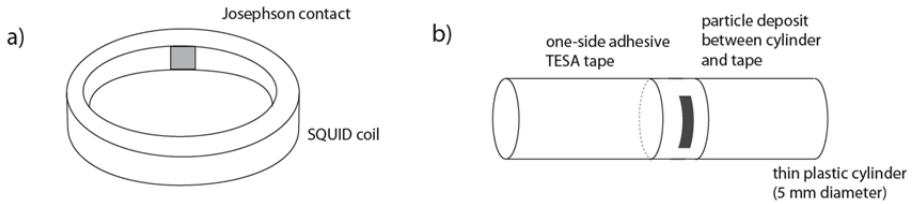

Figure 6.4.1.: a) SQUID coil with Josephson junction used as magnetometer, b) sample suitable for inserting into the SQUID coil.

In order to make full use of the detection area of the Josephson junction, a particle deposit in form of a line segment is ideal. For obtaining a line segment of 5 mm length and 1 mm width the stepper motor was rotated 24 steps, each step depositing 1 ML in deposit having 1 mm in diameter. In this way a deposition having approx. 6.2 ML is obtained. The total deposited particle mass is calculated based on this knowledge, made possible by the precise particle counting as well as the spherical form of the size-selected nanoparticles.

7. The optimization of laser ablation for synthesizing FePt nanoparticles

7.1. The relevance of a vacuum tight DMA

Initial experiments were carried out using commercial DMAs (models 3085, 3081, TSI, St.Paul, USA) which are not designed for vacuum-tightness. Although a slight overpressure in the lines can be established with respect to the atmosphere, there will be still a large difference in partial pressure for the oxygen between the reactor and the environment when using nitrogen as carrier gas. This partial pressure difference is in the opposite direction as the total pressure gradient and will act as driving force for oxygen diffusion into the reactor. Even using ultrapure nitrogen as carrier gas, the particles synthesized under these conditions show FePt cores imbedded in larger FeO_x particles. This is illustrated by Fig. 7.1.1. Clearly, these particles do not meet the requirements. These results led into the development of a tight rDMA and a new sheath recirculation system.

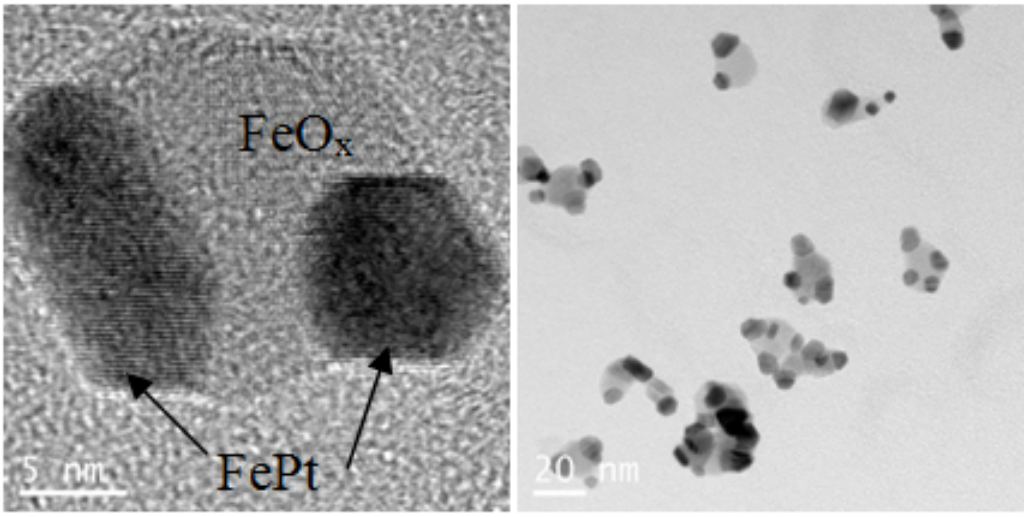

Figure 7.1.1.: The formation of ironoxide when using a commercial, non vacuum-tight DMA (Long DMA 3081, TSI, St.Paul, USA; F_L = 0.895 J/cm²; λ = 355 nm; T = 1473 K; d_L = 1 mm; Q_{in} = 2 slm; d_m = 20 nm). Ironoxide was detected by using a Bruker AXS X flash EDX detector 5030.

7.2. The influence of the laser wavelength

The desirable magnetic properties of FePt can optimally be met by using stoichiometric material, meaning a 50:50 atomic composition. As it is well-known that the laser frequency plays an important role in the conservation of stoichiometry when starting with stoichiometric target material, the laser wavelength was varied from 1064 nm to 532 nm and 355 nm while maintaining a fluence of 0.895 J/cm². Polydisperse FePt samples were obtained by simply switching of the sheath gas recirculation and deposited on TEM grids by means of the LPI, applying at least 5 hours of deposition to obtain sufficient film thickness. The Fe K-line was used for determining the atomic composition, whereas for Pt the L-line was used. EDX results were averaged from 10 different locations on each probe. By using reference samples the error in the determination of the Fe content was found to be ±0.6 at%, for Pt 1.10 at%. The results are shown in Table 7.1. It can be seen that the larger wavelengths (1064 and 532 nm) lead to nonstoichiometric material, whereas the wavelength in the near-UV leads to almost stoichiometric material, with respect to stoichiometry suitable for further processing into magnetic thin nanoparticu-

Table 7.1.: The atomic compositions of FePt nanoparticle layers determined with EDX at different laser wavelengths λ (F_L = 0.895 J/cm²; d_L = 1 mm; Q_{in} = 2 slm; T = 293 K; $Fe_{53}Pt_{47}$ rod).

Wavelength λ [nm]	Fe content [at%]	Pt content [at%]
1064	72.1	27.9
532	59.2	40.8
355	52.6	47.4

late films. Shorter wavelengths such as in the UV range prevent deeper penetration of the laser and heating of the target which causes different evaporation rates of Fe and Pt due to different vapour pressures (Bäuerle [1996], ch. 12).

The influence of laser wavelength on the yield of particles of different mobility equivalent diameters was studied by means of the rDMA in combination with the CPC. As the DMA is an integral part of the process, the yield is expressed in terms of number concentration after the size selection step. Using an SMPS would give the real size distribution, however a neutralization step is then included and the DMA transfer function is removed from the instrument's response. For this particular application, only the charged particles are relevant for the process. In practise, inserting a neutralizer after the laser ablation did not change the number concentration by more than 5 %, so that one can conclude the charge state of the aerosol formed is not far from the usual charge equilibrium state as measured by Wiedensohler [1988]. In Fig. 7.2.1 it can be seen that smaller particles are obtained when reducing the wavelength, the modal particle size shifts from 100 nm (@1064 nm) over 35 nm (@532 nm) to 20 nm (@355 nm). This can be explained by the reduced penetration depth of the laser radiation at smaller wavelengths, leading to a smaller mass removal and per consequence smaller volume concentration of coagulating aerosol per laser pulse. This is known to lead to smaller mean particle sizes. In these experiments, care has been taken to adjust the laser intensity for each wavelength so that identical fluences were used in these experiments. Both the better stoichiometry at 355 nm as well as the much larger particle yield around a mobility diameter of 20 nm led to the conclusion that the wavelength of 355 nm was the most suitable and was consequently applied in the following measurements.

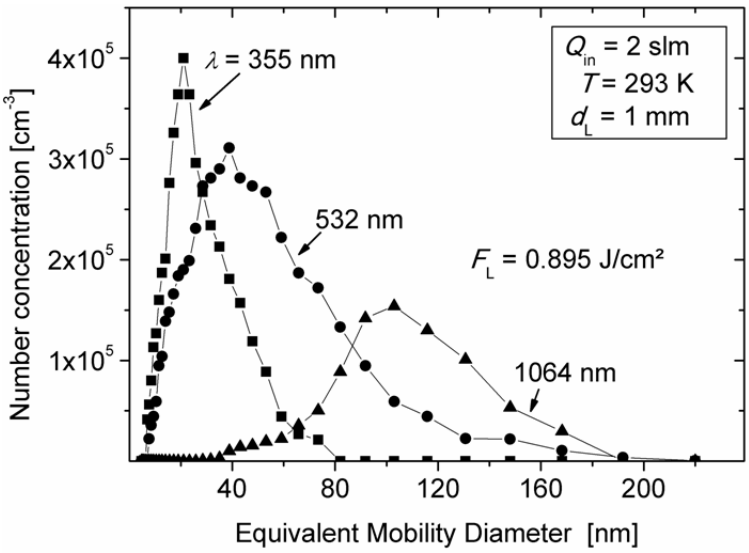

Figure 7.2.1.: The nanoparticle yield as function of the equivalent mobility diameter at different laser wavelengths measured with model TSI 3081.

7.3. The influence of the laser fluence

The laser ablation threshold below which no particles were detected with the CPC was experimentally determined to be 0.5 J/cm². The existence of an ablation threshold is well-known, the ablation rate expressed as µm removed per pulse is most for materials virtually zero below a certain threshold (Bäuerle [1996]). Increasing the fluence to 0.895 J/cm² resulted in a suitable particle number concentration, up to $4 \cdot 10^5$ cm^{-3}, in the diameter range 5-20 nm (Fig. 7.3.1). It can also be seen that increasing the laser fluence from 0.895 J/cm² up to 4.48 J/cm² did not greatly influence the yield of the sub-20 nm particles and increased the yield of particles larger than 25 nm. Similarly, Ozawa et al. [2001] found that a laser fluence of 3.8 J/cm² generated a higher number concentration and larger size of nanoparticles than a fluence of 1.9 J/cm². As for magnetic FePt nanoparticles the size range of interest is between 5 and 20 nm, using the larger fluences would have caused a deterioration in the monodispersity when selecting, e.g., 20 nm nanoparticle diameter. This is due to the increasing fraction of multiply charged particles coming from the larger diameters. Increasing the fluence drastically to 89.5 J/cm² by choosing a smaller laser spot diameter of 0.1 mm leads to a decrease of the

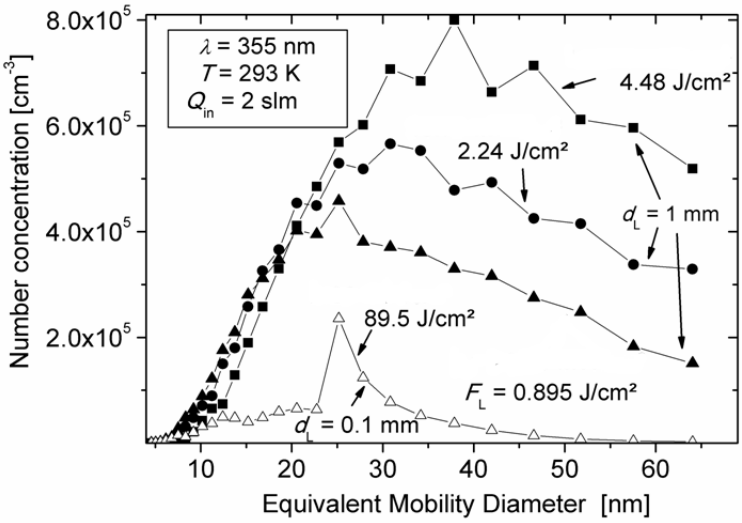

Figure 7.3.1.: The nanoparticle yield as function of the equivalent mobility diameter at different laser fluence measured with nanoDMA model TSI 3085.

number concentration over the full size range which might not be expected at first view. However, experiments from literature (Bäuerle [1996], p. 198) show that for laser spot diameters larger than 80 µm the ablation rate expressed as µm/pulse is constant. The reason for this is that the higher energy density does not arrive at the metal surface, as the energy is absorbed by the plasma above the target. Because of the smaller effective area in case of the smaller spot diameters, the total volume of the ablated material will be smaller, thereby leading to smaller particle sizes.

7.4. The influence of the volume flow of the carrier gas

From these results it has become clear that changing the laser fluence does not allow shifting the particle size distribution. However, for process optimization it is necessary to be able to optimize the particle number concentration at a given diameter. A common method for laser ablation synthesis is to change the process pressure (Ozawa et al. [2001]) which modifies the residence time and thereby the coagulation time. It was shown by these authors that in short-pulsed laser ablation from a tungsten rod at a fluence of 1.9 J/cm² in helium, the peak of maximum number concentration increased from

less than 10 nm to more than 80 nm while increasing the pressure from 8.6 to 67 kPa. However, this is costly as a suitable pumping capacity has to be made available. Furthermore, reducing the process pressure below atmospheric pressure leads to a reduced residence time in the thermal annealing section, which is problematic as a sufficient annealing time is necessary for the $L1_0$ phase formation (Stappert et al. [2003]). Because of these reasons atmospheric pressure was chosen for the system. The number size distribution can also be shifted by changing the carrier gas flow rate. In Fig. 7.4.1 the effect of changing this flow rate from 2 slm up to 15 slm is shown. In these measurements, the rDMA is operated with a flow rate of 2 slm and a sheath gas flow rate of 20 slm. The excess aerosol flow is led through a filter into the exhaust. The laser fluence is 0.895 J/cm² and the laser wavelength is 355 nm, as these conditions were shown in the proceeding section to be optimal for material stoichiometry and particle yield, respectively.

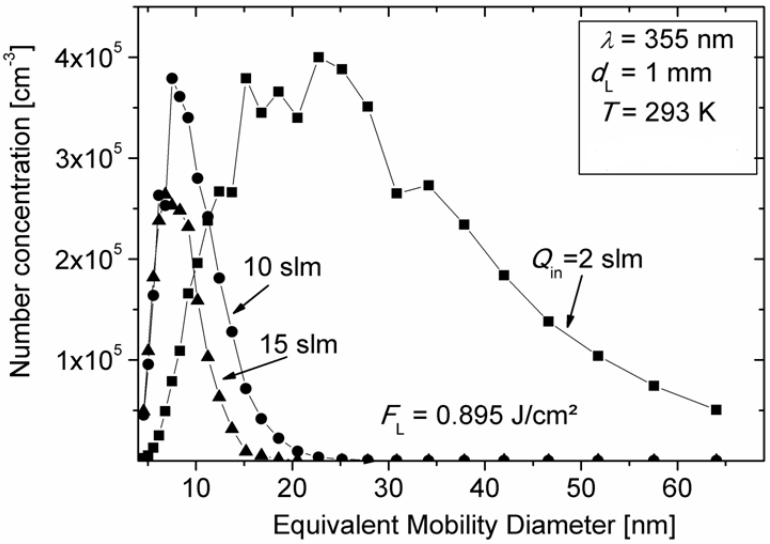

Figure 7.4.1.: The nanoparticle yield as function of the equivalent mobility diameter at different flow rates of the carrier gas.

It can be seen that changing the carrier gas flow rate is a suitable method for shifting the particle size distribution. When applying size selection as synthesis tool, the number concentration at the desired particle size before thermal annealing can be efficiently maximized by modifying the carrier gas flow rate. The particle size range which turned out to be relevant for the formation of well-defined $L1_0$ FePt nanocrystals resulted in an

optimal carrier gas flow rate around 2 slm for an equivalent mobility diameter from 10 till 20 nm. For the size range below 10 nm the higher flow rate of 10 slm was selected as optimal setting for the highest yield of sub-10 nm particles.

The optimal process configurations for laser ablation synthesis of FePt nanoparticles is complicated due to mechanisms such as charge effects and particle losses as well as instrumentation problems such as obtaining absolute process vacuum tightness. The strong oxidation tendency of the Fe atoms at high temperatures directly after the ablation pulse did not allow using commercially available DMAs as discussed previously and necessitated the use of a dedicated DMA which can be evacuated down to a vacuum level of 10^{-5} mbar and a closed-loop sheath gas system allowing the use of highly purified N_2 as carrier gas. The high-temperature thermal annealing step is under these conditions only possible using ceramic tubes having vacuum-tight connections. Ex-situ characterization showed that only the second harmonic of the pulsed Nd:YAG laser with a wavelength of 355 nm results in conservation of stoichiometry, the use of higher wavelengths, 512 nm or 1064 nm, leads to loss of stoichiometry at the same fluence and thus to material unsuitable for magnetic storage applications (ch. 7.2). Using the smaller wavelength also leads to smaller particle sizes so that a higher particle yield in the relevant size range is obtained. This can be explained by the reduced penetration depth of the laser beam at smaller wavelengths, leading to a smaller mass removal from the target rod. Investigations into the effect of laser fluence (ch. 7.3) showed that increasing the fluence did not improve the yield of sub-20 nm particles, but increased the yield of larger particles which is undesirable due to appearance of multiply charged particles in the size-fractionated aerosol. Very high fluences did not lead to significant amounts of nanoparticles due to the reduced irradiated area and plasma shielding effects. For optimizing the yield of sub-10 nm nanoparticles a substantial increase in carrier gas flow rate turned out to be the most effective.

For further laser ablation of FePt a wavelength of 355 nm, a fluence of 0.895 J/cm² and a laser spot diameter of 1 mm was set for a maximum yield of nanoparticles.

8. Size fractionation and on-flight annealing

8.1. Charge state after ablation

During the expansion and cooling of a plasma plume several physical processes are simultaneously taking place and result in a complex formation of particles. Kuroda et al. [2012] modelled particle generation in laser plasma at low pressure conditions. They found a dependency between particle growth and charging due to electrostatic coagulation. Choosing a sufficient distance away from the laser plume led to a balanced charge state of particles upstream the DMA in order to allow the selection of monodisperse nanoparticles. Since nanoparticles are classified on the basis of electrical mobility and monodisperse aerosol is required for size-dependent evaluation of magnetic properties multiply charged FePt nanoparticles need to be avoided. At a laser fluence of 0.895 J/cm² nanoparticles in the sub 30 nm range were generated. Figure 8.1.1 shows a tandem-DMA scan executed with two DMAs switched in series. In between those DMAs a radioactive source (^{85}Kr) was placed which bipolarly recharged the classified nanoparticles coming from DMA-1.

The radioactive source generates a well-known Boltzmann charge distribution f_{B} which was determined by Wiedensohler (1990) for the submicron range. The second DMA (nDMA, model 3085, TSI) was used in a SMPS (model 3080, TSI) which performs an inversion which results in the normalized number size distribution by assuming the charge distribution according to Wiedensohler which is given by

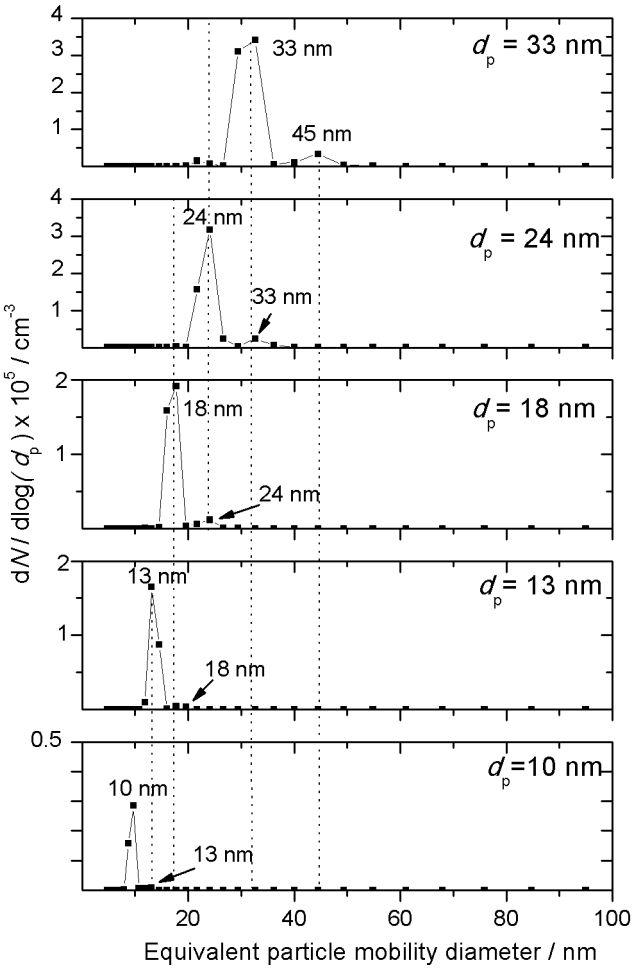

Figure 8.1.1.: Number size distributions measured with SMPS in a tandem-DMA configuration at different preselected particle diameters d_p being charged negatively

$$f_{\mathrm{ch}}(d_p, p) = 10^{\left[\sum_{i=0}^{5} a_i(p)\cdot(\log\ \frac{d_\mathrm{p}}{\mathrm{nm}})^i\right]} \tag{8.1.1}$$

with a_i as the approximation coefficients determined by Wiedensohler [1988] (see Tab. 8.1).

Table 8.1.: The approximation coefficients $a_\mathrm{j}$for non, singly and doubly charged nanoparticles according to Wiedensohler [1988].

	q				
$a_i(q)$	-2	-1	0	1	2
a_0	-26.3328	-2.3197	-0.0003	-2.3484	-44.4756
a_1	35.9044	0.6175	-0.1014	0.6044	79.3772
a_2	-21.4608	0.6201	0.3073	0.48	-62.89
a_3	7.0867	-0.1105	-0.3372	0.0013	26.4492
a_4	-1.3088	-0.126	0.1023	-0.1544	-5.748
a_5	0.1051	0.0297	-0.0105	0.032	0.5059

For a better understanding of the tandem DMA scan Fig. 8.1.2 is showing the different stages from laser ablation till SMPS. Laser ablation generates a plasma plume and simultaneously nanoparticles are emitted from the ablated region. The plasma plume ionizes the ambient gas molecules of the carrier gas nitrogen. The ions collide with the nanoparticles and transmit their electrical charge. The capability of nanoparticles to carry positive or negative electrical charges is limited by their surface area such that one finds a polydisperse particle size distribution containing nanoparticles with various electrical mobilities. By applying a voltage U_{DMA} at DMA-1 one selects positively or negatively charged nanoparticles (here positively) with a certain electrical mobility. Thereby, a discrete fraction of nanoparticles possessing a large surface area and carrying multiple charges possibly obtain the same electrical mobility as those ones with a smaller surface area and less number of charges. If the electrical mobility classified aerosol enters the SMPS nanoparticles are recharged by means of a radioactive source according to the charging probability determined by Wiedensohler [1988]. Now, one can find different electrical mobilities with a known charge distribution. The voltage at DMA-2 inside the SMPS is varied such that a range of different electrical mobilities is set and classified nanoparticles are counted by a condensation particle counter (CPC). The SMPS is determining a lognormal size distribution of nanoparticles as TDMA re-

sult, which exemplarily can be found in Fig. 8.1.1.

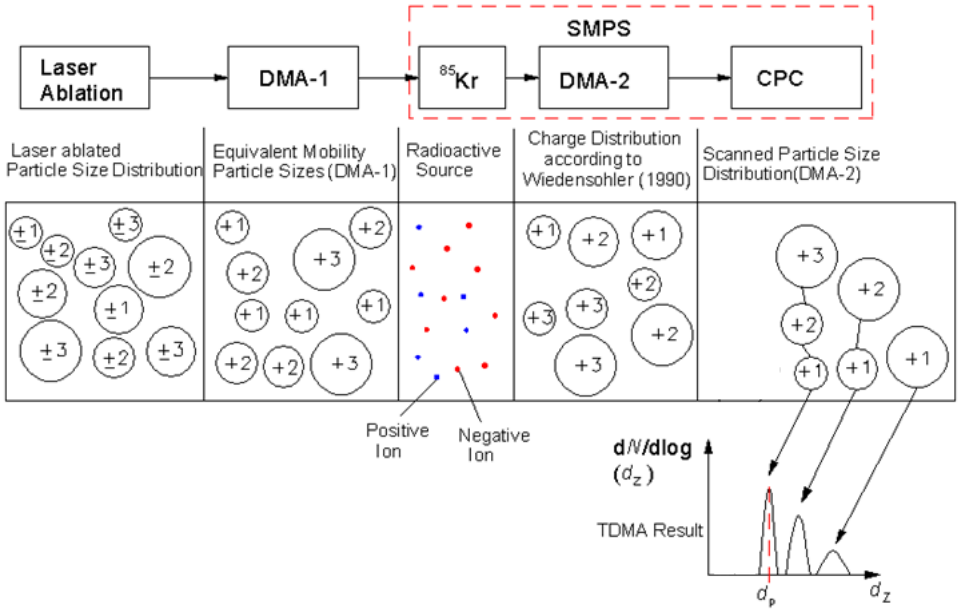

Figure 8.1.2.: The basic principle for the determination of charge distribution.

In order to clarify the determination of doubly charged fraction of nanoparticles as it is shown in Fig. 8.1.3 the following example shall be given. The aerosol after laser ablation and first DMA is composed of particles with diameters of 33 nm (p = -1) and undesired ones having 45 nm (p = -2). In order to calculate the fraction of 45 nm nanoparticles in this mixture, a numerical integration is performed over the particle size distribution measured by the SMPS:

$$f(45\,\mathrm{nm},\, p=-2) = \frac{\int_{d_{\mathrm{p,l}}}^{d_{\mathrm{p,u}}} \frac{dN}{d\log d_{\mathrm{p}}} d\log d_{\mathrm{p}}}{N} \tag{8.1.2}$$

where

$$N = \int_{d_p=0}^{\infty} \frac{dN}{d\log d_p} d\log d_p \tag{8.1.3}$$

The lower and upper bounds $d_{\mathrm{p,l}}$ and $d_{\mathrm{p,u}}$ can theoretically be determined by the transfer function of the first DMA, due to the limited resolution of the SMPS measurements the lower and upper bounds of the relevant peaks are taken.

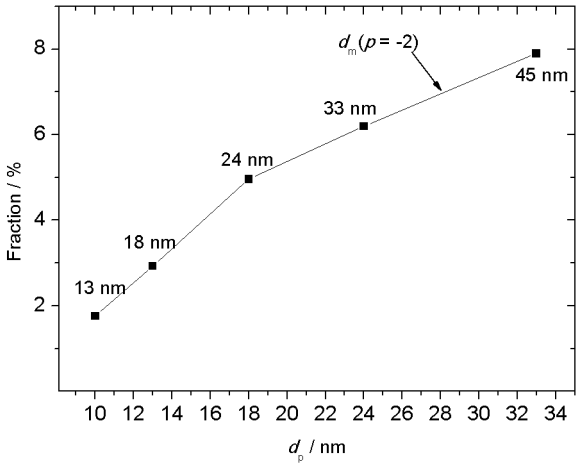

Figure 8.1.3.: Doubly charged fraction of particles with diameter d_{m} downstream the radioactive source (F_{L} = 0.895 J/cm²; λ = 355 nm; d_{L} = 1 mm; Q_{in} = 2 slm).

In Table 8.2 the electrical mobilities, charging probabilities and equivalent mobility diameters used in the experiments are listed for a better overview. A program was developed which allowed to predict possible particle diameter of multiple charged particles having the classified mobility and thus the position of the peaks of a tandem DMA scan as they are shown in Fig. 8.1.1. While the program scans through a range of particle diameter which are possible candidates for the peak positions of the tandem DMA scan an iterative procedure allows to find the electrical mobility which comes closest to the classified electrical mobility. After the scan the program lists the calculated peak diameter according to the smallest found deviation between calculated and classified mobility. The calculated and measured equivalent mobility diameter obtained behind the second DMA are listed and a good agreement can be found(see Table 8.2) . As an example for a preselected d_{p} of 33 nm (DMA-1) a peak at 23 nm is measured which represents the doubly charged particles with diameter 33 nm behind the radioactive source (Z_{p} = $4.11 \cdot 10^{-7}$ cm²(Vs)$^{-1}$; d_{p} = 33 nm; $p = -2$; $f_{\mathrm{B}} = 0.25\%$). On the other hand one can not detect peaks

if the charging probability f_B is close to zero.

In Fig. 8.1.3 the fraction of doubly charged preselected nanoparticles with equivalent mobility diameter d_m is shown over the desired particle diameter d_p. For example, one can expect a fraction of doubly charged particles with d_m= 45 nm of around 8 % if nanoparticles with d_p = 33 nm are selected with the first DMA. The further investigated selected particle size range up to 15 nm shows a relatively small fraction of less than 4% of doubly charged particles and thus sufficient monodispersity.

Table 8.2.: Overview over electrical mobilities, Boltzmann charging probabilities and equivalent mobility diameter used by SMPS for the determination of the normalized number size distribution. In the column DMA-2 peak one can find the calculated and measured mobility diameter.

Preselected electrical mobility DMA-1			Boltzmann charge distribution				DMA-2 peak d_m(nm)	
Z_p (cm²(Vs)$^{-1}$)	d_p(nm)	p(-)	Z_p (cm²(Vs)$^{-1}$)	d_p(nm)	p(-)	f_B(%)	Calculated	Measured
2.10E-06	10.0	-1	2.10E-06	10.0	-1	5.14	10.0	10.0
			4.21E-06	10.0	-2	0.00	7.1	-
		-2	1.05E-06	13.0	-1	7.54	13.2	13.4
			2.10E-06	13.0	-2	0.00	10.0	-
1.25E-06	13.0	-1	1.25E-06	13.0	-1	6.95	12.8	13.0
			2.51E-06	13.0	-2	0.00	9.0	-
		-2	6.27E-07	19.0	-1	10.41	18.2	18.1
			1.25E-06	19.0	-2	0.00	13.0	-
6.63E-07	18.0	-1	6.63E-07	18.0	-1	9.86	18.0	18.2
			1.33E-06	18.0	-2	0.00	13.2	-
		-2	3.32E-07	26.0	-1	13.99	25.0	24.9
			6.63E-07	26.0	-2	0.09	18.0	-
3.79E-07	24.0	-1	3.79E-07	24.0	-1	13.03	24.0	23.7
			7.58E-07	24.0	-2	0.06	17.2	-
		-2	1.90E-07	34.0	-1	17.40	34.0	33.8
			3.79E-07	34.0	-2	0.29	24.2	24.0
2.06E-07	33.0	-1	2.06E-07	33.0	-1	17.01	33.0	32.8
			4.11E-07	33.0	-2	0.25	23.0	22.9
		-2	1.03E-07	48.0	-1	21.80	48.0	47.5
			2.06E-07	48.0	-2	1.01	33.2	33.0

Measurements were repeated with preselected positively charged nanoparticles and similar TDMA scans were found within less than 3% deviation. Thus a bipolar charging can be expected by multiphoton excitation in the ablation process as already reported by Seto et al. (2001). Furthermore, it will not be necessary to recharge ablated FePt nanoparticles in order to obtain monodisperse aerosol in the sub 20 nm range at $F_L = 0.895$ J/cm².

8.2. Optimization of annealing conditions

On the one side a longer annealing time will have a positive influence on the formation of the $L1_0$ order. On the other side one has to consider the thermophoretic loss which always occurs when tube furnaces are used and a temperature gradient $\triangle T$ occurs at the thermal transition zone downstream of the furnace. Thus one has to find a compromise between obtaining a high yield of nanoparticles and a high fraction of $L1_0$ ordered FePt. In the following table the dimensions of the tested tubes are shown.

Table 8.3.: Heating tube parameters

Material	Heated length [mm]	Inner tube diameter [mm]
SiO_2	1300	80
Inconel	1300	139
Al_2O_3	390	18
Al_2O_3	600	54

Particle emission was observed experimentally by means of a sensitive particle counter which can detect number concentrations as low as 1 cm^{-3}. Heat resistive steel (Inconel) starts to emit particles from the tube walls at temperatures above 1073 K. Although yielding the longest annealing time it was found to be not suited for synthesizing FePt nanoparticles with high purity. The SiO_2 tubes start to emit particles at temperatures above 1173 K. Moreover, the tube material starts to soften at temperatures above 1223 K and the tube becomes instable. It was found that almost all charged FePt nanoparticles are deposited inside the tube if the temperature is above 1173 K. Thus the thermal energy must have caused a change in the electrostatic properties of the quartz tube which leads to an attraction of FePt towards the inner wall. Al_2O_3 tubes were found to be non-emitting tubes up to a temperature of 1673 K and thus the best choice for sintering nanoparticles at high temperatures.

Fig. 8.4 shows the thermophoretic loss Λ_{th} of FePt nanoparticles inside the prior mentioned furnace tubes measured as function of the furnace temperature T and particle diameter. The thermophoretic loss was determined using the following equation:

$$\Lambda_{\mathrm{th}}(T) = (1 - N_{\mathrm{A}}(T)/N_{\mathrm{A}}(T = 293K)) \cdot 100\% \tag{8.2.1}$$

with N_{A} the measured number concentration at the outlet of the furnace.

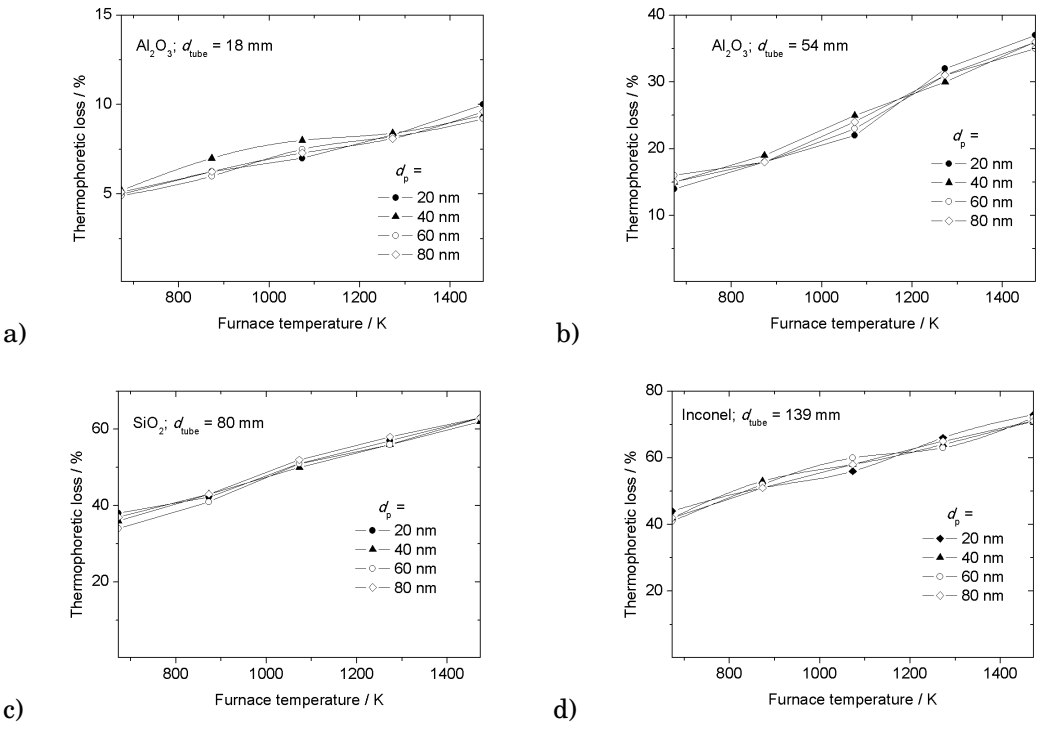

Figure 8.2.1.: Thermophoretic loss of size-selected FePt nanoparticles as function of equivalent particle diameter d_{p} and furnace temperature T for the different heating tubes tested. The residence time in the furnaces at 1073 K is a) 0.9 s, b) 13 s, c) 70 s and d) 160 s.

From these figures, the first noticeable result is that the losses seem to be size-independent in the measured particle size range 20 to 80 nm. This strongly points to thermophoresis being the main cause of losses, as diffusional losses as well as any losses due to electrostatic effects would have shown a clear particle size-dependency due to the fact that the electrical mobility Z_p is a function of the particle diameter. Therefore, the hypothesis of thermophoresis being the most probably loss mechanism seems to be justified as it is size independent as shown in ch. 5.2. It can also be seen that the thermophoretic losses increase with increasing furnace temperature, which is expected from the theory

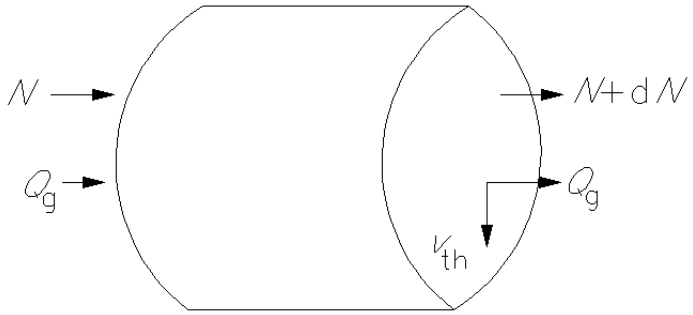

Figure 8.2.2.: Schematic for thermophoretic loss of nanoparticles inside a tube furnace

on thermophoresis. The most determining factor seems to be the residence time in the furnace, as the thermophoretic losses increase by a factor of 8 when the residence time is increased from 0.9 s to 160 s by moving from the smallest to the largest tube. In the following, the reason behind the strong influence of furnace residence time is discussed. A particle number balance is established for the particle concentration $N(z)$ at the axial position z:

$$Q_g \cdot N(z) = Q_g \cdot (N(z) + \mathrm{d}N(z)) \; + \; \pi \cdot d_{tube} \cdot v_{th} \cdot N(z) \; \cdot \mathrm{d}z \tag{8.2.2}$$

with dz the length element in axial direction of the tube, Q_g the volume flow rate of the gas and v_{th} the thermophoretic velocity perpendicular to the gas flow (see Fig. 8.2.2).

From this, the decrease of particle number concentration in an aerosol inside a tube due to thermophoresis can be estimated by means of

$$\frac{\mathrm{d}N(z)}{\mathrm{d}z} = - \frac{\pi \cdot d_{tube} \cdot v_{th}}{Q_g} \cdot N(z) \tag{8.2.3}$$

Here, v_{th} can be calculated by Hinds [1982]

$$v_{\mathrm{th}} = -K_{\mathrm{th}} \frac{\mu_g \nabla T}{\rho_g T} \tag{8.2.4}$$

where K_{th} is the thermophoretic coefficient, μ_g the gas dynamic viscosity and T the local temperature. Experimental observations indicate that K_{th} is equal to the free-molecular value of 0.55 for Knudsen numbers down to $Kn \approx 1$ (Messerer et al., 2003). In our experiments, $Kn > 1$ and therefore eq. 8.2.4 is used here.

Eq. 8.2.3 has to be solved numerically due to the locally varying temperature T and consequently temperature-depending parameters ρ_g, μ_g and Q_g. With the help of a commercial computational fluid dynamics software (Fluent 5.5), the twodimensional temperature profile of a heated tube was simulated. From the CFD solution, the centerline temperature T_{c} and the temperature in the gas adjacent to the wall T_w are obtained and fitted to a 5th order polynomial expression. The mean temperature in the gas at a given axial position is estimated as the arithmetic mean of wall and centerline temperature:

$$\overline{T}(x) = \frac{T_c(x) + T_w(x)}{2} \tag{8.2.5}$$

The temperature gradient ∇T in radial direction at a given axial position is calculated from standard engineering heat transfer theory for fully developed laminar flow (Talbot et al. 1980):

$$\nabla T(x) = \frac{\alpha}{\lambda_g} \left(T_w(x) - \overline{T(x)} \right) \tag{8.2.6}$$

where α the heat transfer coefficient, which can be calculated from the Nusselt number Nu:

$$\alpha = \frac{Nu\ \kappa_{\text{g}}}{d_{tube}} \tag{8.2.7}$$

For fully developed laminar flow with a given wall temperature $Nu = 3.66$. The CFD simulations were carried out for two different tubes, having with diameters 18 and 80 mm and the temperatures profiles. The above set of equations was numerically solved

with a solver for stiff differential equations , using the temperature information from the CFD simulation. The particles losses are calculated from $1-(N/N(0))$. The results are summarized in Table 8.4.

Table 8.4.: Comparison of experimentally measured and simulated thermophoretic losses in heated tubes

Tube diameter [mm]	Furnace temperature [K]	Thermophoretic losses [%]	
		Experimental	Model
18	1473	10.5	6.7
80	1173	50.9	29.7

It can be seen that the model predicts larger thermophoretic losses for the larger diameter tube, qualitatively in line with the experimental results as shown in Fig. 8.2.1 . The model seems to underestimate the losses by approx. 40%. Interestingly, as $\nabla T \propto \alpha$ and therefore $\nabla T \propto 1/d_{tube}$. Thus, $v_{th} \propto 1/d_{tube}$. Therefore, the decrease in particle number concentration $\frac{\mathrm{d}N(z)}{\mathrm{d}z}$ does not have a direct dependence on the tube diameter. However, the temperature profiles in the tubes are different. According to the CFD simulations, the larger diameter tube shows a larger gradient ∇T and this is the main reason for the observed increase in thermophoretic losses.

The simulation carried out implicitly assumes that the aerosol is well-mixed when leaving the heated zone. This is not entirely true, as the aerosol encounters a temperature gradient at the tube entrance in the opposite direction, i.e., leading to a thermophoretic velocity away from the tube wall. This might lead to the thermophoretic losses being in reality smaller than calculated when neglecting the entrance effects. This is not observed however. The most likely explanation is that turbulences and convective eddies occur at the tube entrance, where a small tube guides the aerosol into the large diameter furnace tube. This leads to a more homogeneous distribution of the particles in radial direction, countering the effects of thermophoresis away from the wall at the entrance zone. Furthermore, thermal diffusion inside the heated zone also further reduces the radial gradients of the particle concentration.

For a better understanding of heating tube losses one should add a model for the electrostatic effect causing increasing losses at higher temperatures as observed at the 80

mm SiO_2 tube. The electrostatic effect seems to be related to the electrical conductivity of the tube material at different temperatures. Since the tube furnaces are equipped with spiral-wound filaments it cannot be excluded that magnetic flux originated from the pulsed electrical current induces a voltage in the metallic tubes or causes a Lorentz force on the charged nanoparticles. Thus additionally a magnetodynamic effect may increase the loss of nanoparticles which seems to be reasonable as for higher temperatures larger currents are needed and a larger Lorentz force is caused.

8.3. Influence of annealing conditions on size and morphoplogy

Typically FePt nanoparticles appear in the shape of elongated agglomerates when they are leaving the laser ablation chamber. One finds primary particles often in sizes around 3 nm. Thus compaction of agglomerates by annealing is crucial for obtaining spherical FePt nanoparticles. If spherical FePt nanoparticles with different diameter are to be synthesized one has to investigate the compaction as function of temperature. This can be done by checking the shift of the number-based size distribution of electrical mobility-selected nanoparticles using the rDMA when passing through the tube furnace at different temperatures. Ablated FePt nanoparticles with preselected mobility diameter of d_{m} =20, 40, 60 and 80 nm were annealed on-flight in the finally chosen Al_2O_3 tube having an inner diameter of 18 mm and a heated length of 390 mm. As can be seen from Fig. 8.3.1 the equivalent mobility diameter does not change up to temperatures of 573 K. The degree of compaction increases with diameter being an indication for an increase of agglomeration for larger sizes. Whereas the compaction of FePt with initially d_{m} of 60 and 80 nm does not seem to be finished completely at a temperature of 1573 K the 20 and 40 nm tend to finish at 1173 K or 1373 K. The temperature where the compaction is finished is found at temperatures between 0.5 and 0.85 of the melting temperature, depending on the initial particle size, and is thus in contrast with the conclusions of Karlsson et al. [2005a] who found in a compilation of experimental results from literature that usually a temperature between 0.33 and 0.5 of the melting point is required for

full compaction. However, this consideration does not consider the time-dependency of the compaction. As sintering temperatures of 1573 K should not be exceeded for maintaining the ordered $L1_0$ state (see Fig. 2.2.1) preselected 60 and 80 nm FePt particles will not become spherical and are thus not suited for magnetic storage applications. As FePt nanoparticles with a particle diameter of above 20 nm tend to have the same ferromagnetic properties as the bulk material it is of more interest to further investigate the sub-20 nm particles. Fig. 8.3.2 illustrates the increasing compaction and transition of preselected 20 nm FePt at T = 293 K having the elongated appeareance towards elliptical(T = 873 K) and finally the spherical shape (T = 1273 K).

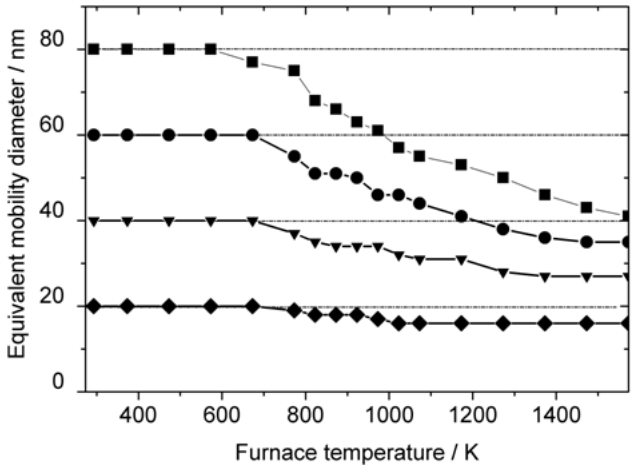

Figure 8.3.1.: Compaction of FePt nanoparticles. Mean equivalent mobility diameter is shown as function of the furnace temperature determined with SMPS TSI 3080(F_{L} = 0.895 J/cm²; λ = 355 nm; d_{L} = 1 mm; Q_{in} = 2 slm; Sintering tube Al_2O_3 d_{tube} = 18 mm, l_{tube} = 390 mm).

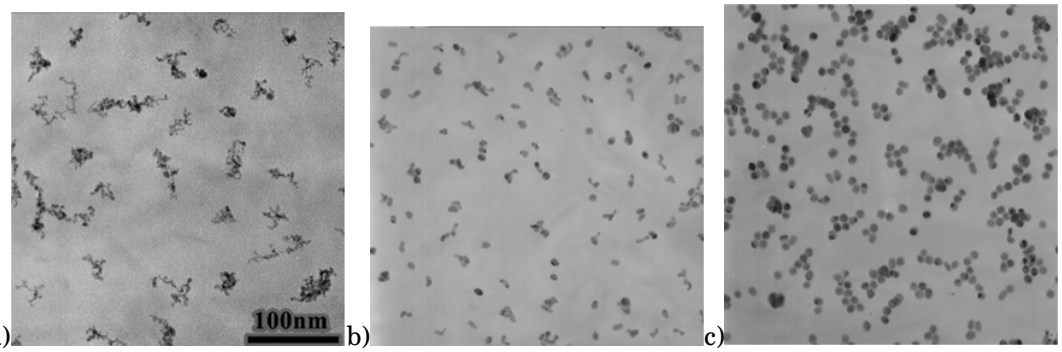

Figure 8.3.2.: TEM micrographs showing the compaction of FePt nanoparticles preselected by RDMA with d_{m} = 20 nm without annealing a) and after annealing at furnace temperatures of b) 873 K and c) 1273 K (F_{L} = 0.895 J/cm²; λ = 355 nm; d_{L} = 1 mm; Q_{A} = 2 lmin^{-1})(The length bar is valid for all three figures).

8.4. Thermal effects on nanoparticle charging

In order to obtain compact and spherical nanoparticles necessary for the magnetic storage it is mandatory to sinter the highly agglomerated particulate matter emitted by ablation. Moreover, the onset of $\mathrm{L1_0}$ phase formation will most probably be at temperatures in between 1000 and 1600 K at atmospheric pressure. First of all it was attempted to collect particles downstream the furnace with a proprietary built electrostatic precipator with TEM grid holder as it grants a softer and with respect to the fine structured mesh of the TEM grid a less destructive deposit in comparison to a low-pressure impactor. After some deposition a negligible amount of FePt nanoparticles was found if sintering temperatures above 1000 K were used. The ESP was operated at + or -8 kV with two parallel electrode plates having a distance of 10 mm granting well above 90 % deposition efficiency of charged nanoparticles in the size range 5 to 80 nm. So the thermal effect on nanoparticle charging was checked with the ESP and the number concentrations were measured behind the ESP switched on or off. From theory one has to consider the thermionic work function Φ of FePt as to estimate the loss of charges. According to the Richardson-Dushman equation (Michaelson [1977]) the emitted electron current density j is related to the absolute temperature T by the equation:

$$j = A_{\mathrm{R}} T^2 e^{\frac{-\Phi(T)}{kT}} \tag{8.4.1}$$

with the Richardson constant A_{R} ($= 1.2 \cdot 10^6 \frac{\mathrm{A}}{\mathrm{m^2\,K^2}}$ for FePt (Wolf [1995])) and

$$\Phi(T) = \Phi_0 + \frac{d\Phi}{dT}\,(T - 293\mathrm{K}) \tag{8.4.2}$$

where $\frac{d\Phi}{dT}$ is equivalent with the temperature coefficient $\alpha = -1.4 \cdot 10^{-3}\,\frac{\mathrm{eV}}{\mathrm{K}}$ and $\Phi_0 = \Phi(T = 293\,\mathrm{K}) = 7$ eV for FePt (Wolf [1995]).

The work function for Fe reaches values in the range from 4.67 to 4.81 and for Pt from 5.12 to 5.93 (Wolf [1995]).
The number of electrons emitted per FePt nanoparticle can be estimated via

$$n_e = \frac{j}{e} \cdot \pi \cdot d_{\mathrm{p}}^2 \cdot t_{\mathrm{res}} \tag{8.4.3}$$

with the assumption of having spherical particles and choosing an appropriate particle diameter d_{p} for a given temperature (see Fig.8.3.1). Since Fe has got a lower work function in comparison to Pt it should be the dominant emitter.
The mean residence time can be calculated by

$$t_{\mathrm{res}} = \frac{\pi}{4} \cdot d_{\mathrm{tube}}^2 \cdot l_{\mathrm{tube}} \cdot (Q_A \cdot (T/293K))^{-1} \tag{8.4.4}$$

The relevant residence times are listed in table 8.5.

Table 8.5.: Mean residence time of FePt nanoparticles in the heated region of the tube furnace.($Q_{\mathrm{A}} = 2$ lmin^{-1}; d_{tube}=18 mm; l_{tube} =390 mm)

Furnace temperature T [K]	t_{res}[s]
773	1.13
873	1.00
973	0.90
1073	0.81
1173	0.74
1273	0.69
1373	0.64
1473	0.59
1573	0.55

As can be seen from Fig. 8.4.1 the experimental results show that all preselected FePt nanoparticles increasingly seem to loose their charge. Under assumption of having predominantly singly and negatively charged nanoparticles one can simply determine the charged fraction by

$$\eta_{\mathrm{c,exp}} = 1 - n_u \tag{8.4.5}$$

with n_u the uncharged fraction of nanoparticles which passed the ESP being determined with the CPC.

The fitted thermionic workfunction of FePt as function of the furnace temperature (see Fig. 8.4.2) was determined under the assumption that n_e < 1 and thus the theoretically expected fraction of charged FePt nanoparticles is

$$\eta_{\mathrm{c,th}} = 1 - n_e \tag{8.4.6}$$

With known A_{R}, d_{p}, T and t_{res} Φ was found by an iterative procedure which determines the minimum of $\eta_{\mathrm{c,exp}} - \eta_{\mathrm{c,th}}$.

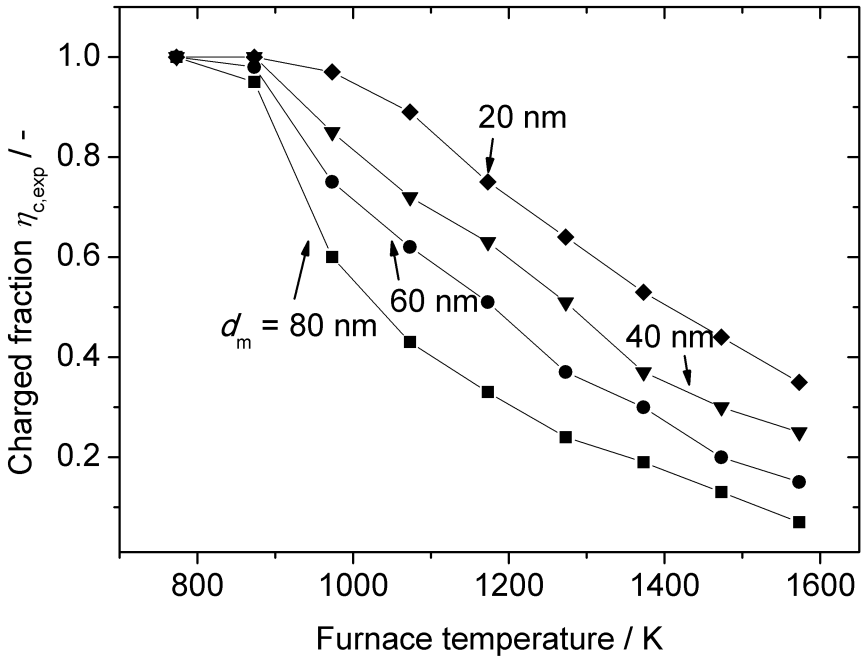

Figure 8.4.1.: The experimentally determined charged fraction $\eta_{c,exp}$ of primarily negatively charged FePt nanoparticles as function of different pre-selected mobility diameters and furnace temperatures. Number concentrations downstream the ESP were recorded with a CPC (TSI model 3775) with and without an applied voltage of 0 and 8 kV.

The work function of monomobile FePt nanoparticles is now determined according to the measured charged fraction and is plotted as function of the furnace temperature in Fig. 8.4.2.

Singly and negatively charged nanoparticles are assumed when entering the furnace thus emitting one electron would cause a neutral particle. Against theoretical expectations the work functions increase with temperature. It is most likely that minor impurities in the FePt nanoparticles cause such small values of the work functions as 2.9 eV at a temperature of 773 K. Such workfunctions may be contributed by alkali metals which increasingly evaporate with rising temperature until they are vanished and Fe becomes the dominant emitter (Peineke and Schmidt-Ott [2008]).

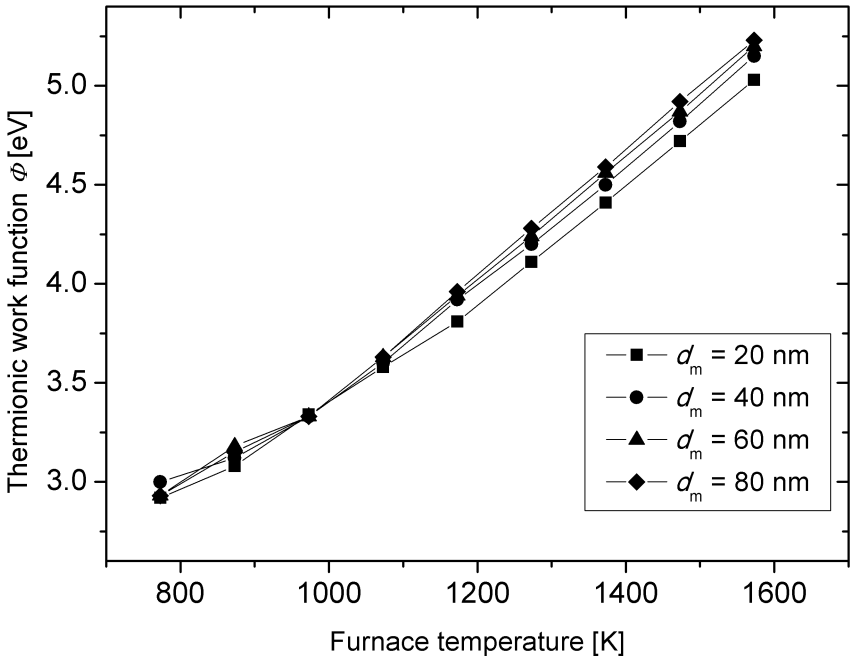

Figure 8.4.2.: The fitted thermionic workfunction Φ as function of furnace temperature T and preselected equivalent mobility diameter d_{m}determined from the experimental results shown in Fig. 8.4.1.

8.5. Monodispersity of particles by means of differential mobility analysis

For obtaining a representative evaluation of the magnetic properties of FePt with respect to different particle diameter the rDMA has to guarentee a geometric standard deviation of lower than 1.10 which is the general accepted limit for monodisperse nanoparticles. In order to assure spherical nanoparticles a sintering temperature of T = 1473 K was chosen. In Fig. 8.5.1 particles with sizes of d_{g}= 5, 10, 15 nm which are selected for further investigations are shown. The geometric mean diameter and standard deviation were measured by means of a SMPS model TSI 3080 and did not reach a value above 1.10.

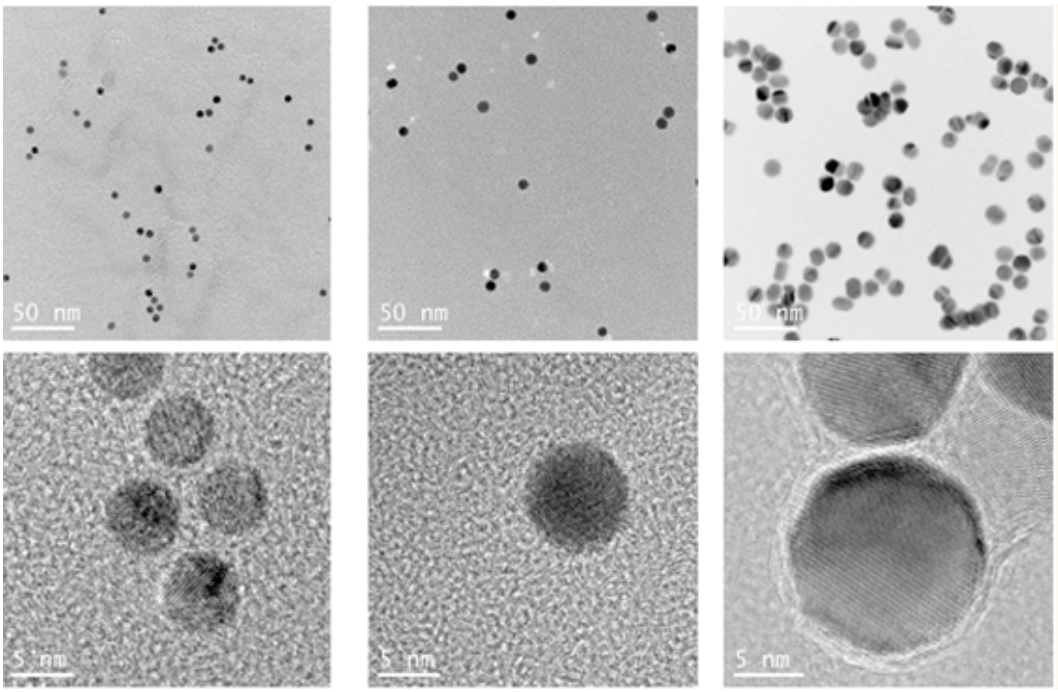

d_g = 5.3 nm
σ_g = 1.07

d_g = 10.0 nm
σ_g = 1.06

d_g = 15.0 nm
σ_g = 1.06

Figure 8.5.1.: A representative composition of TEM micrographs showing monodisperse FePt nanoparticles with different geometric mean diameters d_g and their geometric standard deviation σ_g determined via SMPS model TSI 3080 (F_L = 0.895 J/cm², λ = 355 nm, d_L = 1mm, Q_A = 2 slm and T = 1473 K).

Additionally, FePt nanoparticles of each preselected particle diameter were evaluated from TEM images and equivalent particle diameter was determined from the section area under assumption of spherical nanoparticles as already employed by Karlsson et al. (2006). First attempts to automatically evaluate the particle diameter with the image processing software ImageJ did not succeed due to erroneous detection of single nanoparticles. Sometimes nanoparticles were overlapping each other such that they were only detected as one nanoparticle. This lead to much bigger particle diameter which tampered the geometric standard deviation. Furthermore, it was difficult to select a certain number of pixels as threshold with respect to the smallest expected particle size. Thus finally the size of the nanoparticles was evaluated manually. Therefore an elliptical borderline was placed around each nanoparticle and the area was calculated by ImageJ by counting the number of pixels. A list of these determined areas was

evaluated by means of a macro written in Visual Basic. The results can be found in Fig. 8.5.2 where separately geometric and arithmetic mean diameter and standard deviation both geometric and arithmetic are listed.

The arithmetic standard deviation is defined as

$$\sigma = \sqrt{\frac{1}{n_p}\sum_{i=1}^{n_\mathrm{c}} \left(\left(d_{\mathrm{p,i}} - d_{\mathrm{arit}}\right)^2 \cdot n_\mathrm{i} \right)} \tag{8.5.1}$$

where n_p is the total number of counted nanoparticles, $n_\mathrm{c}$is the number of classes of particle diameter, $d_{\mathrm{p,i}}$is the classified equivalent particle diameter, n_i is the number of particles with a classified equivalent particle diameter and d_{arit} the arithmetic mean particle diameter being calculated by

$$d_{\mathrm{arit}} = \sum_{i=1}^{n_\mathrm{c}} \frac{n_i \cdot d_{p,i}}{n_\mathrm{p}} \tag{8.5.2}$$

On the other hand one also can determine the geometric standard deviation which is defined as

$$\sigma_g = \exp\left[\sqrt{\frac{\sum_{i=1}^{n_\mathrm{c}} n_i \cdot [\ln d_{p,i} - \ln d_g]^2}{n_\mathrm{p} - 1}}\right] \tag{8.5.3}$$

where the geometric mean diameter d_g is

$$d_\mathrm{g} = \exp\left[\sum_{i=1}^{n_\mathrm{c}} \left(\frac{n_i \cdot \ln(d_{p,i})}{n_\mathrm{p}}\right)\right] \tag{8.5.4}$$

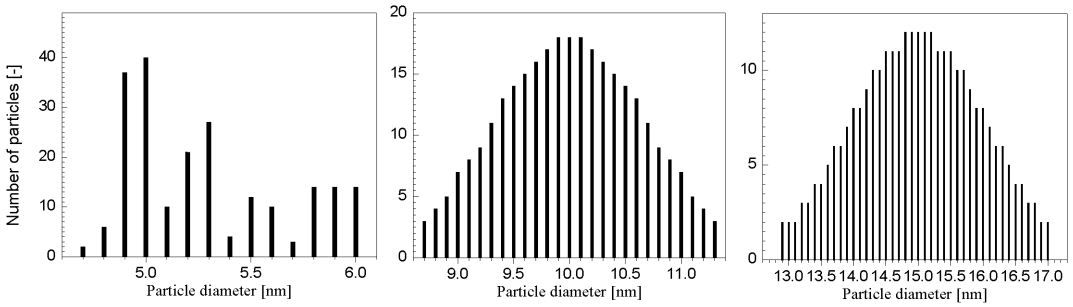

Figure 8.5.2.: Determination of number size distribution via image processing. The projected area of a FePt nanoparticle was used for the determination of its equivalent particle diameter.

Table 8.6.: The geometric and arithmetic mean diameter and deviation from Fig. 8.5.2 with number of observed nanoparticles and classes obtained from image processing and SMPS measurement.

Image processing						SMPS	
n_{p}[-]	n_{c}[-]	d_{g}[nm]	σ_g[-]	d_{arit}[nm]	σ[-]	d_{g}[nm]	σ_g[-]
201	14	5.3	1.07	5.3	0.07	5.3	1.07
298	27	10.0	1.06	9.9	0.06	10.0	1.06
301	42	15.0	1.06	15	0.14	15.0	1.06

Comparing SMPS and image processing results one can find a good agreement considering the geometric mean diameter and standard deviation (see Tab. 8.6) . The required σ_g of less than 1.10 for monodispersity is clearly reached. A σ_g of 1.07 leads to a narrow particle diameter range from 4.7 till 6.0 nm for a d_{g} of 5.3 nm whereas a σ_g of 1.06 for a d_{g} of 10.0 nm or 15.0 nm leads to possible diameter ranges between 8.7 and 11.3 nm or 12.9 and 17 nm. Thus magnetic properties found by SQUID measurements can be addressed more precisely to 5.3 nm FePt nanoparticles followed by 10.0 nm and 15.0 nm. However, precision is limited due to the transfer function of a DMA in general as mentioned in ch. 4 and not only having singly charged nanoparticles after laser ablation. A further argument not to evaluate nanoparticles above 15 nm is the increasing range with increasing particle diameter.

The expected Gaussian distribution of size-selected particles can be found in case of d_{g} = 10.0 and 15.0 nm where diffusion becomes less dominant. Summarizing, the method of

size classification via electrical mobility allows further investigation of size-dependent magnetic properties of FePt. Laser ablation generates already charged nanoparticles thus having no need for additional chargers in the aerosol line.

9. Ordering state and magnetic properties of FePt nanoparticles

9.1. Particle crystallinity

The most important parameter for obtaining a large fraction of $L1_0$ ordered FePt nanoparticles is the annealing temperature. Rietveld refinement was performed on data obtained from HRTEM SAED of monodispersed nanoparticles. The fraction of $L1_0$ order was obtained for a particle diameter of 10 and 15 nm. As compared to 10 and 15 nm FePt particles, diffraction patterns of 5 nm FePt nanoparticles were difficult to evaluate since discrete diffraction rings pointing out the possible crystal phases for the ordered state were diffuse and broadened due to the small particle size (see Fig. 9.1.1).

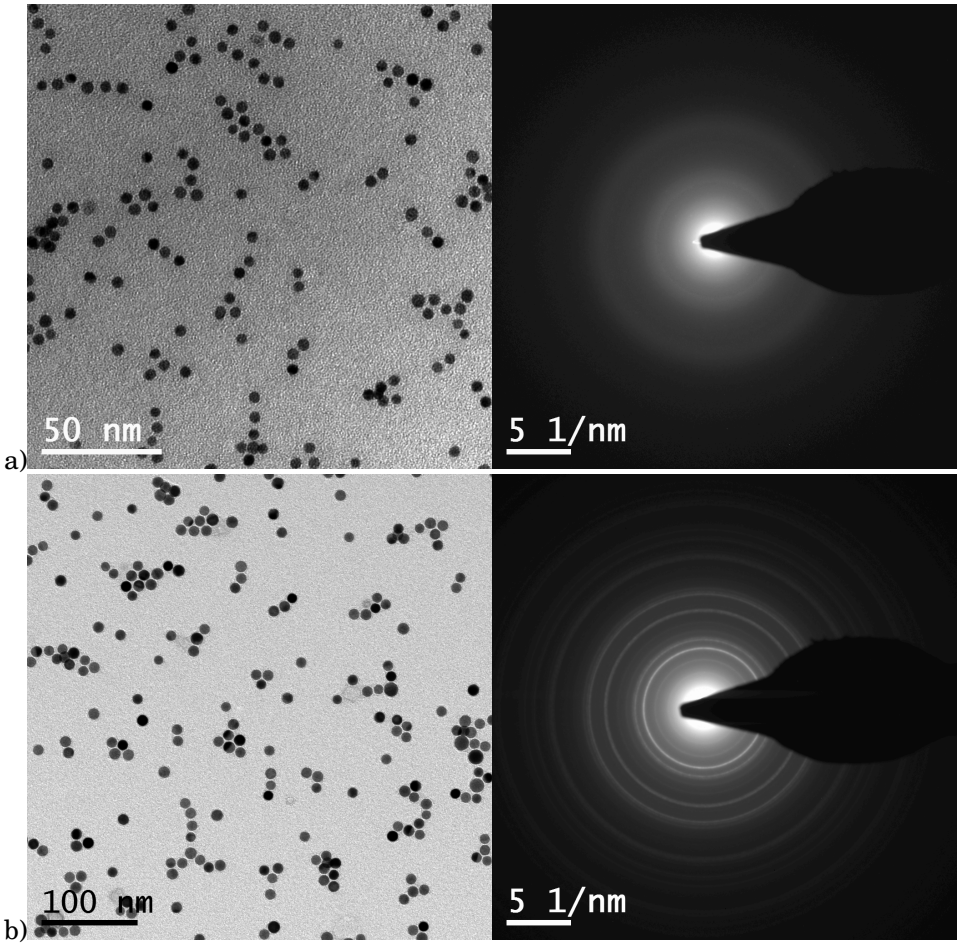

Figure 9.1.1.: HRTEM images (left) and SAED diffraction pattern (right) of a) 5 nm and b) 10 nm FePt nanoparticles being annealed at a temperature of T = 1373 K.

Thus evaluation of the data of 5 nm FePt nanoparticles would be accompanied by large errors. However, one can observe an increase of ordering with increasing sintering temperature inside the tube furnace as can be seen from Fig. 9.1.2. The percentage of $L1_0$ fraction is more than 80 % for the highest temperature, and seems to be comparable for FePt nanoparticles having a particle diameter of 10 and 15 nm.

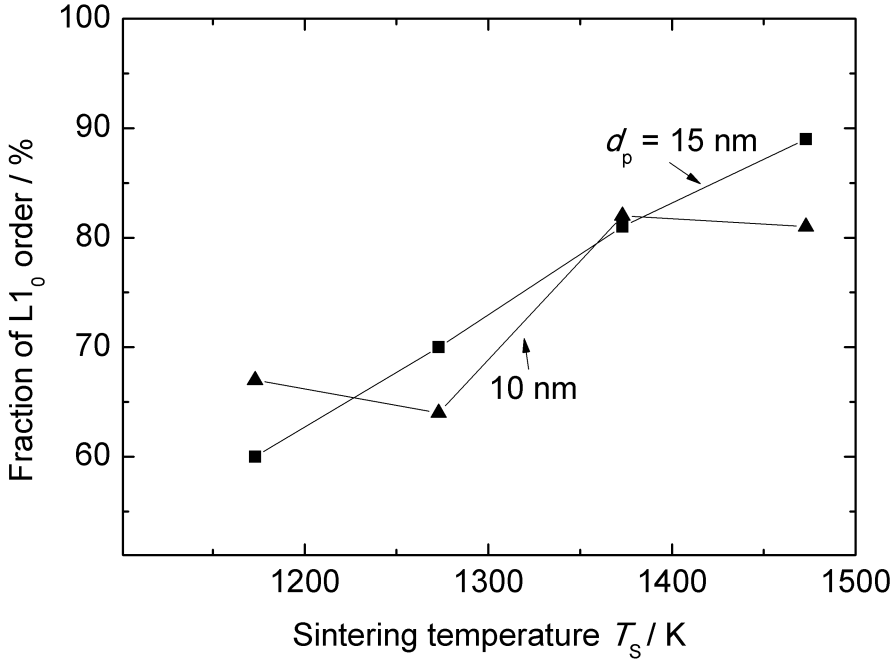

Figure 9.1.2.: The $L1_0$ fraction of d_p = 10 and 15 nm FePt nanoparticles under variation of sintering temperature. Ordering state was determined via Rietveld refinement of SAED images obtained from HRTEM.

In Fig. 9.1.3 a linescan of a single 10.0 nm FePt nanoparticle was executed by means of a STEM equipped with EDX and (EELS). One recognizes the effect of the alternating Fe and Pt atomic layers. Having a high scanning resolution of 0.1 nm EDX shows clearly the transition from a Fe towards a Pt layer. A minimum of intensity for Fe appears if a maximum of Pt is reached and vice versa. The lattice constant a as determined from the distance between the lattice planes is equivalent with $d_{100} = 3.87$ Å which is close to the value of 3.85 Å as listed from JCPDS [1995].

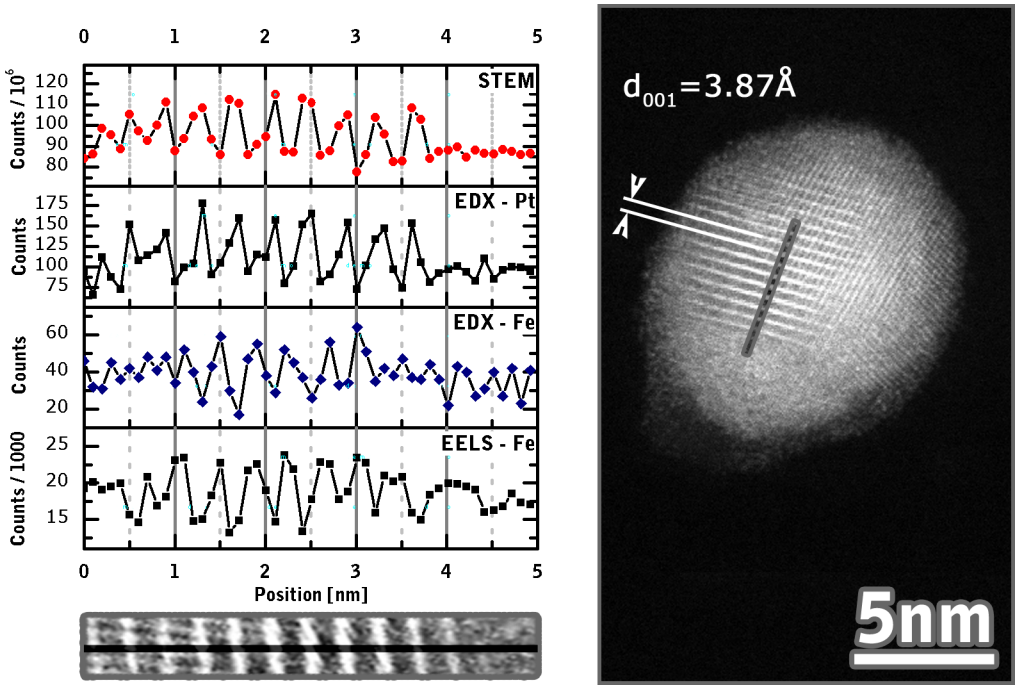

Figure 9.1.3.: STEM, EDX and EELS linescan (left) of a 10 nm FePt nanoparticle (right) being annealed at T = 1373 K.

Fig. 9.1.4 shows a collage of 15.0 nm FePt nanoparticles being annealed at 1273 K and points out the appearance of crystal defects generated due to random coagulation and subsequent sintering of FePt primary particles having a particle diameter up to 5 nm. For instance one can observe two-dimensional defects such as stacking faults resulting in twin borders as shown at Fig. 9.1.4c) which could have been emerged from two coagulated primary particles being sintered together and finally being shaped spherically due to surface tension. In Fig. 9.1.4 d) one can observe a polycrystalline multiple twinned nanoparticle with sub-grain boundaries which could have been formed out of several primary particles. This nanoparticle may consist mainly out of crystallites where the $L1_0$ phase is formed. However different crystal orientations will also cause different directions of the easy axis of magnetization in each crystallite. Although Rietveld refinement indicates a large fraction of $L1_0$, it does not necessarily indicate a large coercive magnetic field strength as it results out of a combination of all magnetic moments of the entire FePt probe. Crystal defects such as twin borders form an energetically stable transition between crystallites. Thus it will become difficult to form monocrystalline

nanoparticles which are larger than the primary particle size via grain boundary, surface or volume diffusion. So another reason for prefering 5 nm FePt next to achieving a high density magnetic storage could be the appearance of less crystal defects.

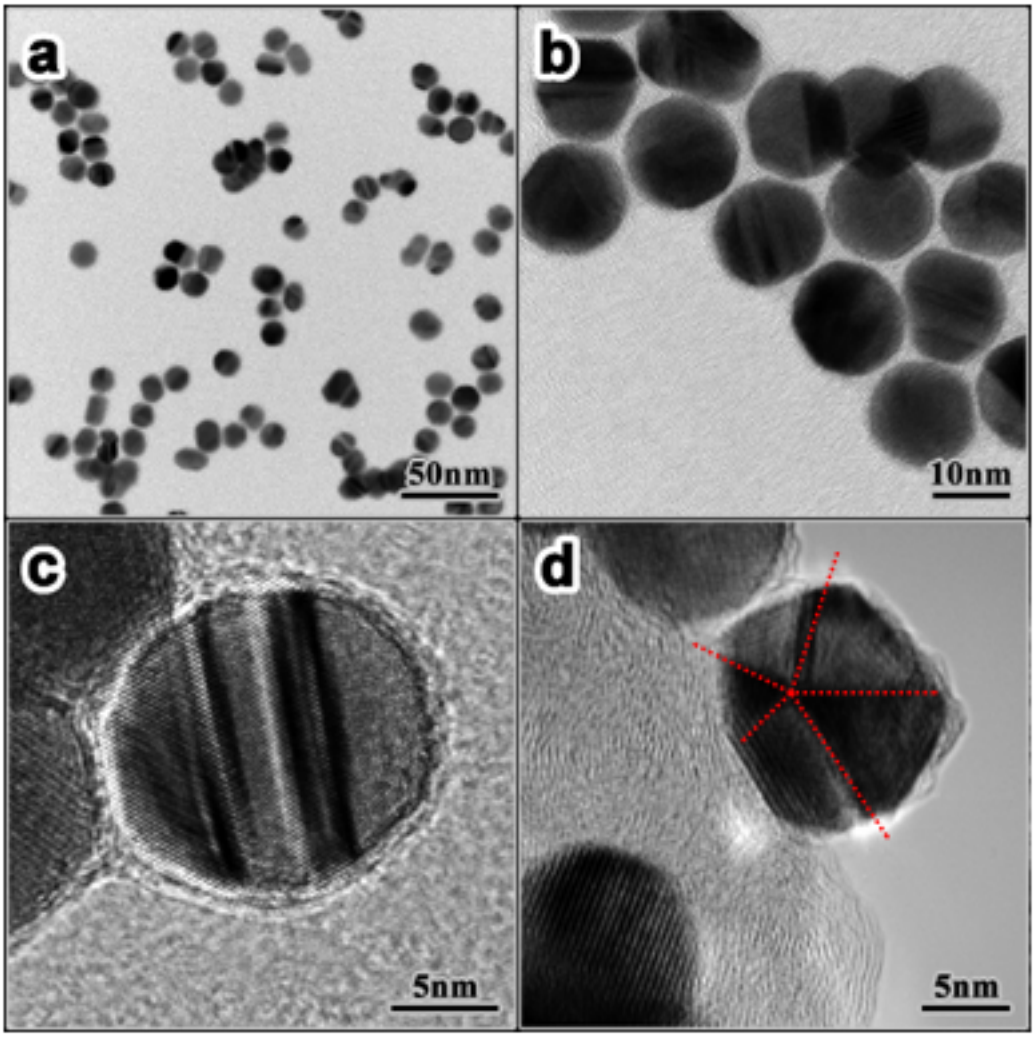

Figure 9.1.4.: A collage of TEM micrographs with FePt nanoparticles (d_p = 15 nm, σ_g = 1.06) at different resolutions showing the appearance of twin borders (b,c) and the formation of polycrystalline multiple twinned particles (transition of twinned border lines marked with red dotted lines)(d).

Table 9.1.: Process parameters being used for obtaining the three generated probes being used for magnetic evaluation (F_{L} = 0.895 J/cm², λ = 355 nm, d_{L} = 1mm and T = 1273 K). The number of deposited monolayers is 6.2 for all SQUID probes. The geometric mean diameter is listed for the case before and after sintering inside the tube furnace.

U_{DMA}[kV]	Q_{in}[l min^{-1}]	d_{g}[nm]		σ_g[-]	N_T [-]
		before	after		
0.5	15.0	6.0	5.3	1.07	$11.43 \cdot 10^{11}$
1.0	2.0	11.1	10.0	1.06	$2.526 \cdot 10^{11}$
1.5	2.0	17.2	15.0	1.06	$1.0656 \cdot 10^{11}$

9.2. Magnetic properties

For the final magnetic evaluation of monodispersed FePt nanoparticles potentially offering the highest $\mathrm{L1_0}$ fraction, SQUID probes of 5.3, 10.0 and 15.0 nm nanoparticles were prepared as described in ch. 6.3. After correction for the counting efficiency of the CPC TSI 3775 of η_{CPC}= 0.7, 0.95 and 1 for 5.3, 10.0 and 15.0 nm nanoparticles and the mentioned deposition efficiencies η_{LPI} of the custom built low-pressure impactor the total amounts of deposited FePt nanoparticles are $N_{\mathrm{T}}(d_{\mathrm{p}}$ =5.3 nm) = $11.43 \cdot 10^{11}$, $N_{\mathrm{T}}(d_{\mathrm{p}} = 10.0\,\mathrm{nm}) = 2.526 \cdot 10^{11}$ and $N_{\mathrm{T}}(d_{\mathrm{p}} = 15.0\,\mathrm{nm}) = 1.0656 \cdot 10^{11}$ as shown in Tab. 9.1.

Tab. 9.1 gives an overview of used process parameters for the three generated probes being used for magnetic evaluation via SQUID.

For obtaining the appropriate mass of the given number of nanoparticles one has to determine the density of $\mathrm{Fe_{53}Pt_{47}}$ as derived in the following:
With given lattice constants a = 3.852 $\overset{o}{\mathrm{A}}$ and c = 3.728 $\overset{o}{\mathrm{A}}$ at T = 293 K (JCPDS [1995], Klemmer et al. [2002]) the volume of a unit cell is determined by

$$V_{uc} = a^2c = 55.32\,\overset{o}{\mathrm{A}}^3 = 5.532 \cdot 10^{-23}\ \mathrm{cm}^3 \tag{9.2.1}$$

The molar mass of $\mathrm{Fe_{53}Pt_{47}}$ is 121.29 g. As a unit cell consists of 4 atoms one obtains $n_{\mathrm{a}}/4$ = $1.51 \cdot 10^{23}$ unit cells per mole. Thus the molar volume becomes

$$V_{\mathrm{m}} = V_{\mathrm{uc}} \cdot \frac{n_{\mathrm{a}}}{4} = 8.353\,\mathrm{cm}^3 \tag{9.2.2}$$

Finally the mass density of $Fe_{53}Pt_{47}$ is $\rho = 121.29\,\mathrm{g}\,/8.353\,\mathrm{cm}^3$ = 14.52 g/cm³.

The measurand obtained from SQUID measurement is not directly the amount of an individual atomic magnetic moment μ_{a}. It is the sum of all atomic moments in the sample. The total magnetic moment has in the sense of thermodynamics the character of an extensive state variable. Thus doubling the volume of a sample means doubling the number of individual atomic moments and thereby the total magnetic moment. The relation between the measurand - the total magnetic moment μ_{m} of a SQUID sample- and the norm M_{m} of the magnetization $\vec{M}_{\mathrm{m}}$ is given by

$$\mu_{\mathrm{m}} = \int M_{\mathrm{m}} dV \tag{9.2.3}$$

whereby integration ranges over the volume of the magnetic sample. In other words, M_{m} can be understood as the density of magnetic moments (magnetic moment per volume) and accordingly it has the unit Am^{-1}. Assuming a homogenous magnetic material with known mass and mass density one can calculate the magnetization M_{m} out of experimental data for the magnetic moment (in emu or Am² with 1 emu $\equiv 10^{-3} Am^2$).

One could assume a sphere as approximation for a single FePt nanoparticle. The volume of a spherical nanoparticle is

$$V_{\mathrm{SP}} = \frac{1}{6}\pi\, d_p^3 \tag{9.2.4}$$

Since the number size distribution of size selected nanoparticles can be approximated by a lognormal distribution one could apply the lognormal density function for the determination of the total mass of a FePt sample (see also Hinds [1982]). The log normally distributed density function can be expressed by

$$f_{\mathrm{LN}}(d_{\mathrm{p}}) = \frac{1}{\sqrt{2\pi} \cdot d_g \cdot \ln \sigma_g} \exp(-\frac{\ln(d_{\mathrm{p}}/d_{\mathrm{g}})^2}{2 \ln^2 \sigma_g}) \tag{9.2.5}$$

The number of particles having a sampled particle diameter can be estimated by

$$n_{\mathrm{p}}(d_{\mathrm{p}}) = N_{\mathrm{T}} \cdot f_{\mathrm{LN}}(d_{\mathrm{p}}) \tag{9.2.6}$$

The mass of sampled FePt nanoparticles with diameter d_{p} can be determined by

$$m_{\mathrm{FePt}}(d_{\mathrm{p}}) = \rho \cdot V_{\mathrm{SP}}(d_{\mathrm{p}}) \cdot n_{\mathrm{p}}(d_{\mathrm{p}}) \tag{9.2.7}$$

For obtaining the total mass of a sample one has to integrate the masses of fractionated particles:

$$m_{\mathrm{T}} = \int_{d_{\mathrm{p,l}}}^{d_{\mathrm{p,u}}} m_{\mathrm{FePt}}(d_{\mathrm{p}})\, dd_{\mathrm{p}} \tag{9.2.8}$$

By combining prior listed equations one obtains the following integral

$$m_{\mathrm{T}} = \frac{\rho\sqrt{\pi} \cdot N_{\mathrm{T}}}{6\sqrt{2} \cdot d_{\mathrm{g}} \cdot \ln \sigma_{\mathrm{g}}} \int_{d_{\mathrm{p,l}}}^{d_{\mathrm{p,u}}} d_{\mathrm{p}}^2 \cdot \exp(-\frac{\ln\left(d_{\mathrm{p}}/d_{\mathrm{g}}\right)^2}{2 \ln \sigma_g^2})\, dd_{\mathrm{p}} \tag{9.2.9}$$

Another possibility is the discrete summation of masses with help of Fig. 8.5.2:

$$m_{\mathrm{T}} = \frac{N_{\mathrm{T}} \cdot \rho \cdot \pi}{N_{\mathrm{S}} \cdot 6} \sum_{i=1}^{n_{\mathrm{dp}}} d_p^3(i) \cdot N_i \tag{9.2.10}$$

with N_i as the number of nanoparticles having a particle diameter $d_{\mathrm{p}}(i)$ and n_{dp} the number of different particle diameter.

Now, magnetization M_{m} can be estimated by

$$M_{\mathrm{m}} = \frac{\mu_{\mathrm{m}}}{m_{\mathrm{T}}} \cdot \rho \tag{9.2.11}$$

Without knowing the mass density ρ of the probe one could also use

$$M_{\mathrm{m}} = \frac{N_{\mathrm{S}} \cdot 6}{N_{\mathrm{T}} \cdot \pi} \frac{\mu_{\mathrm{m}}}{\sum_{i=1}^{n_{\mathrm{i}}} d_p^3(i) \cdot N_i} \tag{9.2.12}$$

With eq. 9.2.10 one obtains masses of $m_{\mathrm{T}}(d_g$=5 nm) = 1.39 μg, $m_{\mathrm{T}}(d_g$=10 nm) = 1.94 μg and $m_{\mathrm{T}}(d_g$=15 nm) = 2.77 μg.

There are two possibilities to estimate the background signal which mainly comes from the plastic straw and adhesive tape used as particle carrier inside the SQUID. First one is the direct determination of the magnetic properties of the straw through SQUID measurement as it is exemplarily shown in Fig. 9.2.1. Second one is the estimation of the background signal by a linear fit of the magnetically saturated section of the superposed magnetic hysteresis loops as it is shown by the red line added to the hysteresis loop of the magnetic moment being a function of the externally applied magnetic field in Fig. 9.2.4. Both possibilities were tested and good agreement was found, so that the linear fit was done for the rest of measurements in order to skip the SQUID measurements of the used straws.

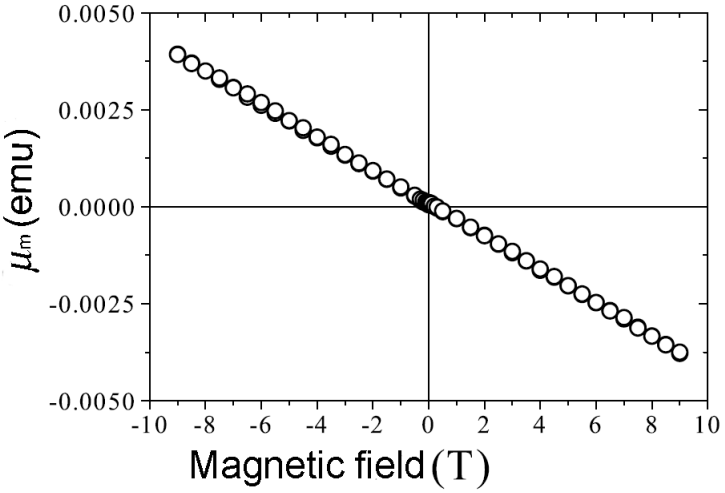

Figure 9.2.1.: Magnetic moment μ_m as function of the applied magnetic field obtained from a diamagnetic plastic straw used as carrier for a FePt sample.

Fig. 9.2.2 up to 9.2.4 show the SQUID measurements of layers of 5, 10 and 15 nm FePt nanoparticles annealed at 1273 K at chamber temperatures of 5, 6 and 300 K. The red curve is presenting the corrected hysteresis loop after subtraction of the background signal. For 5, 10 and 15 nm FePt nanoparticles one can find magnetisation curves which clearly show the presence of ferromagnetic nanoparticles and thus a successful generation of carriers for ultra high density data storage. With increasing ambient temperature from 5 till 300 K one can observe the typical decrease of the area enclosed by the hysteresis loop which is an indicator for the stored magnetic energy of the FePt sample. The decrease of magnetic energy is due to the increasing thermal fluctuation of magnetic moments of the samples. As can be seen from Fig. 9.2.5 the data storage composed out of FePt nanoparticles could withstand externally applied magnetic field strengths being equivalent with the coercive field strength H_c of 11.5 kOe, 10.2 kOe and 8 kOe in case of 5, 10 and 15 nm nanoparticles at an ambient temperature of 300 K. A comparison with other results, e.g. such as obtained from Kawai et al. [2005] or Luong et al. [2005], who reported about a high coercive field strength of 17 kOe of a 68 nm thin film of FePt at room temperature, is difficult as those films were composed out of polydisperse nanoparticles since they did not apply a fractioning method but directly deposited sputtered FePt nanoparticles onto a heated substrate. However, as the prepared sam-

ples of monodisperse nanoparticles had film thicknesses of seven monolayers it would mean that with a particle diameter of 5 nm one obtains roughly an effective thickness of 35 nm. So in this case 11.5 kOe would become reasonable if compared with 17 kOe at 68 nm thickness and roughly a change of coercive field strength of 0.25 kOe/nm. Furthermore, looking at Fig. 9.2.5 one finds a much smaller temperature dependancy of the coercive field in case of nanoparticles having a particle diameter of 5 nm and 10 nm than compared to 15 nm. Thus one can expect that ultrahigh-density storage films with 5 nm nanoparticles would offer the highest stability at varying ambient temperatures.

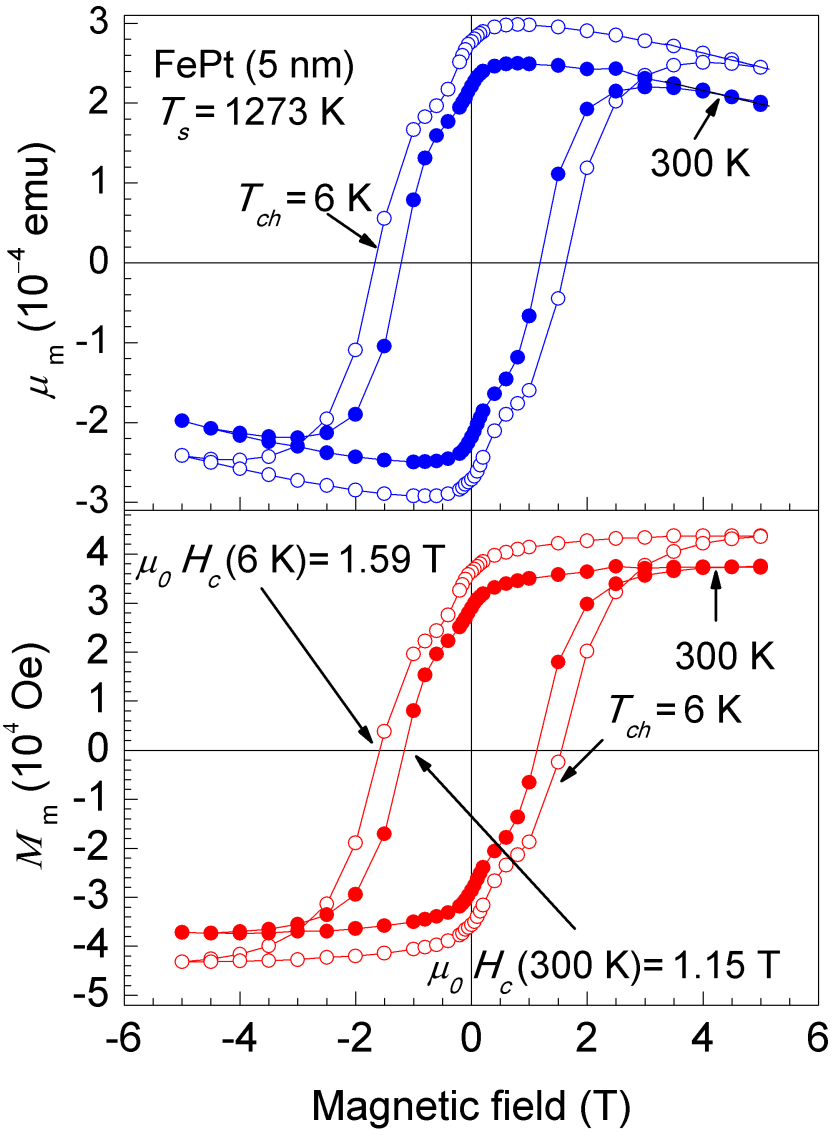

Figure 9.2.2.: Magnetic hysteresis loops obtained from SQUID measurements (Quantum Design MPMS) of 5 nm FePt nanoparticles annealed at 1273 K. SQUID probe was prepared on a plastic straw as explained in ch. 6.4. The blue curve is the magnetic moment directly obtained from SQUID measurement and the red curve shows magnetisation obtained after correction of magnetic moment (10^3 emu = 1 Am²; 0.012566371 Oe = 1 Am^{-1}).

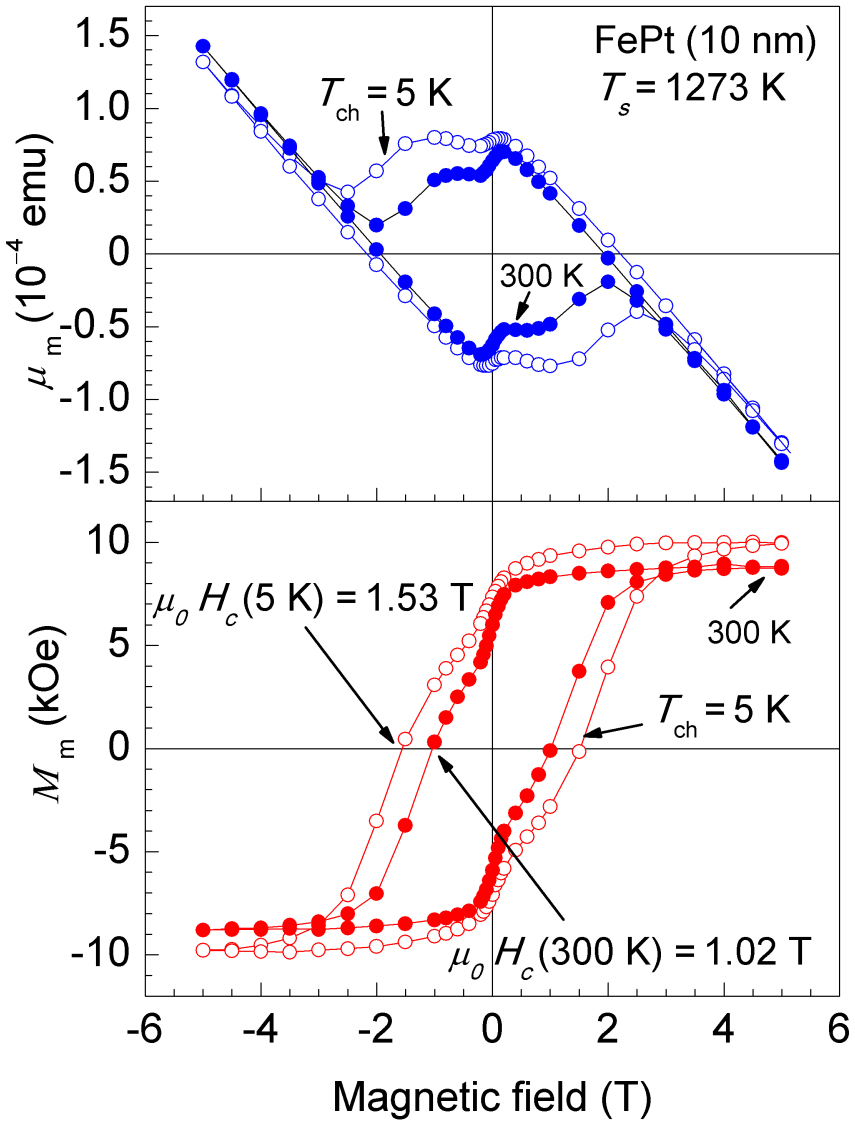

Figure 9.2.3.: Magnetic hysteresis loops obtained from SQUID measurements (Quantum Design MPMS) of 10 nm FePt nanoparticles annealed at 1273 K. Further details as in Fig. 9.2.2.

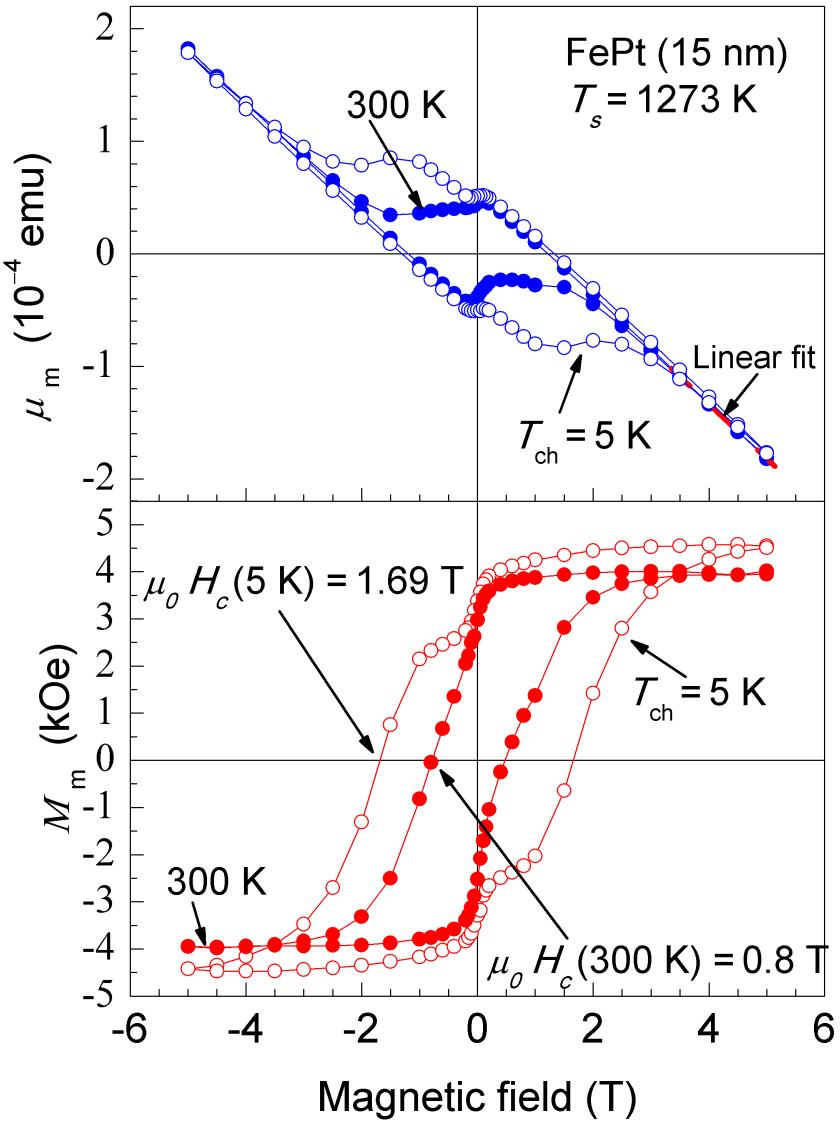

Figure 9.2.4.: Magnetic hysteresis loops obtained from SQUID measurements (Quantum Design MPMS) of 15 nm FePt nanoparticles annealed at 1273 K. Further details as in Fig. 9.2.2.

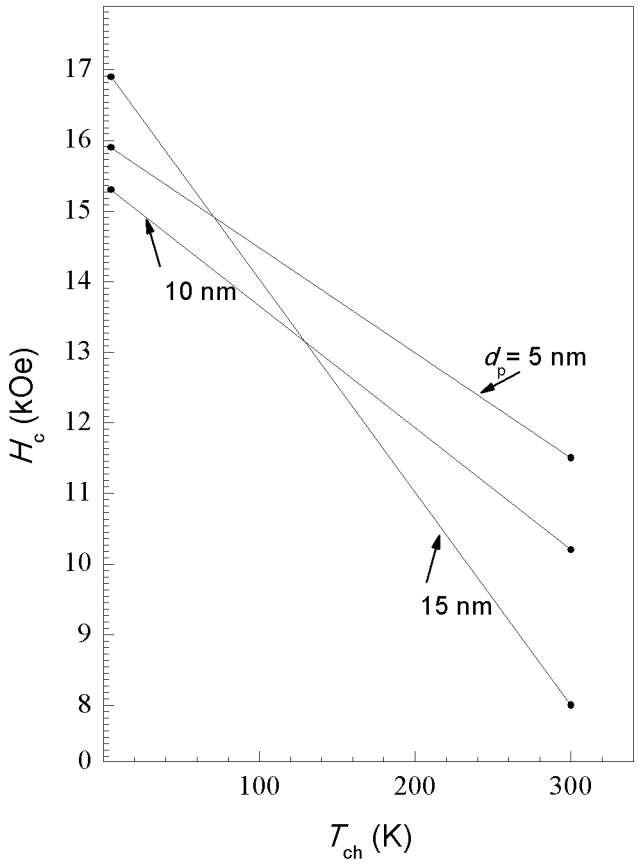

Figure 9.2.5.: Coercive field strenght H_c as function of the chamber temperature of the SQUID $T_{ch}$and particle size.

The saturation magnetisation M_s of FePt samples steeply decreases with increasing particle diameter from enormous 40 kOe at 300 K and 5 nm FePt over 8 kOe and 10 nm FePt till only 4 kOe and 15 nm FePt nanoparticles (see Fig. 9.2.6). The reason for this could be found in the increasing formation of polycrystalline FePt nanoparticles with increasing size due to random coagulation and sintering of primary particles. The appearance of crystal defects causes sections or crystallites possibly possessing the $L1_0$ order. However the orientations of magnetic moments inside these sections may differ

that much that the externally measured sum of magnetic moments for polycrystalline 15 or 10 nm FePt becomes lower than a 5 nm FePt sample consisting out of monocrystalline primary nanoparticles.

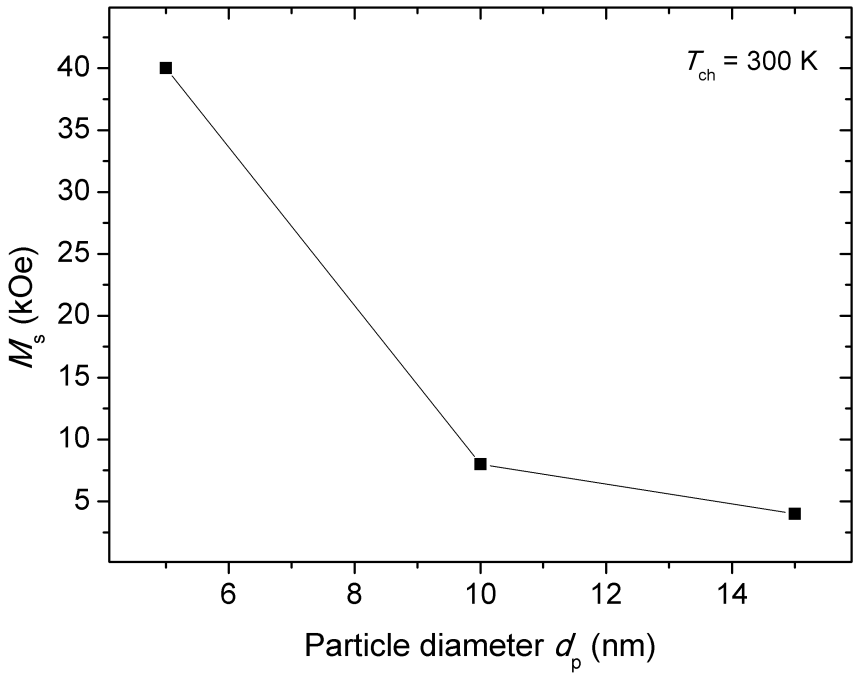

Figure 9.2.6.: Saturation magnetisation M_s at an ambient temperature of 300 K as function of particle diameter.

As mentioned in ch. 2.4 one is able to estimate the uniaxial anistropy constant k_U after knowing the blocking temperature, the saturation magnetization and the coercive field strength at a given ambient temperature T_{ch} (Cullity and Graham [2008]). As SQUID measurements were done at 5 K chamber temperature one could determine k_U via the following equation:

$$k_U = \frac{\mu_0 H_c(T_{ch} = 5\ \text{K}) \cdot M_S(T_{ch} = 5\ \text{K})}{2\left[1 - (T_{ch}/T_B)^{\frac{1}{2}}\right]} \tag{9.2.13}$$

The blocking temperature appears to have a minimum value of 300 K since FePt nanoparticles with particle diameter of 5, 10 and 15 nm particle diameter still show ferromagnetic behaviour as observed from the prior shown hysteresis loops. For the case that T_B

>> T_{ch} one could determine the minimum of k_{U} by

$$k_{\mathrm{U,min}} = \frac{\mu_0 H_{\mathrm{c}}(T_{\mathrm{ch}} = 5\ \mathrm{K}) \cdot M_{\mathrm{S}}(T_{\mathrm{ch}} = 5\ \mathrm{K})}{2} \tag{9.2.14}$$

Whereas a $k_{\mathrm{U,min}}$ of $6.087 \cdot 10^6$ J/m³ for FePt nanoparticles with a particle diameter of 10 nm and $3.025 \cdot 10^6$J/m^3 for 15 nm large nanoparticles are in the theoretically expected order of magnitude ($6.6 \cdot 10^6 - 10 \cdot 10^6$ J/m³, Weller et al. [2000]) , 5 nm large FePt nanoparticles with $2.72 \cdot 10^7$J/m³ seem to offer a giant magnetic uniaxial anisotropy.

Table 9.2.: Minimum of expected uniaxial magnetic anisotropy $k_{\mathrm{U,min}}$for different particle diameter of FePt nanoparticles

d_{p}(nm)	$k_{\mathrm{U,min}}$(J/m³)
5	$2.72 \cdot 10^7$
10	$6.087 \cdot 10^6$
15	$3.025 \cdot 10^6$

Summarizing, 5 nm FePt nanoparticles with respect to offering such a high uniaxial anisotropy constant, coercive field strength and saturation magnetisation could be preferably used for ultra high density storage applications. The elaborated synthesis route under use of ns pulsed laser ablation could be a serious option next to the sputtering technique or the wet chemical route.

9.3. Assembly of a magnetic film of FePt nanoparticles

Having achieved ferromagnetic and spherical FePt nanoparticles the next big issue of magnetic storage is the development of a method for achieving a high density monolayer. Fig. 9.3.1 shows a self assembly of 10 nm FePt nanoparticles (83 % in $\mathrm{L1_0}$ order at T_{s} = 1373 K) being deposited on a TEM grid by means of the custom built LPI. One can detect areas where matrices are formed with highest density due to the ferromagnetic properties of FePt nanoparticles attracting each other evenly. Self organization of magnetic nanoparticles is well known if wet chemical colloidal route is used as most

recently reported by van Raap et al. [2012], Theis-Bröhl et al. [2011] or Singamaneni et al. [2011]. There is already a technology in development which is called SOMA (Self Organized Magnetic Array). However homogenous particle film formation by means of low pressure impaction is difficult due to the small deposition spot. Even a multi hole nozzle will only deliver a slightly increased deposition area as pressure drop needs to be maintained with increasing number of smaller holes (smallest laser shot diameter 60 µm) and pumping capacity is limited. Further, more smaller holes will increase particle loss as well which is not economic and it is not guarenteed that nanoparticles are equally distributed upstream the multi hole nozzle due to the parabolic velocity profile of the gas. On the other hand, if only a single hole nozzle is used together with a positioning table underneath control of movement will become difficult to handle.

Instead, the custom built ESP showed the ability of forming large areas of homogeneous deposit. The fraction of charged particles could be increased by means of a UV charger which acts as a unipolar charger and therefore one could increase the deposition efficiency. Aside from particle formation out of the gas phase one could transfer particles into liquid media with adhesive which solidifies the magnetic layer. This could be achieved by using a bubbler with micron sized holes which is inserted in the liquid.

Another big issue arises after successful deposition. It is the design of a writing and reading head with GMR (Giant Magnetic Resistance) technology which can detect the position of a single FePt nanoparticle or one bit of information. The positioning of the heads becomes very difficult as well. Furthermore remagnetization of such a particle without influencing neighbouring particles is another difficult task.

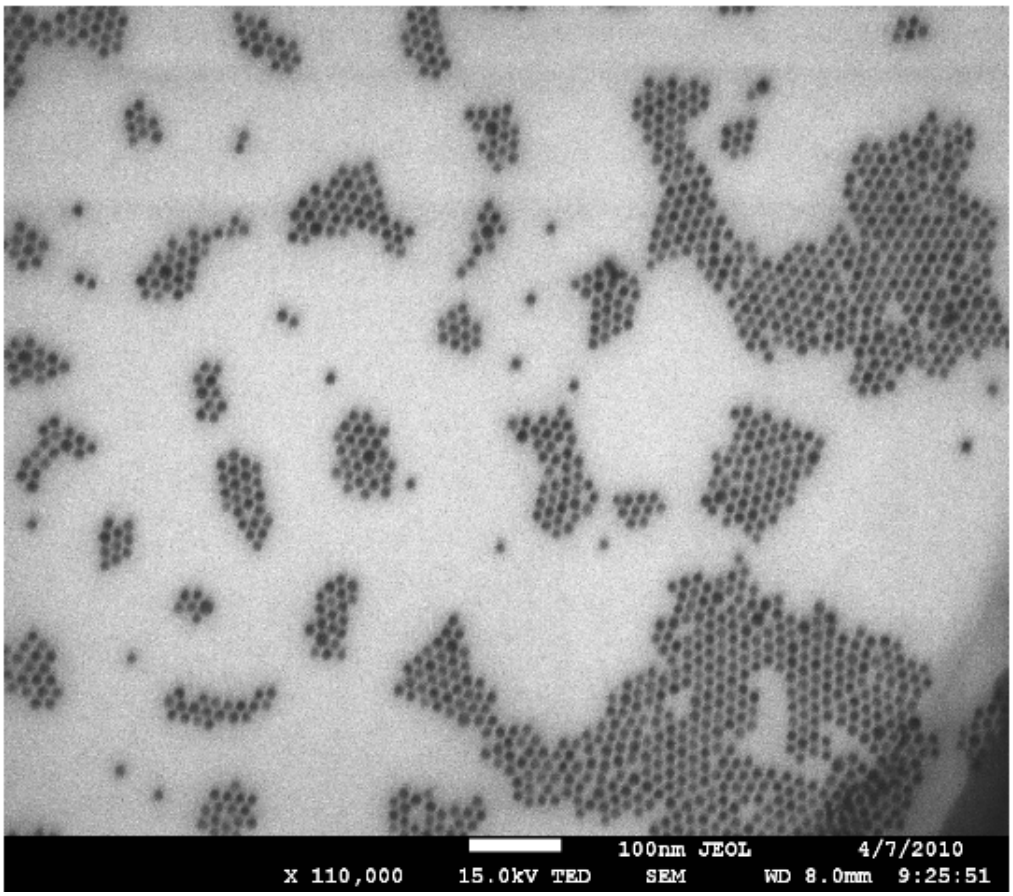

Figure 9.3.1.: Self assembly of 10 nm FePt nanoparticles being deposited by low pressure impaction

10. Summary and conclusion

The objective of this work was to create stoichiometrically preserved $L1_0$ ordered FePt magnetic nanoparticles offering a high magnetic anisotropy in order to enable future high density storage media. High magnetic anisotropy guarentees the preservation of digitized information at ambient temperatures realized by single domain nanoparticles of which each represents one bit of information in form of a distinct oriented magnetisation engrained by means of a highly sensitive write/reading head. Stability of magnetisation decreases with decreasing size of magnetic nanoparticles as one gets closer to the superparamagnetic limit thresholding a balance between magnetoanisotropic and thermal energy causing a objectional fluctuation of orientation of magnetic dipole moments. Therefore, different techniques for synthesis of nanoparticles out of the gas phase are presented and discussed with respect to feasibility (e.g. preservation of stoichiometry) and expected production efficiency. Pulsed Laser Ablation with 10 ns pulse duration was finally applied and available parameters such as wavelength, laser spot diameter and fluence were tested together with a FePt rod as target material. EDX measurements showed that a wavelength of 355 nm guarenteed the preservation of stoichiometry whereas 1064 nm and 532 nm lead to a non preferable shift towards iron rich samples. By using nitrogen as carrier gas one was able to improve the presence of $L1_0$ ordered nanoparticles due to volume diffusion and dissociation. Via a nozzle having a diameter of 1 mm nitrogen was introduced into a vacuum tight system necessary for avoiding oxidization of iron. SMPS measurements showed that increasing volume flow rates caused a shift of number size distribution towards smaller nanoparticles which is due to a larger velocity of the gas causing a shorter residence time of ablated material in the ablation cell and thus the formation of smaller agglomerates. A laser fluence

of 0.895 J/cm² was found suitable for generating a sufficient amount of mainly singly charged FePt nanoparticles in the sub 20 nm range. At this fluence the laser ablation turned out to be an efficient bipolar charging method as well. It was further of interest to utilize a fractionating method which allowed an investigation of monodispersed FePt nanoparticles in order to check the magnetic properties as function of particle size. Together with the charging capability of laser ablation the most reasonable fractionating method was the electrical differential mobility analysis executed with a custom built radial DMA. As shape of monodispersed FePt nanoparticles should be as compact as possible and condensed matter more probably spawns non compacted agglomerates one had to find a method of compaction being finally realized by means of onflight sintering which was tested by passing the aerosol through tube furnaces with different dimensions of sintering tubes. It turned out that compact FePt particles in the sub 20 nm range could be found if sintering temperatures well above 1273 K were maintained. Next to compaction annealing of FePt also caused an increased fraction of $L1_0$ order with increasing temperature at sintering times around 1 s which was found by evaluation of HRTEM diffraction pattern and Rietveld refinement. A maximum order of 85 % could be achieved with 15 nm FePt being annealed at 1473 K and 82% with 10 nm FePt being annealed at 1373 K.

For relating magnetic measurements to prepared FePt samples a deposition technique was elaborated which offers the possibility to create a defined amount and thus total volume of sampled nanoparticles. For achieving this a custom built low-pressure impactor was used together with a condensation particle counter. Inside the low pressure impactor adhesive tape strips were fixed in a magazine. After deposition one obtained defined layers of 5, 10 or 15 nm FePt nanoparticles. The prepared strips were then plugged on plastic straws offering the possiblity to execute SQUID measurements with low level of magnetic interference. It could be found that especially 5 nm FePt nanoparticles showed excellent ferromagnetic characteristics with respect to a magnetic coercive field of 1.15 T and saturation magnetisation of 40 kOe at room temperature and as they are the smallest a maximum achievable storage density becomes possible as well. Additionally, high uniaxial anisotropy constants (larger than $2.72 \cdot 10^7$J/m³ for 5 nm FePt; $6.087 \cdot 10^6$ J/m³ for 10 nm FePt; $3.025 \cdot 10^6$ J/m³ for 15 nm FePt) could be found experi-

mentally possibly offering a stable state of magnetisation if the blocking temperature is much higher than the ambient temperature . These values are the first reported ones.

Symbols

α	heat transfer coefficient [W/(m² K)]
β	Pearson composition parameter [-]
β_f	dimensionless flow parameter [-]
Δa	width of particle size distribution [m]
δ	dimensionless flow parameter [-]
η_g	viscosity of gas [kg/(m s)]
$\eta_{c,exp}$	experimentally determined charged fraction of nanoparticles [-]
η_{CPC}	counting efficiency of CPC [-]
η_{LPI}	deposition efficiency of LPI [-]
η_{PV}	Pseudo-Voigt composition parameter [-]
γ	surface tension [N/m]
λ	laser wavelength [m]
λ_g	mean free path of gas molecules [m]

Λ_{th} thermophoretic loss [-]

μ_0 permeability constant [V s / (A m)]

μ_{a} atomic magnetic moment [Am²]

μ_g dynamic gas viscosity [-]

μ_m total magnetic moment of a sample [Am²]

∇T temperature gradient [K]

Ω atomic volume [m³]

ω angular frequency of rotating cylinder in CPMA [Hz]

Ω_d diffusing transfer function of DMA [-]

Ω_{nd} non-diffusing relative transfer function of DMA [-]

$\overline{T}$ mean temperature in furnace tube [K]

Φ thermionic workfunction [J]

ϕ laser fluence profile [J/m²]

ϕ_0 maximum laser fluence [J/m²]

ϕ_{th} ablation threshold fluence [J/m²]

σ arithmetic standard deviation of particle diameter [m]

σ_g geometric standard deviation of mean geometric particle diameter [m]

σ_i standard deviation at location i [-]

τ_r relaxation time of particle motion [s]

τ_{coa} coalescence time [s]

τ_{col} particle collision time [s]

τ_{rel} relaxation time for thermal decay of magnetization [s]

θ_k calculated position of reflex k [-]

$\triangle T$ temperature gradient in tube furnace [K/m]

$\widetilde{Z}_p$ dimensionless mobility set with DMA [-]

a lattice constant in [100] direction [m]

a_0 mean particle size in nucleation process [m]

A_o area of orifice outlet [m²]

A_R Richardson constant [A/(m²K²)]

b distance between electrodes in radial DMA [m]

c lattice constant in [001]- direction [m]

C_c Cunningham slip correction [-]

c_v packaging density [-]

d^* critical nucleus size [m]

d_{arit} arithmetic mean diameter of nanoparticles [m]

d_c characteristic dimension of obstacle [m]

d_g mean geometric particle diameter [m]

d_L laser spot diameter [m]

d_m equivalent mobility diameter of particle [m]

d_p equivalent particle diameter [m]

d_s deposition spot diameter [m]

d_{E} electrode diameter of ESP [m]

d_{N} nozzle diameter of ESP [m]

d_{mol} diameter of gas molecules [m]

$d_{p,l}$ lower particle diameter [nm]

$d_{p,u}$ upper particle diameter [nm]

d_{plate} outer diameter of orifice plate at ESP [mm]

dz length element in z- direction of heated tube [m]

E free energy [J]

e elementary charge [As]

E_P laser pulse energy [J]

E_{ESP} electrical field strength in electrostatic precipitator [V/m]

E_{th} thermal energy [J]

f friction coefficient [kg/s]

f_0 experimental frequency [Hz]

f_B Boltzmann charging probability [-]

F_D drag force [kg m/s²]

F_E electrostatic force [kg m/s²]

F_i external forces [kg m/s²]

F_k structure factor [-]

F_L laser fluence [J/m²]

f_L laser pulse repetition rate [Hz]

f_{LN} log normal density function [-]

f_{ch} charging probability of radioactive source according to Wiedensohler [

G profile function [-]

H_C Coercive field strength [A/m]

H_k full width half maximum of reflex k [-]

H_k^{Gau} Gaussian component of FWHM of reflex k [-]

$H_k^{Lorentz}$ Lorentzian component of FWHM of reflex k [-]

H_S switching magnetic coercitivity [A/m]

i step of measurement [-]

J nucleation rate [-]

j emitted electron current density [A/m²]

k Bragg reflex [-]

k_B Boltzmann constant [J/K]

k_u uniaxial magnetic anisotropy constant [m³]

K_{th} thermophoretic coefficient [1/m]

$k_{U,min}$ minimum of uniaxial anisotropy constant [J/m³]

Kn Knudsen number[-]

L Length of classification zone in cDMA [m]

L_k Lorentz polarisation factor [-]

m mass of a nanoparticle [kg]

m_k spatial frequency [1/m]

M_m magnetisation [A/m]

M_S saturized magnetisation [K]

m_T total mass of a SQUID sample [g]

m_{FePt} mass of nanoparticles of a sampled particle diameter [kg]

N number concentration measured with CPC [1/cm³]

n number of molecules [-]

N_A particle number concentration in aerosol [m^{-3}]

n_c number of classes of particle diameter [-]

n_d number of deposited particles in LPI [-]

n_e number of emitted electrons [-]

n_i number of nanoparticles belonging to ith class of particle diameter [m]

N_O number of observations for Rietfeld refinement [-]

n_p number of observed nanoparticles [-]

n_u uncharged fraction of nanoparticles passing the ESP [-]

n_{1ML} number of particles for one monolayer [-]

n_{a} number of atoms [-]

N_{T} total number of nanoparticles for a SQUID sample [-]

n_{dp} number of different particle diameter [-]

N_i sampled number of nanoparticles with size class i [-]

Nu Nusselt number [-]

P total gas pressure [kg/(ms^2]

p number of elementary charges [-]

P_{f} number of free parameters for Rietfeld refinement [-]

P_{L} laser power [W]

Q_A aerosol flow [m^3/s]

Q_c entering sheath flow in radial DMA [m³/s]

Q_F quality of fit by Rietfeld refinement [-]

Q_g volume flow rate of a gas [m³/s]

Q_m the exiting sheath flow rate of a DMA [l/min]

Q_s sample flow in radial DMA [m³/s]

Q_{C} sample flow entering CPC [m³/s]

Q_{in} introduced carrier gas flow [m³/s]

Q_{I} gas flow entering low pressure impactor [m³/s]

Q_{S} sheath gas flow at DMA [m³/s]

r radius from pulse centre of laser [m]

R_1 radius of central electrode [m]

R_2 inner radius of outer electrode in cDMA [m]

r_i inner radius of classification zone in CPMA [m]

r_o outer radius of classification zone in CPMA [m]

r_{p} radial position of particle in CPMA [m]

R_E quality factor of Rietveld refinement expected Bragg R value [-]

R_{in} inner radius of entrance slot of radial DMA [m]

R_{out} outer radius of entrance slot of radial DMA [m]

R_{wP} weighted quality factor of Rietveld refinement R-Profile value [-]

S supersaturation [-]

s scaling factor for Rietveld refinement [-]

Stk Stokes number [-]

T temperature [K]

t time [s]

T_B blocking temperature [K]

T_c centerline temperature of heated tube [K]

t_P laser pulse duration [s]

T_s sintering temperature [K]

T_w inner wall temperature of heated tube [K]

t_{res} residence time in heated region of tube furnace [s]

u particle volume [m³]

u_f gas velocity [m/s]

u_o mean gas velocity inside an orifice [m/s]

u_p particle velocity [m/s]

U_{ESP} electrode voltage of ESP [V]

U_{CPMA} potential difference between concentric cylinders of CPMA [V]

U_{DMA} applied electrode voltage in DMA [V]

v particle volume [m³]

V_g grain volume [m³]

V_m molar volume [cm³]

V_p particle volume [m³]

v_p velocity of particle relative to gas flow [m/s]

v_{1ML} volume of one monolayer thick deposit [m³]

V_{SP} volume of a spherical nanoparticle [m³]

V_{Pcrit} minimum volume of particle for thermally stable magnetisation [m³]

v_{th} thermophoretic velocity of a nanoparticle [m/s]

V_{uc} volume of a unit cell [m³]

w_0 radius for laser fluence dropping to 1/e² of maximum [m]

w_i weight factor for Rietveld refinement at location i [-]

w_{cz} width of classification zone in pDMA [m]

y_{ib} background of intensity profile [-]

y_{ic} calculated intensity at location i [-]

y_{io} observed intensity at location i [-]

z distance between nozzle plate and central electrode of ESP [m]

Z_p electrical mobility of particle[As²/kg]

Z^*_{cDMA} centroid mobility of classified nanoparticles in cDMA [As²/kg]

Z^*_{pDMA} centroid mobility of classified particles in pDMA [As²/kg]

Z^*_{rDMA} centroid mobility of classified particles in radial DMA [As²/kg]

Abbreviations

CPC	Condensation Particle Counter
CVS	Chemical Vapour Synthesis
EDX	Energy Dispersive X-ray spectroscopy
EELS	Electron Energy Loss Spectroscopy
ESP	Electrostatic Precipitator
fcc	face centered cubic
fct	face centered tetragonal
FWHM	Full Width at Half Maximum
GMR	Giant Magneto Resistance
HRTEM	High Resolution Transmission Electron Microscopy
HV-RDMA	High Vacuum-Radial Differential Mobility Analyzer
LA-PLA	Liquid Assisted Pulsed Laser Ablation
LPI	Low Pressure Impactor
ML	Monolayer
NAPLD	Nanoparticle Assisted Pulsed Laser Deposition
Nd:YAG	Neodymium donated Yttrium-Aluminium-Granat-Laser
pDMA	parallel plate Differential Mobility Analyzer
PLD	Pulsed Laser Deposition
PVD	Physical Vapour Deposition
PVS	Physical Vapour Synthesis
SAED	Selected Area Electron Diffraction
SOMA	Self-Organized Magnetic Array
SQUID	Superconducting Quantum Interference Device

STEM	Scanning Transmission Electron Microscopy
TAPLD	Thermally Assisted Pulsed Laser Deposition

List of Figures

List of Tables

Bibliography

N.R. Agarwal, F. Neri, S. Trusso, A. Lucotti, and P.M. Ossi. Au nanoparticle arrays produced by Pulsed Laser Deposition for Surface Enhanced Raman Spectroscopy. *Applied Surface Science*, 258(23):9148–9152, 2012.

S.A. Al-Mamun, R. Nakajima, and T. Ishigaki. Tuning the size of aluminum oxide nanoparticles synthesized by laser ablation in water using physical and chemical approaches. *Journal of Colloid and Interface Science*, 392(1):172–182, 2013.

A.P. Alivisatos. Semiconductor clusters, nanocrystals, and quantum dots. *Science*, 271 (5251):933–937, 1996.

A.P. Alivisatos. Nanocrystals: Building blocks for modern materials design. *Endeavour*, 21(2):56–60, 1997.

D. Alloyeau, C. Ricolleau, C. Mottet, T. Oikawa, C. Langlois, Y. Le Bouar, N. Braidy, and A. Loiseau. Size and shape effects on the order-disorder phase transition in CoPt nanoparticles. *Nature Materials*, 8(12):940–946, 2009.

S. Amoruso, G. Ausanio, R. Bruzzese, L. Gragnaniello, L. Lanotte, M. Vitiello, and X. Wang. Characterization of laser ablation of solid targets with near-infrared laser pulses of 100 fs and 1 ps duration. *Applied Surface Science*, 252(13 SPEC. ISS):4863–4870, 2006.

S. Anders, S. Sun, C.B. Murray, C.T. Rettner, M.E. Best, T. Thomson, M. Albrecht, J.U. Thiele, E.E. Fullerton, and B.D. Terris. Lithography and self-assembly for nanometer scale magnetism. *Microelectronic Engineering*, 61-62:569–575, 2002.

P. Asanithi, S. Chaiyakun, and P. Limsuwan. Growth of silver nanoparticles by dc magnetron sputtering. *Journal of Nanomaterials*, 2012:art.no. 963609, 2012.

G. Ausanio, V. Iannotti, S. Amoruso, X. Wang, C. Aruta, M. Arzeo, R. Fittipaldi, A. Vecchione, R. Bruzzese, and L. Lanotte. Effects of substrate temperature on nanoparticle-assembled Fe films produced by ultrafast pulsed laser deposition. *Applied Surface Science*, 258(23):9337–9341, 2012.

M.D. Barankin, Y. Creyghton, and A. Schmidt-Ott. Synthesis of nanoparticles in an atmospheric pressure glow discharge. *Journal of Nanoparticle Research*, 8(3-4):511–517, 2006.

K. Barmak. Calorimetric studies of the A1 to L10 transformation in binary FePt thin films with compositions in the range of 47.5- 54.4 at% Fe. *Journal of Applied Physics*, 99(024902), 2005.

D. Bäuerle. *Laser processing and chemistry*. Springer, New York, 1 edition, 1996.

D. Beena, R. Vinodkumar, I. Navas, V. Ganesan, A. Yamuna, and V.P. Mahadevan Pillai. Transparent conducting indium molybdenum oxide films by pulsed laser ablation. *Journal of Alloys and Compounds*, 539:63–68, 2012.

G. Biskos, V. Vons, C.U Yurteri, and A. Schmidt-Ott. Generation and Sizing of Particles for Aerosol-Based Nanotechnology. *Kona Powder and Particle Journal*, 26:13–35, 2008.

A. Bonis, R. Teghil, A. Santagata, A. Galasso, and J.V. Rau. Thin films deposited by femtosecond pulsed laser ablation of tungsten carbide. *Applied Surface Science*, 258 (23):9198–9201, 2012.

J. Bonse, J.M. Wrobel, J. Krüger, and W. Kautek. Ultrashort-pulse laser ablation of indium phosphide in air. *Applied Physics A: Materials Science and Processing*, 72(1): 89–94, 2001.

P. Buffat and J.-P. Borel. Size effect on the melting temperature of gold particles. *Physical Review A*, 13(6):2287–2298, 1976.

H.C Burger and P.H van Cittert. Die Herstellung von Wismut-Antimon-Vakuumthermoelementen durch Verdampfung. *Zeitschrift für Physik*, 66(3-4):210–217, 1930.

J.H. Byeon and J.T. Roberts. Silver deposition on a polymer substrate catalyzed by singly charged monodisperse copper nanoparticles. *ACS Applied Materials and Interfaces*, 4 (5):2515–2520, 2012.

R.P. Camata, H.A. Atwater, K.J. Vahala, and R.C. Flagan. Size classification of silicon nanocrystals. *Applied Physics Letters*, 68(22):3162–3164, 1996.

Cambustion. Centrifugal Particle Mass analyzer. *Brochure*, 2012.

E. Camps, L. Escobar-Alarcón, I. Camps, S. Muhl, and M. Flores. Tribological characterization of TiCN coatings deposited by two crossed laser ablation plasma beams. *Applied Physics A: Materials Science and Processing*, 110(4):957–961, 2012.

D. Canteli, S. Fernandez, C. Molpeceres, I. Torres, and J.J. Gandía. Nanosecond laser ablation processes in aluminum-doped zinc-oxide for photovoltaic devices. *Applied Surface Science*, 258(23):9447–9451, 2012.

E. Cappelli, D.M. Trucchi, S. Orlando, A. Bellucci, A. Mezzi, and S. Kaciulis. Influence of process conditions on chemical composition and electronic properties of AlN thin films prepared by ArF reactive pulsed laser deposition. *Physica Status Solidi (C) Current Topics in Solid State Physics*, 9(3-4):1053–1056, 2012.

X.-S. Che, Z.-T. Liu, Y.-P. Li, N. Wang, and Z. Xu. Effects of methane flow rate on the optical properties and chemical bonding of germanium carbon films deposited by reactive sputtering. *Vacuum*, 90(1):75–79, 2013.

D.-R. Chen, D.Y.H. Pui, D. Hummes, H. Fissan, F.R. Quant, and G.J. Sem. Design and evaluation of a nanometer aerosol differential mobility analyzer (Nano-DMA). *Journal of Aerosol Science*, 29(5-6):497–509, 1998.

J.S. Chen, B.C. Lim, and J.P. Wang. Crystallographic orientation control in L10 FePt films on CrRu underlayer. *Digests of the Intermag Conference*, 2003.

M. Chen, J.P. Liu, and S. Sun. One-step synthesis of FePt nanoparticles with tunable size. *Journal of the American Chemical Society*, 126(27):8394–8395, 2004.

M. Chen, J. Kim, J.P. Liu, H. Fan, and S. Sun. Synthesis of FePt nanocubes and their oriented self-assembly. *Journal of the American Chemical Society*, 128(22):7132–7133, 2006.

H. Cho, S. Kim, and H. Ki. Pulsed laser deposition of functionally gradient diamond-like carbon (DLC) films using a 355 nm picosecond laser. *Acta Materialia*, 60(18): 6237–6246, 2012.

B.D. Cullity and C.D. Graham. *Introduction to magnetic materials*. Wiley, New York, 2008.

T.L. da Silva and L.C. Varanda. Perpendicularly self-oriented and shape-controlled L10-FePt nanorods directly synthesized by a temperature-modulated process. *Nano Research*, 4(7):666–674, 2011.

Z.R. Dai, S. Sun, and Z.L. Wang. Phase Transformation, Coalescence, and Twinning of Monodisperse FePt Nanocrystals. *Nano Letters*, 1(8):443–447, 2001.

R. Das, B. Das, R. Shukla, P. Deb, T. Prabaharan, and A. Shyam. Experimental study of exploding wire method for production of metal nanoparticles. *Instruments and Experimental Techniques*, 55(1):131–133, 2012.

Y.F. Ding. Nucleation site density study of the L10 phase transformation in FePt nanoparticles. *Journal of Applied Physics*, 99(8):1–3, 2006.

Y.F. Ding, J.S. Chen, and E. Liu. Modulation of preferred orientation and easy axis of magnetic anisotropy in L10 FePt films with Cu buffer layers. *Surface and Coatings Technology*, 198(1-3 SPEC. ISS):262–265, 2005a.

Y.F. Ding, J.S. Chen, and E. Liu. Controlling the crystallographic orientation and easy axis of magnetic anisotropy in L10 FePt films with Cu additive. *Surface and Coatings Technology*, 198(1-3 SPEC. ISS):270–273, 2005b.

J. Dixkens and H. Fissan. Development of an electrostatic precipitator for off-line particle analysis. *Aerosol Science and Technology*, 30(5):438–453, 1999.

O. Dmitrieva, M. Acet, G. Dumpich, J. Kästner, C. Antoniak, M. Farle, and K. Fauth. Enhancement of L10 phase formation in FePt nanoparticles by nitrogenization. *Journal of Physics D: Applied Physics*, 39(22):4741–4745, 2006.

A.S. Edelstein and R.C. Cammarata. *Nanomaterials: Synthesis, Properties and Applications*. London, 1997.

K. Ehara, C. Hagwood, and K.J. Coakley. Novel method to classify aerosol particles according to their mass-to-charge ratio - Aerosol particle mass analyser. *Journal of Aerosol Science*, 27(2):217–234, 1996.

Y.H. Fang, P.C. Kuo, S.C. Chen, S.L. Hsu, and G.P. Lin. Alternate monatomic layer deposited L10 FePt (001) with high coercivity and small grain size. *Thin Solid Films*, 517(17):5185–5188, 2009.

M. Farahmandjou. Synthesis and structural study of L10- FePt nanoparticles. *Turkish Journal of Engineering and Environmental Sciences*, 34(4):265–270, 2010.

M. Farahmandjou. The effect of 1, 2- hexadecadeniol and LiBEt3H superhydride on the size of FePt nanoparticles. *AIP Conference Proceedings*, 1415:193, 2011.

M. Farahmandjou. Effect of oleic acid and oleylamine surfactants on the size of FePt Nanoparticles. *Journal of Superconductivity and Novel Magnetism*, 25(6):2075–2079, 2012.

M. Farahmandjou and S.A. Sebt. The effect of NaCl prepared by ultra-sonic vibration on the sintering of annealed FePt nanoparticles. *Chinese Journal of Physics*, 47(4): 540–546, 2009.

M. Farahmandjou, S.A. Sebt, S.S. Parhizgar, P. Aberomand, and M. Akhavan. The effect of NaCl prepared by ultra-sonic vibration on Sintering of annealed FePt nanoparticles. *Journal of Physics: Conference Series*, 153:art.no. 012050, 2009.

E. Fazio, F. Neri, R. Ruggeri, G. Sabatino, S. Trusso, and G. Mannino. Structural properties of pulsed laser deposited SnOx thin films. *Applied Surface Science*, 257(7): 2520–2525, 2011.

J. Fernandez de la Mora, S.V. Hering, N. Rao, and P.H. McMurry. Hypersonic impaction of ultrafine particles. *Journal of Aerosol Science*, 21(2):169–187, 1990.

H. Fissan, D. Hummes, F. Stratmann, P. Büscher, S. Neumann, D.Y.H. Pui, and D. Chen. Experimental comparison of four differential mobility analyzers for nanometer aerosol measurements. *Aerosol Science and Technology*, 24(1):1–13, 1996.

R.C. Flagan and M.M. Lunden. Particle structure control in nanoparticle synthesis from the vapor phase. *Materials Science and Engineering A*, 204(1-2):113–124, 1995.

S.K. Friedlander. Smoke, dust and haze. Fundamentals of aerosol behaviour. *Oxford University Press*, 1977.

B. Ghosh, S. Hussain, D. Ghosh, R. Bhar, and A.K. Pal. Studies on CdTe films deposited by pulsed laser deposition technique. *Physica B: Condensed Matter*, 407(21):4214–4220, 2012.

P. Gibot, E. Tronc, C. Chanéac, J.P. Jolivet, D. Fiorani, and A.M. Testa. (Co,Fe)Pt nanoparticles by aqueous route; Self-assembling, thermal and magnetic properties. *Journal of Magnetism and Magnetic Materials*, 290-291 PART 1:555–558, 2005.

E.B. Gordon, A.V. Karabulin, V.I. Matyushenko, V.D. Sizov, and I.I. Khodos. The electrical conductivity of bundles of superconducting nanowires produced by laser ablation of metals in superfluid helium. *Applied Physics Letters*, 101:art. no. 052605, 2012.

C.G. Granqvist and R.A. Buhrman. Ultrafine metal particles. *Journal of Applied Physics*, 47(5):2200–2219, 1976.

S. Guo and S. Sun. FePt nanoparticles assembled on graphene as enhanced catalyst for oxygen reduction reaction. *Journal of the American Chemical Society*, 134(5):2492–2495, 2012.

T. Hachisu, A. Sugiyama, and T. Osaka. Development on self-assembly technique for arrangement of chemically synthesized FePt nanoparticles. *ECS Transactions*, 33 (34):107–113, 2011.

J. Harra, J. Mäkitalo, R. Siikanen, M. Virkki, G. Genty, T. Kobayashi, M. Kauranen, and J.M. Mäkelä. Size-controlled aerosol synthesis of silver nanoparticles for plasmonic materials. *Journal of Nanoparticle Research*, 14(6):1–10, 2012.

J.W. Harrell, S. Wang, D.E. Nikles, and M. Chen. Thermal effects in self-assembled FePt nanoparticles with partial chemical ordering. *Applied Physics Letters*, 79(26): 4393–4395, 2001.

M. Heim, G. Kasper, G.P. Reischl, and C. Gerhart. Performance of a new commercial electrical mobility spectrometer. *Aerosol Science and Technology*, 38(SUPPL. 2):3–14, 2004.

W.C. Hinds. *Aerosol technology: properties, behaviour, and measurement of airborne particles*. New York, 1982.

M. Hirasawa, T. Orii, and T. Seto. Size-dependent crystallization of Si nanoparticles. *Applied Physics Letters*, 88(9):1–4, 2006.

L.E.M. Howard, H.L. Nguyen, S.R. Giblin, B.K. Tanner, I. Terry, A.K. Hughes, and J.S.O. Evans. A synthetic route to size-controlled fcc and fct FePt nanoparticles. *Journal of the American Chemical Society*, 127(29):10140–10141, 2005.

Y. Huang, J. Wan, Y. Zhang, and G. Hadjipanayis. Fabrication of FePt/M (M = C, Ag, Si) nanoparticulate thin films with perpendicular anisotropy. *International Journal of Product Development*, 5(3-4):259–267, 2008.

Y.H. Huang, J. Wan, Y. Zhang, G.C. Hadjipanayis, and D. Weller. FePt nanoparticles with tailored microstructure. *Digests of the Intermag Conference*, (3):FD05, 2003.

Y.H. Huang, J. Wan, Y. Zhang, H.L. Wang, G.C. Hadjipanayis, D. Niarchos, and D. Weller. Investigation of particle formation and superstructure development in FePt nanoparticles and their effect on magnetic properties. *Journal of Magnetism and Magnetic Materials*, 294(2):232–238, 2005.

D.M. Hull and A. Stewart. Laser beam profiles - Principles and definitions. *Lasers & applications*, 4(10):75–80, 1985.

D. Hummes. *Entwicklung eines differentiellen Mobilitäts-Analysators zur Bereitstellung von monodispersen Partikeln im Nanometergrößenbereich*. Pro-Universitate-Verlag, Sinzheim, 1997.

D. Hummes, S. Neumann, F. Schmidt, M. DrÃ¶tboom, H. Fissan, K. Deppert, T. Junno, J.-O. Malm, and L. Samuelson. Determination of the size distribution of nanometer-sized particles. *Journal of Aerosol Science*, 27(SUPPL.1):S163–S164, 1996.

K.M. Hyie and I.I. Yaacob. Annealing behavior of FePt ferromagnetic nanoparticles prepared in water-in-oil microemulsions. *AIP Conference Proceedings*, 1138, 2009.

V. Ievlev, M. Sumets, and A. Kostyuchenko. Conduction mechanisms in Si-LiNbO3 heterostructures grown by ion-beam sputtering method. *Journal of Materials Science*, 48 (4):1562–1570, 2013.

R. Intartaglia, K. Bagga, A. Genovese, A. Athanassiou, R. Cingolani, A. Diaspro, and F. Brandi. Influence of organic solvent on optical and structural properties of ultra-small silicon dots synthesized by UV laser ablation in liquid. *Physical Chemistry Chemical Physics*, 14(44):15406–15411, 2012.

J. D. Jackson. *Classical electrodynamics*. Wiley, New York, 3 edition, 1999. ISBN 9780471309321.

JCPDS. International Center for Diffraction Data. pages 26–1139, 1995.

Z. Jia, S. Kang, D.E. Nikles, and J.W. Harrell. Synthesis of FePtAu nanoparticles in high-boiling-point solvents. *IEEE Transactions on Magnetics*, 41(10):3385–3387, 2005.

T. Junno, M.H. Magnusson, S.-B. Carlsson, K. Deppert, J.-O. Malm, L. Montelius, and L. Samuelson. Single-electron devices via controlled assembly of designed nanoparticles. *Microelectronic Engineering*, 47(1):179–183, 1999.

S. Kala, B.R. Mehta, F.E. Kruis, and V.N. Singh. Synthesis and oxidation stability of monosized and monocrystalline Pr nanoparticles. *Journal of Materials Research*, 24 (7):2276–2285, 2009.

S. Kala, M. Rouenhoff, R. Theissmann, and F.E. Kruis. Synthesis and film formation of monodisperse nanoparticles and nanoparticle pairs. *NanoScience and Technology*, 79:99–119, 2012.

E. Kang, H. Jung, J.-G. Park, S. Kwon, J. Shim, H. Sai, U. Wiesner, J.K. Kim, and J. Lee. Block copolymer directed one-pot simple synthesis of L10-phase FePt nanoparticles inside ordered mesoporous aluminosilicate/carbon composites. *ACS Nano*, 5(2):1018–1025, 2011.

L.S. Karlsson, K. Deppert, and J.-O. Malm. Size determination of au aerosol nanoparticles by off-line tem/stem observations. *Journal of Nanoparticle Research*, 8(6):971–980, 2006.

M.N.A. Karlsson, K. Deppert, L.S. Karlsson, M.H. Magnusson, J.-O. Malm, and N.S. Srinivasan. Compaction of agglomerates of aerosol nanoparticles: A compilation of experimental data. *Journal of Nanoparticle Research*, 7(1):43–49, 2005a.

M.N.A. Karlsson, K. Deppert, B.A. Wacaser, L.S. Karlsson, and J.-O. Malm. Size-controlled nanoparticles by thermal cracking of iron pentacarbonyl. *Applied Physics A: Materials Science and Processing*, 80(7):1579–1583, 2005b.

S. Kawabata, N. Ishikawa, M. Mitsui, and A. Nakajima. Fabrication and characterization of a granular film consisting of size-selected silver nanoparticles: Application to a SERS substrate. *European Physical Journal D*, 43(1-3):155–158, 2007.

K. Kawai, S. Honda, R. Sugiki, M. Komatsu, and K. Kawabata. High coercive FePt alloys prepared by a new sputtering method. *Journal of Magnetism and Magnetic Materials*, 287(SPEC. ISS):214–218, 2005.

M. Kawakami, A.B Hartanto, Y. Nakata, and T. Okada. Synthesis of ZnO nanorods by nanoparticle assisted pulsed-laser deposition. *Japanese Journal of Applied Physics, Part 2: Letters*, 42(1 A/B):L33–L35, 2003.

Y. Kawakami, T. Seto, and E. Ozawa. Synthesis and characteristics of tungsten ultrafine particles by Nd:YAG laser irradiation. *Nippon Kinzoku Gakkaishi / Journal of the Japan Institute of Metals*, 63(9):1101–1104, 1999.

M.K. Kennedy, F.E. Kruis, H. Fissan, B.R. Mehta, S. Stappert, and G. Dumpich. Tailored nanoparticle films from monosized tin oxide nanocrystals: Particle synthesis, film formation, and size-dependent gas-sensing properties. *Journal of Applied Physics*, 93 (1):551–560, 2003.

M. Khanuja, S. Kala, B.R. Mehta, and F.E Kruis. Concentration-specific hydrogen sensing behavior in monosized Pd nanoparticle layers. *Nanotechnology*, 20(1):1–7, 2009.

M.A. Khaskheli, P. Wu, R. Chand, X. Li, H. Wang, S. Zhang, S. Chen, and Y. Pei. Structural and dielectric properties of Ti and Er co-doped HfO2 gate dielectrics grown by RF sputtering. *Applied Surface Science*, 266:355–359, 2013.

J. Kim, C. Rong, J. Ping Liu, and S. Sun. Dispersible ferromagnetic FePt nanoparticles. *Advanced Materials*, 21(8):906–909, 2009.

Y.-T Kim, J. Park, and J. Choi. Sputter-deposited ZnO thin films consisting of nanonetworks for binder-free dye-sensitized solar cells. *Current Applied Physics*, 13(2): 381–385, 2013.

J. Klanwan, T. Seto, T. Furukawa, Y. Otani, T. Charinpanitkul, M. Kohno, and M. Hirasawa. Generation and size classification of single-walled carbon nanotube aerosol using atmospheric pressure pulsed laser ablation (AP-PLA). *Journal of Nanoparticle Research*, 12(8):2747–2755, 2010.

T.J. Klemmer, N. Shukla, C. Liu, X.W. Wu, E.B. Svedberg, O. Mryasov, R.W. Chantrell, and D. Weller. Structural studies of L10 FePt nanoparticles. *Applied Physics Letters*, 81(12):2220–2222, 2002.

E.O. Knutson and K.T. Whitby. Aerosol classification by electric mobility: apparatus, theory, and applications. *Journal of Aerosol Science*, 6(6):443–451, 1975.

F. Kokai, S. Inoue, H. Hidaka, K. Uchiyama, Y. Takahashi, and A. Koshio. Catalyst-free growth of amorphous silicon nanowires by laser ablation. *Applied Physics A: Materials Science and Processing*, pages 1–7, 2012.

A. Koshio, M. Shiraishi, Y. Kobayashi, M. Ishihara, Y. Koga, S. Bandow, S. Iijima, and F. Kokai. Modification of carbon nanotubes by laser ablation of copper. *Chemical Physics Letters*, 396(4-6):410–414, 2004.

F.E. Kruis, K. Nielsch, H. Fissan, B. Rellinghaus, and E.F. Wassermann. Preparation of size-classified pbs nanoparticles in the gas phase. *Applied Physics Letters*, 73(4): 547–549, 1998.

P. Kulkarni and J. Wang. New fast integrated mobility spectrometer for real-time measurement of aerosol size distribution-I: Concept and theory. *Journal of Aerosol Science*, 37(10):1303–1325, 2006.

S. Kuroda, S. Kaihara, Y. Fujii, T. Kinoshita, and M. Adachi. Modeling of particle generation in laser ablation plasma. *Journal of Aerosol Science*, 50:38–56, 2012.

H. Landolt and R. Börnstein. *Numerical data and functional relationships in science and technology: new series IV*, volume 5e. Springer, Berlin, 1992.

H.-S. Lee and J.-Y. Kim. Lattice expansion by adding oxygen to control crystallographic orientations in chemically ordered L10 FePt films. *IEEE Transactions on Magnetics*, 43(7):3149–3152, 2007.

A.H. Li, H.K. Liu, M. Ionescu, X.L. Wang, S.X. Dou, E.W. Collings, M.D. Sumption, M. Bhatia, Z.W. Lin, and J.G. Zhu. Improvement of critical current density and thermally assisted individual vortex depinning in pulsed-laser-deposited YBa 2Cu 3O 7-δ thin films on SrTiO 3 (100) substrate with surface modification by Ag nanodots. *Journal of Applied Physics*, 97(10):1–5, 2005.

G. Li, H. Saito, S. Ishio, T. Shima, and K. Takanashi. Anomalous magnetization processes and non-symmetrical domain wall displacements in L10 FePt particulate films. *Journal of Magnetism and Magnetic Materials*, 303(1):14–19, 2006.

G. Li, H. Saito, S. Ishio, T. Shima, K. Takanashi, and Z. Xiong. Asymmetric initial magnetization process of elongated particles in nucleation-type L10 FePt films. *Journal of Magnetism and Magnetic Materials*, 315(2):126–131, 2007.

J.M. Liu. Simple technique for measurements of pulsed Gaussian-beam spot sizes. *Opt. Lett.*, (7):196–198, 1982.

R. Longtin, C. Fauteux, L.-P. Carignan, D. Therriault, and J. Pegna. Laser-assisted synthesis of carbon nanofibers: From arrays to thin films and coatings. *Surface and Coatings Technology*, 202(12):2661–2669, 2008.

A. Lorusso, M.L. de Giorgi, C. Fotakis, B. Maiolo, P. Miglietta, E.L. Papadopoulou, and A. Perrone. Y thin films by ultrashort pulsed laser deposition for photocathode application. *Applied Surface Science*, 258(22):8719–8723, 2012.

N.H. Luong, V.V. Hiep, D.M. Hong, N. Chau, N.D. Linh, M. Kurisu, D.T.K. Anh, and G. Nakamoto. High-coercivity FePt sputtered films. *Journal of Magnetism and Magnetic Materials*, 290-291 PART 1:559–561, 2005.

M.H. Magnusson, K. Deppert, J.-O. Malm, J.-O. Bovin, and L. Samuelson. Gold nanoparticles: Production, reshaping, and thermal charging. *Journal of Nanoparticle Research*, 1(2):243–251, 1999.

M.H. Magnusson, K. Deppert, and J.-O. Malm. Single-crystalline tungsten nanoparticles produced by thermal decomposition of tungsten hexacarbonyl. *Journal of Materials Research*, 15(7):1564–1569, 2000.

S. Mahmood, R.S. Rawat, S.V. Springham, T.L. Tan, and P. Lee. Material ablation and plasma plume expansion study from Fe and graphite targets in Ar gas atmosphere. *Applied Physics A: Materials Science and Processing*, 101(4):695–699, 2010.

T. Makino, N. Suzuki, Y. Yamada, T. Yoshida, T. Seto, and N. Aya. Size classification of Si nanoparticles formed by Pulsed Laser Ablation in helium background gas. *Applied Physics A: Materials Science and Processing*, 69(7):S243–S247, 1999.

A. Marcu, C. Grigoriu, W. Jiang, and K. Yatsui. Pulsed laser deposition of YBCO thin films in a shadow mask configuration. *Thin Solid Films*, 360(1-2):166–172, 2000.

M. Marjamäki, J. Keskinen, D.-R Chen, and D.Y.H. Pui. Performance evaluation of the electrical low-pressure impactor (ELPI). *Journal of Aerosol Science*, 31(2):249–261, 2000.

M. Markovich, J. Roqueta, J. Santiso, E. Lakin, E. Zolotoyabko, and A. Rothschild. Epitaxial growth of Nb-doped SrTiO3 films by pulsed laser deposition. *Applied Surface Science*, 258(23):9496–9500, 2012.

J. Martín-Sánchez, A. Chahboun, S.R.C. Pinto, A.G. Rolo, L. Marques, R. Serna, E.M.F. Vieira, M.M.D. Ramos, and M.J.M. Gomes. A shadowed off-axis production of Ge nanoparticles in Ar gas atmosphere by pulsed laser deposition. *Applied Physics A: Materials Science and Processing*, 110:585–590, 2012.

A. Martins, M.C.A. Fantini, and A.D. Santos. Growth of L10 ordered FePt alloy films at reduced temperatures. *Physica Status Solidi (A) Applied Research*, 201(5):837–841, 2004.

A. Martins, M.C.A Fantini, N.M Souza-Neto, A.Y Ramos, and A.D Santos. Alternate monatomic layer sputter deposition of FCT (L10-type) ordered FePt and CoPt films. *Journal of Magnetism and Magnetic Materials*, 305(1):152–156, 2006.

A.D Maynard. The development of a new thermophoretic precipitator for scanning transmission electron microscope analysis of ultrafine aerosol particles. *Aerosol Science and Technology*, 23(4):521–533, 1995.

A. Messerer, R. Niessner, and U. Pöschl. Thermophoretic deposition of soot aerosol particles under experimental conditions relevant for modern diesel engine exhaust gas systems. *Journal of Aerosol Science*, 34(8):1009–1021, 2003.

M.E. Messing, K.A. Dick, L.R. Wallenberg, and K. Deppert. Generation of size-selected gold nanoparticles by spark discharge - For growth of epitaxial nanowires. *Gold Bulletin*, 42(1):20–26, 2009.

M.E. Messing, C.R. Svensson, J. Pagels, B.O. Meuller, K. Deppert, and J. Rissler. Gas-borne particles with tunable and highly controlled characteristics for nanotoxicology studies. *Nanotoxicology*, 7(6):1052–1063, 2013.

H.B Michaelson. The work function of the elements and its periodicity. *Journal of Applied Physics*, 48(11):4729–4733, 1977.

D. Nakamura, T. Shimogaki, K. Okazaki, I.A Palani, K. Kubo, K. Tsuta, M. Higashihata, and T. Okada. Influence of ZnO buffer layer on ZnO nanowire growth by nanoparticle-assisted pulsed laser deposition. *Advanced Materials Letters*, 3(2):66–70, 2012.

K. Nakaso, M. Shimada, K. Okuyama, and K. Deppert. Evaluation of the change in the morphology of gold nanoparticles during sintering. *Journal of Aerosol Science*, 33(7): 1061–1074, 2002.

K.K. Nanda, F.E. Kruis, H. Fissan, and M. Acet. Band-gap tuning of PbS nanoparticles by in-flight sintering of size classified aerosols. *Journal of Applied Physics*, 91(4): 2315–2321, 2002.

T. Nunokawa, Y. Onodera, M. Hara, Y. Kitamoto, O. Odawara, and H. Wada. Preparation of Y2O3:Er,Yb nanoparticles by laser ablation in liquid. *Applied Surface Science*, 261: 118–122, 2012.

Hisahito Ogawa, Atsushi Abe, Masahiro Nishikawa, and Shigeru Hayakawa. Electrical properties of tin oxide ultrafine particle films. *Journal of the Electrochemical Society*, 128(9):2020–2025, 1981a.

Hisahito Ogawa, Atsushi Abe, Masahiro Nishikawa, and Shigeru Hayakawa. Preparation of tin oxide films from ultrafine particles. *Journal of the Electrochemical Society*, 128(3):685–689, 1981b.

K. Okuyama, Y. Kousaka, N. Tohge, S. Yamamoto, J.J. Wu, R.C. Flagan, and J.H. Seinfeld. Production of ultrafine metal oxide aerosol particles by thermal decomposition of metal alkoxide vapors. *AIChE Journal*, 32(12):2010–2019, 1986.

T. Orii, M. Hirasawa, and T. Seto. Tunable, narrow-band light emission from size-selected Si nanoparticles produced by pulsed-laser ablation. *Applied Physics Letters*, 83(16):3395–3397, 2003.

T. Orii, T. Seto, and M. Hirasawa. Target system for fabrication and control of magnetic metal content in diluted magnetic semiconductors by pulsed-laser deposition. *Journal of Vacuum Science and Technology A: Vacuum, Surfaces and Films*, 22(5):2096–2100, 2004.

T. Orii, M. Hirasawa, and T. Seto. Effect of in situ annealing on structure and optical properties of ZnTe nanoparticles produced by pulsed laser ablation. *Journal of Physics: Conference Series*, 59(1):716–719, 2007.

S. Orlando, A. Santagata, G.P. Parisi, L. Medici, S. Kaciulis, A. Mezzi, A. Bellucci, E. Cappelli, and D.M. Trucchi. Structural, chemical, and electrical characterization of indium nitride produced by pulsed laser ablation. *Physica Status Solidi (C) Current Topics in Solid State Physics*, 9(3-4):993–996, 2012.

M. Osaci, C. Abrudean, and A. Berdie. Relaxation times in magnetic nanoparticles system and memory effects. *Acta Physica Polonica A*, 112(6):1203–1212, 2007.

E. Ozawa, Y. Kawakami, and T. Seto. Formation and size control of tungsten nano particles produced by Nd:YAG laser irradiation. *Scripta Materialia*, 44(8-9):2279–2283, 2001.

D. Padilla-Rueda, J.M. Vadillo, and J.J. Laserna. Room temperature pulsed laser deposited ZnO thin films as photoluminiscence gas sensors. *Applied Surface Science*, 259:806–810, 2012.

I.A. Palani, D. Nakamura, K. Okazaki, M. Highasiata, and T. Okada. Structural and optical properties of Sb-Al co-doped ZnO nanowires synthesized using Nanoparticle Assisted Pulsed Laser Deposition (NAPLD) with Sb as catalyst. *Journal of Alloys and Compounds*, 527:112–116, 2012.

J.J. Park, J.K. Song, J.S. Ha, and S.M. Park. The effects of magnetic field on pulsed laser deposition of Mg-doped ZnO thin films. *Applied Surface Science*, 258(22):8542–8547, 2012.

C. Peineke and A. Schmidt-Ott. Explanation of charged nanoparticle production from hot surfaces. *Journal of Aerosol Science*, 39(3):244–252, 2008.

A. Pereira, L. Cultrera, A. Dima, M. Susu, A. Perrone, H.L. Du, A.O. Volkov, R. Cutting, and P.K. Datta. Pulsed laser deposition and characterization of textured Pd-doped-SnO 2 thin films for gas sensing applications. *Thin Solid Films*, 497(1-2):142–148, 2006.

C.L. Platt and K.W. Wierman. Use of film thickness and Cu additive to improve (0 0 1) texture in MgO/FePtCu(C) bilayers. *Journal of Magnetism and Magnetic Materials*, 295(3):241–245, 2005.

C.L. Platt, A.E. Berkowitz, D.J. Smith, and M.R. McCartney. Correlation of coercivity and microstructure of thin CoFe films. *Journal of Applied Physics*, 88(4):2058–2062, 2000.

C.L. Platt, K.W. Wierman, E.B. Svedberg, R. van de Veerdonk, J.K Howard, A.G. Roy, and D.E. Laughlin. L10 ordering and microstructure of FePt thin films with Cu, Ag, Au additive. *Journal of Applied Physics*, 92(10):6104–6109, 2002.

C.L. Platt, K.W. Wierman, J.K. Howard, A.G. Roy, and D.E. Laughlin. A comparison of FePt thin films with HfO2 or MnO additive. *Journal of Magnetism and Magnetic Materials*, 260(3), 2003.

S. Polarz, A. Roy, M. Merz, S. Halm, D. Schröder, L. Schneider, G. Bacher, F.E Kruis, and M. Driess. Chemical vapor synthesis of size-selected zinc oxide nanoparticles. *Small*, 1(5):540–552, 2005.

B. Rellinghaus, J. Kästner, T. Schneider, E.F. Wassermann, and P. Mohn. Thermodynamic analysis of Fe72Pt28 Invar. *Physical Review B*, 51(5):2983–2993, 1995.

B. Rellinghaus, S. Stappert, E.F. Wassermann, H. Sauer, and B. Spliethoff. The effect of oxidation on the structure of nickel nanoparticles. *European Physical Journal D*, 8 (3):249–252, 2000.

H.M. Rietveld. The Rietveld method: A Retrospection. *Z. Kristallogr.*, 225:545–547, 2010.

J. Rodríguez-Carvajal and T. Roisnel. Line Broadening Analysis Using Fullprof: Determination of Microstructural Properties. *Materials Science Forum*, 443-444:123–126, 2004.

D. R. Rolison. Nanoparticles: Synthesis, Properties and Applications. *Institute of Physics Publishing, London, UK*, page 305, 1996.

C.-B Rong, N. Poudyal, and J.P Liu. Effect of thermal fluctuations on magnetization reversal of L10 FePt nanoparticles. *Journal of Physics D: Applied Physics*, 43(49), 2010.

J. Rosell-Llompart, I.G. Loscertales, D. Bingham, and J. Fernández de la Mora. Sizing nanoparticles and ions with a short differential mobility analyzer. *Journal of Aerosol Science*, 27(5):695–719, 1996.

K. Sakiyama, K. Koga, T. Seto, M. Hirasawa, and T. Orii. Formation of size-selected Ni/NiO Core-Shell particles by Pulsed Laser Ablation. *Journal of Physical Chemistry B*, 108(2):523–529, 2004.

V. Salgueiriño-Maceira, M.A. Correa-Duarte, and M. Farle. Manipulation of chemically synthesized FePt nanoparticles in water: Core-shell silica/ FePt nanocomposites. *Small*, 1(11):1073–1076, 2005.

M. Sanz, M. López-Arias, E. Rebollar, R. de Nalda, and M. Castillejo. Laser ablation and deposition of wide bandgap semiconductors: Plasma and nanostructure of deposits diagnosis. *Journal of Nanoparticle Research*, 13(12):6621–6631, 2011.

Y. Sasaki, M. Mizuno, A.C.C. Yu, M. Inoue, K. Yazawa, I. Ohta, M. Takahashi, B. Jeyadevan, and K. Tohji. Crystallographic structures and magnetic properties of L10-type FePt nanoparticle monolayered films stabilized on functionalized surfaces. *Journal of Magnetism and Magnetic Materials*, 282(1-3):122–126, 2004.

R. Savu and E. Joanni. Low-temperature, self-nucleated growth of indium-tin oxide nanostructures by pulsed laser deposition on amorphous substrates. *Scripta Materialia*, 55(11):979–981, 2006.

H.G. Scheibel and J. Porstendörfer. Generation of monodisperse Ag- and NaCl-aerosols with particle diameters between 2 and 300 nm. *Journal of Aerosol Science*, 14(2): 113–126, 1983.

A. Schmidt-Ott, P. Schurtenberger, and H. Siegmann. Enormous yield of photoelectrons from small particles. *Physical Review Letters*, 45(15):1284–1287, 1980.

T. Schrefl, G. Hrkac, D. Suess, W. Scholz, and J. Fidler. Coercivity and remanence in self-assembled FePt nanoparticle arrays. *Journal of Applied Physics*, 93(10 2):7041–7043, 2003.

S. Schwyn, E. Garwin, and A. Schmidt-Ott. Aerosol generation by spark discharge. *Journal of Aerosol Science*, 19(5):639–642, 1988.

S.A. Sebt, S.S. Parhizgar, M. Farahmandjou, P. Aberomand, and M. Akhavan. The role of ligands in the synthesis of FePt nanoparticles. *Journal of Superconductivity and Novel Magnetism*, 22(8):849–854, 2009.

D.J. Sellmyer, Y. Xu, M. Yan, Y. Sui, J. Zhou, and R. Skomski. Assembly of high-anisotropy L10 FePt nanocomposite films. *Journal of Magnetism and Magnetic Materials*, 303(2 SPEC. ISS):302–308, 2006.

K.S Seol, K. Takeuchi, T. Miyagawa, and Y. Ohki. Characteristics of nanoparticles formed during pulsed laser ablation of SrBi2Ta2O9. *Japanese Journal of Applied Physics, Part 1: Regular Papers and Short Notes and Review Papers*, 41(9):5654–5658, 2002a.

K.S. Seol, S. Tomita, K. Takeuchi, T. Miyagawa, T. Katagiri, and Y. Ohki. Gas-phase production of monodisperse lead zirconate titanate nanoparticles. *Applied Physics Letters*, 81(10):1893–1895, 2002b.

T. Seto, T. Nakamoto, K. Okuyama, M. Adachi, Y. Kuga, and K. Takeuchi. Size distribution measurement of nanometer-sized aerosol particles using DMA under low-pressure conditions. *Journal of Aerosol Science*, 28(2):193–206, 1997.

T. Seto, Y. Kawakami, N. Suzuki, M. Hirasawa, and N. Aya. Laser Synthesis of Uniform Silicon Single Nanodots. *Nano Letters*, 1(6):315–318, 2001a.

T. Seto, Y. Kawakami, N. Suzuki, M. Hirasawa, S. Kano, N. Aya, S. Sasaki, and H. Shimura. Evaluation of morphology and size distribution of silicon and titanium oxide nanoparticles generated by laser ablation. *Journal of Nanoparticle Research*, 3 (2-3):185–191, 2001b.

T. Seto, T. Orii, M. Hirasawa, and N. Aya. Fabrication of silicon nanostructured films by deposition of size-selected nanoparticles generated by pulsed laser ablation. *Thin Solid Films*, 437(1-2):230–234, 2003.

T. Seto, H. Akinaga, F. Takano, K. Koga, T. Orii, and M. Hirasawa. Magnetic properties

of monodispersed Ni/NiO core-shell nanoparticles. *Journal of Physical Chemistry B*, 109(28):13403–13405, 2005.

T. Seto, K. Koga, H. Akinaga, F. Takano, T. Orii, and M. Hirasawa. Laser ablation synthesis of monodispersed magnetic alloy nanoparticles. *Journal of Nanoparticle Research*, 8(3-4):371–378, 2006.

S. Shamsaei, M. Ghoreishi, and Y. Javid. An investigation into laser ablation of copper films with a Nd:YAG laser. *Lasers in Engineering*, 23(3-4):151–162, 2012a.

S. Shamsaei, M. Ghoreishi, and Y. Javid. An investigation into laser ablation of copper films with a Nd:YAG laser. *Lasers in Engineering*, 23(3-4):151–162, 2012b.

J. Shi, S. Gider, K. Babcock, and D. Awschalom. Magnetic clusters in molecular beams, metals, and semiconductors. *Science*, 271(5251):937–941, 1996.

Q. Shi, C. Wang, D. Zhang, S. Li, L. Zhang, W. Wang, and J. Zhang. Luminescence of Cr 3+-doped ZnGa2O4 thin films deposited by pulsed laser ablation. *Thin Solid Films*, 520(23):6845–6849, 2012.

T. Shima, K. Takanashi, Y.K. Takahashi, and K. Hono. Coercivity exceeding 100 kOe in epltaxially grown FePt sputtered films. *Applied Physics Letters*, 85(13):2571–2573, 2004.

N. Shukla, J. Ahner, and D. Weller. Dip-coating of FePt nanoparticle films: Surfactant effects. *Journal of Magnetism and Magnetic Materials*, 272-276(SUPPL. 1):e1349–e1351, 2004.

C. Sima, C. Grigoriu, C. Besleaga, T. Mitran, L. Ion, and S. Antohe. Porous nanostructured ZnO films deposited by picosecond laser ablation. *Materials Science and Engineering B: Solid-State Materials for Advanced Technology*, 177(14):1182–1187, 2012.

S. Singamaneni, V.N. Bliznyuk, C. Binek, and E.Y. Tsymbal. Magnetic nanoparticles: Recent advances in synthesis, self-assembly and applications. *Journal of Materials Chemistry*, 21(42):16819–16845, 2011.

S.C. Singh and H. Zeng. Nanomaterials and nanopartterns based on laser processing: A brief review on current state of art. *Science of Advanced Materials*, 4(3-4):368–390, 2012.

R. Skomski, A. Kashyap, and J. Zhou. Atomic and micromagnetic aspects of L10 magnetism. *Scripta Materialia*, 53(4):389–394, 2005.

M.A. Sobhan, M. Ams, M.J. Withford, and E.M. Goldys. Ultrafast laser ablative generation of gold nanoparticles: The influence of pulse energy, repetition frequency and spot size. *Journal of Nanoparticle Research*, 12(8):2831–2842, 2010.

F.E. Spada, F.T. Parker, C.L. Platt, and J.K. Howard. X-ray diffraction and Mössbauer studies of structural changes and L 10 ordering kinetics during annealing of polycrystalline Fe51Pt49 thin films. *Journal of Applied Physics*, 94(8):5123–5134, 2003.

S. Stappert, B. Rellinghaus, M. Acet, and E.F Wassermann. Gas-phase preparation of L10 ordered FePt nanoparticles. *Journal of Crystal Growth*, 252(1-3):440–450, 2003.

S.C. Stern, H.W. Zeller, and A.I. Schekman. Collection efficiency of jet impactors at reduced pressures. *Industrial & Engineering Chemistry Fundamentals*, 1(4):273–277, 1962.

M. R. Stolzenburg. An Ultrafine Aerosol Size Distribution Measuring System. *PhD thesï¿œs,University of Minnesota*, 1988.

M.R. Stolzenburg and P.H. McMurry. Equations governing single and tandem DMA configurations and a new lognormal approximation to the transfer function. *Aerosol Science and Technology*, 42(6):421–432, 2008.

S. Sun, C.B. Murray, D. Weller, L. Folks, and A. Moser. Monodisperse FePt nanoparticles and ferromagnetic FePt nanocrystal superlattices. *Science*, 287(5460):1989–1992, 2000.

S. Sun, E.E. Fullerton, D. Weller, and C.B. Murray. Compositionally controlled FePt nanoparticle materials. *IEEE Transactions on Magnetics*, 37(4 I):1239–1243, 2001.

S. Sun, S. Anders, H.F. Hamann, J.-U. Thiele, J.E.E. Baglin, T. Thomson, E.E. Fullerton, C.B. Murray, and B.D. Terris. Polymer mediated self-assembly of magnetic nanoparticles. *Journal of the American Chemical Society*, 124(12):2884–2885, 2002.

S. Sun, S. Anders, T. Thomson, J.E.E. Baglin, M.F. Toney, H.F. Hamann, C.B. Murray, and B.D. Terris. Controlled synthesis and assembly of FePt nanoparticles. *Journal of Physical Chemistry B*, 107(23):5419–5425, 2003.

K. Suzuki, M. Inoguchi, K. Kageyama, H. Takagi, and Y. Sakabe. Well-crystallized zinc oxide quantum dots with narrow size distribution. *Journal of Nanoparticle Research*, 11(6):1349–1360, 2009.

K. Suzuki, N. Tanaka, A. Ando, and H. Takagi. Size-selected copper oxide nanoparticles synthesized by laser ablation. *Journal of Nanoparticle Research*, 14(5):1–11, 2012.

N. Suzuki, T. Makino, Y. Yamada, T. Yoshida, and T. Seto. Monodispersed, nonagglomerated silicon nanocrystallites. *Applied Physics Letters*, 78(14):2043–2045, 2001.

L. Talbot, R.K Cheng, R.W Schefer, and D.R Willis. Thermophoresis of particles in a heated boundary layer. *Journal of Fluid Mechanics*, 101(4):737–758, 1980.

H. Tanaka and F. Maeda. Number-adjustable nanoparticle clusters realized by a combination of Ag and C60 nanoparticles in the gas phase. *Chemical Physics Letters*, 484 (1-3):37–40, 2009.

R. Teghil, L. D'Alessio, A. de Bonis, D. Ferro, A. Galasso, G. Lanza, A. Santagata, P. Villani, and D.J. Sordelet. Ultra-short pulse laser ablation of Al70Cu20Fe10 alloy: Nanoparticles generation and thin films deposition. *Thin Solid Films*, 517(6): 1880–1886, 2009.

T. Teranishi, M. Nakaya, and M. Kanehara. Application of FePt nanoparticle superlattices to nanomagnetic devices. *Polymer Preprints, Japan*, 54(2):4793–4794, 2005.

K. Theis-Bröhl, D. Mishra, B.P. Toperverg, H. Zabel, B. Vogel, A. Regtmeier, and A. Hütten. Self organization of magnetic nanoparticles: A polarized grazing incidence small

angle neutron scattering and grazing incidence small angle x-ray scattering study. *Journal of Applied Physics*, 110(10):1–6, 2011.

J.-U. Thiele, L. Folks, M.F. Toney, and D.K. Weller. Perpendicular magnetic anisotropy and magnetic domain structure in sputtered epitaxial FePt (001) L1 0 films. *Journal of Applied Physics*, 84(10):5686–5692, 1998.

L. Torrisi and R. Setola. Thermally assisted hydroxyapatite obtained by pulsed-laser deposition on titanium substrates. *Thin Solid Films*, 227(1):32–36, 1993.

S.C. Tsang, C.H. Yu, H. Tang, Y. He, V. Castelletto, I.W. Hamley, T. Narayanan, C.C.H. Lo, and K. Tam. Assembly of centimeter long silica coated FePt colloid crystals with tailored interstices by magnetic crystallization. *Chemistry of Materials*, 20(14):4554–4556, 2008.

M.B.F. van Raap, P.M. Zélis, D.F. Coral, T.E. Torres, C. Marquina, G.F. Goya, and F.H. Sánchez. Self organization in oleic acid-Coated CoFe 2O 4 colloids: A SAXS study. *Journal of Nanoparticle Research*, 14(9):1–10, 2012.

M.R. Visokay and R. Sinclair. Direct formation of ordered CoPt and FePt compound thin films by sputtering. *Applied Physics Letters*, (66):1692–1694, 1995.

J. Wan, M.J Bonder, Y. Huang, G.C Hadjipanayis, and C. Ni. (0 0 1) Exchange-coupled FCC/L10 FePt bilayers. *Journal of Magnetism and Magnetic Materials*, 322(13):1811–1815, 2010.

H.L. Wang, Y. Huang, Y. Zhang, G.C. Hadjipanayis, D. Weller, and A. Simopoulos. Effects of annealing on the magnetic and structural properties of FePt nanoparticles prepared by chemical synthesis. *Journal of Magnetism and Magnetic Materials*, 310(1):22–27, 2007.

J.-P. Wang. FePt magnetic nanoparticles and their assembly for future magnetic media. *Proceedings of the IEEE*, 96(11):1847–1863, 2008.

S. Wang, S.S. Kang, D.E. Nikles, J.W. Harrell, and X.W. Wu. Magnetic properties of self-organized L10 FePtAg nanoparticle arrays. *Journal of Magnetism and Magnetic Materials*, 266(1-2):49–56, 2003.

Z. Wang, X. Li, M. Gao, and X. Zeng. One-step preparation of amorphous iron nanoparticles by laser ablation. *Powder Technology*, 215-216:147–150, 2012.

K. Wasa and S. Hayakawa. *Handbook of Sputter Deposition Technology: Principles, Technology and Applicatons*. Materials Science and Process Technology Series. Noyes Publ, 1992. ISBN 9780815512806.

D. Weller, A. Moser, L. Folks, M.E Best, W. Lee, M.F Toney, and M. Schwickert. High ku materials approach to 100 gbits/qin. *IEEE Transactions on Magnetics*, 36(1 PART 1): 10–15, 2000.

S.H. Whang, Q. Feng, and Y.-Q. Gao. Ordering, deformation and microstructure in L10 type FePt. *Acta Materialia*, 46(18):6485–6495, 1998.

R.L. Whetten, D.M. Cox, D.J. Trevor, and A. Kaldor. Advances in research on clusters of transition metal atoms. *Surface Science*, 156(PART 1):8–35, 1985.

A. Wiedensohler. An approximation of the bipolar charge distribution for particles in the submicron size range. *Journal of Aerosol Science*, 19(3):387–389, 1988.

K.W. Wierman, C.L. Platt, and J.K. Howard. Thickness dependent stress relaxation with the onset of L1 0 ordering in FePt thin films. *Materials Research Society Symposium - Proceedings*, 795:217–222, 2003a.

K.W. Wierman, C.L. Platt, J.K. Howard, and F.E. Spada. Evolution of stress with L10 ordering in FePt and FeCuPt thin films. *Journal of Applied Physics*, 93(1-2):7160–7162, 2003b.

K.W. Wierman, C.L. Platt, and J.K. Howard. Impact of stoichiometry on L10 ordering in FePt and FePtCu thin films. *Journal of Magnetism and Magnetic Materials*, 278(1-2): 214–217, 2004.

W. Winklmayr, G.P. Reischl, A.O. Lindner, and A. Berner. A new electromobility spectrometer for the measurement of aerosol size distributions in the size range from 1 to 1000 nm. *Journal of Aerosol Science*, 22(3):289–296, 1991.

B. Wolf. *Handbook of Ion Sources*. CRC PressINC, 1995. ISBN 9780849325021.

J. Woltersdorf, A.S. Nepijko, and E. Pippel. Dependence of lattice parameters of small particles on the size of the nuclei. *Surface Science*, 106(1-3):64–69, 1981.

Y. Xing and D.E. Rosner. Surface melting of particles: Predicting spherule size in vapor-phase nanometer particle formation. *Materials Research Society Symposium - Proceedings*, 457:167–172, 1997.

S.C. Xu, C. Yang, M. Liu, S.Z. Jiang, Y.Y. Ma, C.S. Chen, X.G. Gao, Z.C. Sun, B. Hu, C.C. Wang, and B.Y. Man. High quality FeSi2 thin films prepared on silicon (100) by using pulsed laser ablation of Fe target. *Materials Chemistry and Physics*, 135(2-3): 991–997, 2012.

H. Zeng, S. Sun, T.S. Vedantam, J.P. Liu, Z.-R. Dai, and Z.-L. Wang. Exchange-coupled FePt nanoparticle assembly. *Applied Physics Letters*, 80(14):2583–2585, 2002.

M. Zhang and A.S. Wexler. Cross flow ion mobility spectrometry: Theory and initial prototype testing. *International Journal of Mass Spectrometry*, 258(1-3):13–20, 2006.

S.-H. Zhang, Y. Akutsu, L.M. Russell, R.C. Flagan, and J.H. Seinfeld. Radial differential mobility analyzer. *Aerosol Science and Technology*, 23(3):357–372, 1995.

Y. Zhang, J. Wan, M.J. Bonder, G.C. Hadjipanayis, and D. Weller. Formation of FePt nanoparticles in annealed FePt/C multilayers. *Journal of Applied Physics*, 93(10 2): 7175–7177, 2003a.

Y. Zhang, J. Wan, S. Stoyan, V. Skumryev, G.C. Hadjipanayis, and D. Weller. Thickness effect on the formation of FePt nanoparticles in FePt/C multilayers. *Microscopy and Microanalysis*, 9(SUPPL. 2):514–515, 2003b.

Y. Zhang, J. Wan, and G.C Hadjipanayis. Microstructure characterization of FePt/Ti/Si thin films. *Microscopy and Microanalysis*, 14(SUPPL. 2):352–353, 2008.

N. Zotov, J. Feydt, and A. Ludwig. Dependence of grain sizes and microstrains on annealing temperature in Fe/Pt multilayers and L10 FePt thin films. *Thin Solid Films*, 517(2):531–537, 2008.

Appendix A.

The laser ablation chamber

Between CF double cross and laser entering gauge class an intersection CF tube (length 150 mm) was placed in order to overcome nanoparticle deposit on the fused silica glass. Especially larger fragments of ablated material possess a large kinetic energy and together with larger inertia they are able to leave the guiding carrier gas stream originated at the nozzle. Those fragments are impacting on the inner housing of the ablation chamber. When hitting the fused silica glas the fragments are irradiated by laser beam which causes a sintering of such on the glas. Prior ablation process without intersection caused an increase of photonic energy absorption by such layer formation. Thus evident only a fraction of energy reached the rod and decrease of particle production rate was the final result. The area of the nozzle exit generates the highest pressure drop and gas velocity(Fig.A.0.1). Therefore, it was placed as close as possible towards the laser impaction area in order to maximize guiding drag force and minimize particle losses.
The CCD camera was used for adjusting the movement and position of the rod while laser ablation was in progress. Two synchronous motors were used for the axial und longitudinal movement of the FePt rod and revolutions could be controlled by varying the motor voltages. Longitudinal shift was achieved by means of an excenter toothwheel with crankshaft and rotation by a toothwheel fixed on the moving rod. Reducing gearboxes were flanged to the motors in order to allow slow motion and smooth removal of material. While having a laser spot diameter of 1 mm for the rotation of the rod a

frequency of 0.5 Hz and the translation a speed of 0.5 mm/s was set.

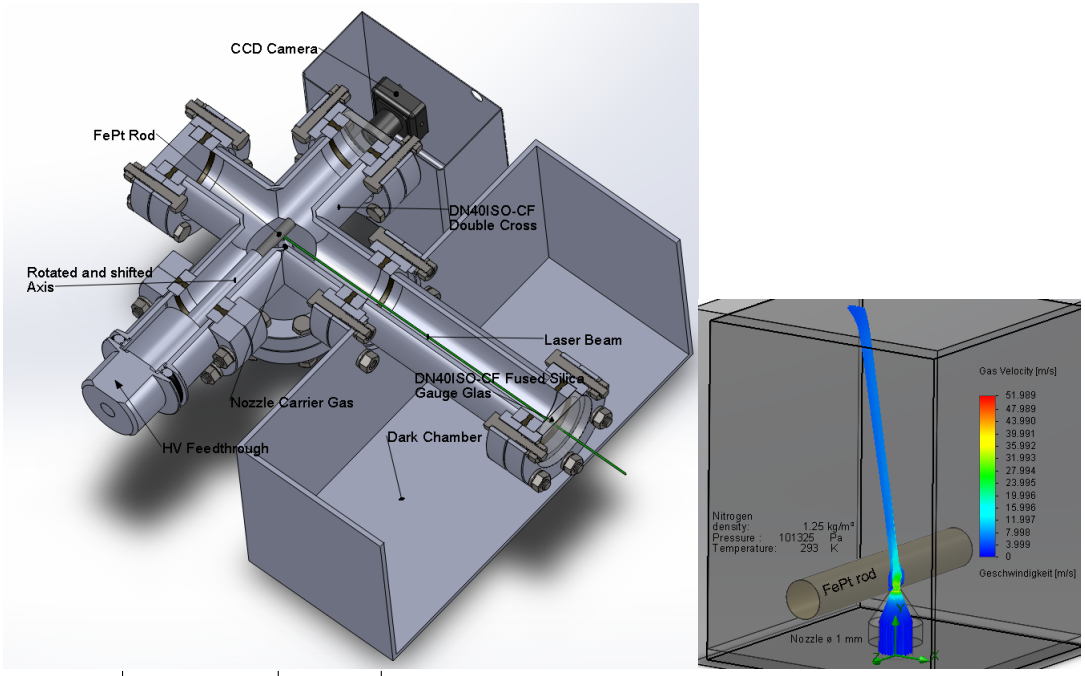

Q_{in}[l/min]	max. v_{gas}[m/s]	Mach [-]
2	52	0.15
10	225	0.65
15	294	0.85

Figure A.0.1.: The Laser Ablation Chamber: Cut through and model for fluid simulation with Fluent 3D(laminar flow condition only).Table shows the maximum gas velocity and Mach number as function of the introduced volume flow of the carrier gas nitrogen. Mach 1 is reached at around 20 l/min(maximum flow rate due to choked nozzle).

Appendix B.

Curriculum vitae

Due to obligation of secrecy the curriculum vitae is not available in the online version.